

---

# Electron Pulse Control with Terahertz Fields

Dominik Patrick Ehberger

---



München 2019



---

# **Electron Pulse Control with Terahertz Fields**

**Dominik Patrick Ehberger**

---

Dissertation  
an der Fakultät für Physik  
der Ludwig-Maximilians-Universität  
München

vorgelegt von  
Dominik Patrick Ehberger  
aus Altötting

München, den 14.05.2019

Erstgutachter: Prof. Dr. Ferenc Krausz

Zweitgutachter: Prof. Dr. Alexander Högele

Tag der mündlichen Prüfung: 28.06.2019

# Zusammenfassung

Nahezu alle makroskopisch beobachtbaren physikalischen, chemischen und biologischen Prozesse haben ihren Ursprung auf atomarer Ebene. Die initiale Dynamik dieser Prozesse spielt sich typischerweise auf Längenskalen im Bereich von Pikometern ( $10^{-12}$  m) und auf Zeitskalen von bis zu wenigen Femtosekunden ( $10^{-15}$  s) und noch schneller ab. Ultrakurze Pulse freier Elektronen mit de-Broglie-Wellenlängen von nur wenigen Pikometern ermöglichen mittels Mikroskopie, Beugung und Spektroskopie die atomare Struktur einer zu untersuchenden Probe zu bestimmen. In Kombination mit optischen Anregungsmethoden bieten sie damit die Möglichkeit feinste strukturelle Änderungen zeitaufgelöst zu untersuchen. Bei dieser Methode der *zeitaufgelösten Elektronenbildgebung* sind für gewöhnlich die Dauer des Elektronen-Abfragepulses und dessen Synchronisation mit dem optischen Anregepuls die limitierenden Faktoren der Zeitauflösung. Coulomb-Wechselwirkungen der geladenen Teilchen im Puls und die durch deren Masse bedingte Dispersion im Vakuum begrenzen die Elektronenpulsdauer zu typischerweise mehreren hundert Femtosekunden. Die Verwendung von nur wenigen Elektronen pro Puls sowie auf Mikrowellentechnik basierenden Kompressionskonzepten erlaubt prinzipiell die Erzeugung von fast beliebig kurzen Elektronenpulsen. Jedoch stellt die Synchronisation zwischen den optischen Pulsen und der Mikrowellenphase eine große technische Hürde dar, welche das Ziel auf diesem Wege eine Zeitauflösung im Sub-Femtosekunden-Bereich zu erreichen in weite Ferne rücken lässt.

Die vorliegende Dissertation befasst sich daher mit einem neuartigen Ansatz der Erzeugung, Manipulation und Charakterisierung ultrakurzer Elektronenpulse mittels rein optischer Methoden. Basis aller hierin gezeigten Experimente ist die Kontrolle optisch generierter Wellenformen im Terahertzbereich und deren Wechselwirkung mit Femtosekundenelektronenpulsen. Ein Hauptaspekt ist dabei die maßgeschneiderte Interaktion von Elektronenpulsen mit einem elektromagnetischen Subzyklus, welche es ermöglicht, Teilchen innerhalb eines Pulses zeit- und ortsabhängig zu beschleunigen, abzubremesen und abzulenken. Diese, dem hier demonstrierten Konzept eigene, multidimensionale Kontrolle erlaubt es, Elektronenpulse nicht nur deutlich zu

verkürzen, sondern sie zudem entlang ihrer Propagationsachse nahezu beliebig zu verkippen, was eine Vielzahl an neuen Möglichkeiten für Anrege-Abfrage-Experimente mit Elektronen birgt. Es wird gezeigt, dass mit diesem Ansatz eine mehr als 17-fache Reduktion der Elektronenpulsdauer auf 12 Femtosekunden (rms) erreicht werden kann und dies bei einer Langzeitstabilität, welche jene von konventionellen mikrowellenbasierten Konzepten bei Weitem übertrifft.

Die Entwicklung von terahertzbasierten Charakterisierungstechniken mit kleinsten Zeitauflösung ist ein ebenso zentrales Anliegen dieser Arbeit. Der dabei entstandene experimentelle Aufbau erlaubt mittels femtosekundengenauer Elektronenlaufzeitmessungen, die Bestimmung sowohl der zeitlichen, als auch der räumlichen Form eines zuvor optisch präparierten Elektronenpulses. So lässt sich nicht nur die reine Dauer eines solchen Pulses messen, sondern auch dessen Korrelationen in Position und Zeit. Mit dieser erweiterten Diagnostik konnte im Rahmen der vorliegenden Arbeit eine Relation zwischen Verkippungswinkel und Winkeldispersion von massebehafteten Teilchen entdeckt werden, die auf neue physikalische Zusammenhänge hinweist, welche jenseits reinen Anwendungsbezugs liegen. Darüber hinaus erlaubt die Messung der genauen zeitlichen Struktur eines komprimierten Elektronenpulses die Rekonstruktion seines Energiespektrums. Dieses strikt auf optischen Methoden beruhende Spektrometer-Konzept wurde im Rahmen dieser Arbeit anhand der Messung von Elektronenenergie-Verlustspektren mit einer Auflösung von wenigen Elektronenvolt zum ersten Mal demonstriert.

Die hier entwickelten optischen Manipulationstechniken bringen Einzelelektronenpulse von Dauern unterhalb der Femtosekundenschwelle in greifbare Nähe. Darauf weisen Simulationen und analytische Betrachtungen in dieser Arbeit hin. Damit eröffnet sich ein neues Regime zeitaufgelöster elektronenbasierter Bildgebungsverfahren um die Dynamik atomarer und elektronischer Prozesse in komplexen Materialien erstmals auf ihren fundamentalen Längen- und Zeitskalen zu beobachten. Schon mit den hier demonstrierten Elektronenpulsen lässt sich eine Vielzahl von bislang unbeobachteter struktureller Dynamiken, wie etwa die schnellster Phononenmoden, untersuchen. Die in dieser Arbeit entwickelten Techniken zur multidimensionalen Elektronenpulskontrolle bergen das Potential konventionelle Konzepte der Teilchenmanipulation auf ein neues Level rein optischer Kontrolle zu bringen und damit zur Entstehung einer neuen Generation von Teilchenbeschleunigern, Freie-Elektronen-Lasern und Elektronenmikroskopen beizutragen.

# Abstract

Almost all macroscopically observable physical, chemical and biological processes originate from the atomic level. The initial dynamics of these processes typically unfolds on length scales in the range of picometers ( $10^{-12}$  m) and time scales in the range of down to a few femtoseconds ( $10^{-15}$  s) and even faster. Ultrashort pulses of free electrons with de-Broglie wavelengths of only few picometers can be used to resolve the atomic structure of a sample via microscopy, diffraction and spectroscopy. In combination with methods of optical excitation they offer the possibility of investigating the finest structural changes in a time-resolved manner. This method of *time-resolved electron imaging* is typically limited in temporal resolution by the duration of the electron probe pulse and its synchronization with the optical pump pulse. Coulomb interactions of the charged particles in the pulse and their mass-induced dispersion in vacuum limit the electron pulse duration to typically several hundred femtoseconds. Using only a few electrons per pulse as well as microwave-based compression schemes in principle allow for the generation of almost arbitrarily short electron pulses. However, the synchronization between the optical pulses and the microwave phase imposes a major technical obstacle, which makes the aim to achieve temporal resolution in the subfemtosecond range by these means appear rather remote.

The present dissertation therefore deals with a novel approach of generation, manipulation and characterization of ultrashort electron pulses by purely optical means. The control of optically generated waveforms and their interplay with femtosecond electron pulses is the basis of all experiments shown herein. A key theme is the tailored interaction of electron pulses with an electromagnetic subcycle, which enables the acceleration, deceleration, and deflection of particles within a pulse as a function of space and time. This multidimensional control, which is inherent to the concept demonstrated here, not only allows substantial compression of electron pulses, but also the ability to tilt them almost arbitrarily with respect to their propagation axis, which creates a broad range of new possibilities for pump-probe experiments with electrons. It is shown that with this approach a more than 17-times reduction of the

electron pulse duration to 12 femtoseconds (rms) is achievable, featuring a long-term stability which greatly exceeds those of conventional microwave-based approaches.

The development of terahertz-based characterization techniques of smallest temporal resolution is an equally central subject of this work. The experimental setup developed to this end allows the determination of both the temporal and spatial shape of a previously optically prepared electron pulse using electron arrival-time measurements with femtosecond accuracy. In this way not only the duration of such a pulse is measurable, but also its correlation in position and time. With this extended diagnostic, a relation between tilt angle and angular dispersion of massive particles was discovered in the course of this thesis, which indicates new physical relationships beyond mere applications. Furthermore, the measurement of the exact temporal structure of a compressed electron pulse allows the reconstruction of its energy spectrum. This all-optical spectrometer concept has been demonstrated for the first time in the course of this thesis by measuring electron energy loss spectra with few-electronvolt resolution.

The optical manipulation techniques developed here make single-electron pulses of subfemtosecond duration feasible. This is indicated by simulations and analytic considerations in this work. These techniques open a new regime of time-resolved electron imaging and will allow the observation of atomic and electronic dynamics for the first time on their fundamental length and time scales. With the electron pulse durations demonstrated here, a variety of previously unobserved structural dynamics, such as those of fastest phonon modes, can already be investigated. The techniques of multidimensional electron pulse control developed in this work bear the potential to bring conventional concepts of particle manipulation to a new level of all-optical control and may contribute to the emergence of a new generation of particle accelerators, free electron lasers and electron microscopes.

# List of peer-reviewed publications by the author

- D. Ehberger**, K. J. Mohler, T. Vasileiadis, R. Ernstorfer, L. Waldecker, and P. Baum, [Terahertz Compression of Electron Pulses at a Planar Mirror Membrane](#), *Physical Review Applied* **11**, 024034 (2019).
- D. Ehberger**, A. Ryabov, and P. Baum, [Tilted Electron Pulses](#), *Physical Review Letters* **121**, 094801 (2018).
- D. Ehberger**, C. Kealhofer, and P. Baum, [Electron energy analysis by phase-space shaping with THz field cycles](#), *Structural Dynamics* **5**, 044303 (2018).
- B.-H. Chen, M. Kretschmar, **D. Ehberger**, A. Blumenstein, P. Simon, P. Baum, and T. Nagy, [Compression of picosecond pulses from a thin-disk laser to 30 fs at 4 W average power](#), *Optics Express* **39**, 6604 (2018).
- C. Kealhofer, W. Schneider, **D. Ehberger**, A. Ryabov, F. Krausz, and P. Baum, [All-optical control and metrology of electron pulses](#), *Science* **352**, 429 (2016).
- M. V. Tsarev, **D. Ehberger**, and P. Baum, [High-average-power, intense THz pulses from a LiNbO<sub>3</sub> slab with silicon output coupler](#), *Applied Physics B* **122**, 30 (2016).
- J. McNeur, M. Kozak, **D. Ehberger**, N. Schönenberger, A. Tafel, A. Li, and P. Hommelhoff, [A miniaturized electron source based on dielectric laser accelerator operation at higher spatial harmonics and a nanotip photoemitter](#), *Journal of Physics B: Atomic, Molecular and Optical Physics* **49**, 034006 (2016).
- D. Ehberger**, J. Hammer, M. Eisele, M. Krüger, J. Noe, A. Högele, and P. Hommelhoff, [Highly Coherent Electron Beam from a Laser-Triggered Tungsten Needle Tip](#), *Physical Review Letters* **114**, 227601 (2015).

J. Hoffrogge, J. P. Stein, M. Krüger, M. Förster, J. Hammer, **D. Ehberger**, P. Baum, and P. Hommelhoff, [Tip-based source of femtosecond electron pulses at 30 keV](#), Journal of Applied Physics **115**, 094506 (2014).

# Contents

<b>Zusammenfassung</b>	<b>v</b>
<b>Abstract</b>	<b>vii</b>
<b>List of peer-reviewed publications</b>	<b>ix</b>
<b>1 The route towards atomic resolution in space and time</b>	<b>1</b>
1.1 Ultrafast imaging methods: historical overview . . . . .	2
1.2 Shaping electron pulses by all-optical means . . . . .	4
1.3 Terahertz control of electron pulses: scope of this thesis . . . . .	7
<b>2 Phase space picture of electron pulse compression</b>	<b>13</b>
2.1 Femtosecond single-electron pulses for ultrafast imaging . . . . .	13
2.2 Longitudinal phase space representation of an electron pulse . . . . .	15
2.3 Electron pulse propagation and the Rayleigh time . . . . .	18
2.4 Phase space preparation with temporal lenses . . . . .	21
2.5 Imaging with temporal lenses . . . . .	23
2.5.1 The temporal lens equation . . . . .	24
2.5.2 Pulse compression with a single temporal lens . . . . .	27
2.5.3 Susceptibility to timing jitter and energy fluctuations . . . . .	29
2.6 Application I: the multistage compressor . . . . .	31
2.7 Application II: the dynamic monochromator . . . . .	36
<b>3 High-average-power, intense THz pulses from a LiNbO<sub>3</sub> slab with silicon output coupler</b>	<b>41</b>
3.1 Preface . . . . .	41
3.2 Tsarev et al., Appl. Phys. B 122, 30 (2016) . . . . .	47

<b>4</b>	<b>All-optical control and metrology of electron pulses</b>	<b>57</b>
4.1	Preface . . . . .	57
4.2	Kealhofer et al., Science 352, 429 (2016) . . . . .	61
4.2.1	Concept and implementation . . . . .	62
4.2.2	Electron pulse compression . . . . .	63
4.2.3	Temporal characterization . . . . .	64
4.2.4	Compression and measurement . . . . .	67
4.2.5	Electron-laser timing metrology . . . . .	67
4.2.6	Direct THz-electron interaction at a foil: a THz cathode-ray-tube oscilloscope . . . . .	70
4.2.7	Conclusions and outlook . . . . .	71
<b>5</b>	<b>Electron energy analysis by phase-space shaping with THz field cycles</b>	<b>73</b>
5.1	Preface . . . . .	73
5.2	Ehberger et al., Struct. Dyn. 5, 044303 (2018) . . . . .	75
5.2.1	Introduction . . . . .	75
5.2.2	Concept for THz-based time-of-flight detection . . . . .	77
5.2.3	Experimental setup . . . . .	79
5.2.4	Results . . . . .	80
5.2.5	Discussion . . . . .	81
5.2.6	Multi-stage THz-ToF for energy resolution beyond the cathode limit . . . . .	82
5.2.7	Conclusions and outlook . . . . .	85
<b>6</b>	<b>Tilted electron pulses</b>	<b>87</b>
6.1	Preface . . . . .	87
6.2	Ehberger et al., Phys. Rev. Lett. 121, 094801 (2018) . . . . .	93
<b>7</b>	<b>Terahertz compression of electron pulses at a planar mirror membrane</b>	<b>103</b>
7.1	Preface . . . . .	103
7.2	Ehberger et al., Phys. Rev. Applied 11, 024034 (2019) . . . . .	107
7.2.1	Introduction . . . . .	107
7.2.2	Concept and experimental setup . . . . .	108
7.2.3	Results on pulse compression . . . . .	111
7.2.4	Timing stability . . . . .	113
7.2.5	Discussion . . . . .	115
<b>8</b>	<b>Conclusions and outlook</b>	<b>119</b>

**Table of Contents** **xiii**

---

<b>Appendix A</b>	<b>123</b>
<b>Appendix B</b>	<b>125</b>
<b>Appendix C</b>	<b>133</b>
<b>Data Archiving</b>	<b>139</b>
<b>Bibliography</b>	<b>141</b>
<b>Acknowledgments</b>	<b>163</b>



# Chapter 1

## The route towards atomic resolution in space and time

Ever since ancient times, humans have wondered about the structure of matter. Within only the past two centuries, initial philosophical concepts about our world's smallest constituents and their composition were revolutionized more than once by scientific discoveries. Today we know that matter consist of atoms. We know the atomic sub-structure down to the level of quarks and leptons. We have a profound understanding of how quarks form protons, neutrons and eventually the atomic nucleus. And we know how the electronic structure of an atom defines its binding properties to form solid, liquid or gaseous compounds. But the further we move away from the atomic level towards more complex molecules and crystals, the more sparse our knowledge becomes. Even the simple triatomic water molecule ( $\text{H}_2\text{O}$ ) is still debated with regard to its structural properties and dynamics [1, 2]—let alone for example the highly complex phenomena in proteins of living organisms. Understanding the complexity of matter from a fundamental point of view is therefore one of the main tasks of modern science across multiple disciplines such as physics, chemistry and biology.

It is fair to ask why humankind has not yet solved such an outstanding problem, despite the knowledge of the fundamental quantum mechanical principles and given the broad relevance of this field of research. The problem arises from the huge variety of microscopic configurations a macro-system can have and the probabilistic description that quantum mechanics requires. For this reason, the computational effort to fully describe real systems scales exponentially with the number of particles involved [3]. That is why, even with modern supercomputers, it is nearly impossible to simulate interesting, i.e. complex, materials in order to predict their properties *ab initio*. This challenge is encountered by science with computational modelling ap-

proaches such as density functional theory [4], quantum simulators such as ultracold gases in optical lattices [5] and the development of quantum computers and their powerful algorithms to outperform classical machines [6].

A conceptually different experimental approach to unscramble complex materials is to investigate the structural dynamics of real specimen. Studying how the change of macroscopic material properties (e.g. conductivity, magnetization or photosensitivity) is linked to changes in the microscopic structure, i.e. the electronic and nuclear configuration, allows to gain deep insight into basic and specific functionalities of matter. In this way, researchers strive to find general concepts or principles (and exceptions thereof) to bring order into the zoo of macroscopic phenomena. For instance, the insulator-to-metal transition of vanadium dioxide ( $\text{VO}_2$ ) that goes along with a profound change in its atomic and electronic structure, has been studied for decades [7–10] and still bears subtleties to be discovered [11]. Other prominent examples of dynamic phenomena of atomic-scale origin include ultrafast demagnetization [12–14] and optically induced superconductivity [15, 16]. The knowledge about the individual and common dynamics of such transitions, induced by external perturbations of photonic, chemical or stochastic nature, is key to designing future materials and devices or improving existing ones. Study of such processes with atomic resolution in both space and time is therefore at the heart of contemporary materials science—as is the development of experimental techniques to do so.

## 1.1 Ultrafast imaging methods: historical overview

X-ray diffraction, pioneered by Max von Laue at the Ludwig-Maximilians-Universität München in 1912 [17] and further developed by William L. Bragg and his father William H. Bragg [18, 19], was the first technique capable of resolving the lattice structure of condensed matter. Since then, it has been widely used for structural analysis of many samples, as for example to find the double-helix structure of DNA in 1953 [20]. X-rays, in contrast to visible light, can resolve the atomic structure of crystals because their wavelength is shorter than the inter-nuclear distances. Massive particles such as electrons and neutrons of typically even shorter wavelengths are also used for crystallographic purposes. In fact, the de-Broglie hypothesis of matter possessing wave-characteristics, was first confirmed by diffraction of electrons at a nickel crystal by Davisson and Germer in 1927 and independently by Thomson in the same year [21, 22]. Diffraction, compared to microscopy, has the advantage of directly accessing a sample’s crystalline structure, which is much harder to observe

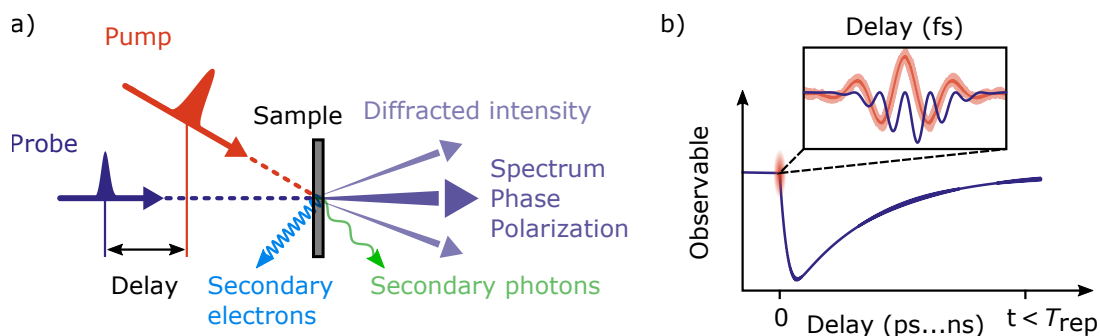


**Figure 1.1:** The pump-probe scheme. a) Experimental concept. A pump pulse (red) impinging on a sample triggers a dynamic process. The delayed probe pulse (blue) is used to retrieve information about the transient state of the sample via various direct and indirect observables. b) Exemplary time trace of an observable in a pump-probe experiment (see for instance Ref. [13]). The dynamics is completed within the pulse repetition period  $T_{\text{rep}}$  before the next pump pulse arrives. Inset: given sufficiently short probe pulses, sub-cycle processes following the field of the pump pulse (red) can be recovered (trace inspired by [28]).

by direct imaging.<sup>1</sup> Also, real images can be reconstructed from diffraction data by algorithms [25, 26], which are complementary to microscopic approaches.

Time-resolved measurements for tracking dynamical processes rely on experimental techniques to capture information from a specimen in a transient state, such that the dynamics appears “frozen” in time at each glance. Our eyes can track changes not faster than roughly 10–100 milliseconds, depending on the kind of perceived information [27]. Everything occurring on shorter timescales remains hidden from bare sight. Special techniques are therefore required to observe structural and atomic dynamics which may happen on timescales of femtoseconds ( $10^{-15}$  s) and below.

Access to these realms was made possible by advances in laser technology producing ever shorter and more powerful bursts of light. Ultrafast pump-probe techniques rely on such short pulses. The basic concept of this method is depicted in Fig. 1.1 a. A pump pulse (red) initiates a process in a sample under investigation and a second pulse (blue), which is delayed in time, probes and captures its transient state. This procedure is then repeated with varying delay between the pump and the probe pulse. Various experimental signatures related to the probe pulse can be used to recover the dynamics of the process (see Fig. 1.1 b). These signatures may be related to (diffracted) intensity, spectral information or polarization of the probe pulse, but can be also more complex in form of photoelectron spectra, molecular dissociation products or secondary radiation. The shortness and precise timing of the pump and probe pulses is of utter importance for the temporal resolution of the technique. The

<sup>1</sup>The first microscopic image of individual atoms was provided by the technique of field ion microscopy in the 1950s [23, 24]—decades after the first diffraction experiments.

sharper the initiation of the investigated process by the pump pulse is defined in time and the shorter the interaction of the probing pulse with the specimen, the finer dynamical details, down to suboptical-cycle phenomena, can be resolved (see inset of Fig. 1.1 b).

In 1982 it was shown by Mourou and Williamson that laser-triggered photoelectrons can be used as ultrafast probe pulses, which simultaneously access the lattice structure of the sample via diffraction [29]. Even though the temporal resolution in the earliest experiments was limited to tens of picoseconds [30] and therefore not fast enough to resolve fundamental atomic motions, this seminal work can be regarded as the birth of a technique that would later be known as Ultrafast Electron Diffraction (UED). The development and application of UED has since experienced a huge boost, fueled by work in the groups of Ahmed Zewail [31], R.J. Dwayne Miller [32, 33] and many others. In the early 2000s the technique’s time resolution broke the picosecond mark [34], enabling a wealth of new phenomena to be investigated [35–42]. However, the bottleneck to the overall temporal resolution of the technique has been and still is the electron probe pulse duration. Coulomb repulsion of the charged particles in the pulse and their dispersion in vacuum (see Chapter 2) limit the electron pulse duration to typically hundreds of femtoseconds. Although attosecond electron pulse trains have been demonstrated [43–45] and used as probes for diffraction and microscopy in 2018 [44], due to their fast sequence, they cannot be used to recover dynamics on timescales longer than an optical cycle ( $\sim 1$  fs). There remains a “blind spot” in the temporal resolution of UED in the range of roughly 1 to 100 femtoseconds, which has not been studied with isolated electron probe pulses this far.<sup>2</sup> Closing this resolution gap to be able to cover some of the most fundamental laser-induced phenomena such as the *push and pull* of electronic charges in the laser field [48, 28], the coupling to the fastest lattice vibrations [49, 50] and their eventual relaxation is one of the main motivations of this thesis.

## 1.2 Shaping electron pulses by all-optical means

At the time when electron pulses for imaging and diffraction entered the femtosecond regime [34], techniques to produce optical pulses already had progressed to attosecond realms. Advances in laser development in the late 1990s had resulted in methods to produce laser pulses consisting of only a few oscillations of the electromagnetic field [51]. The growing control over the shape of these fields [52, 53] enabled the

---

<sup>2</sup>While time-resolved x-ray diffraction techniques already offer time resolution below 100 fs, they require huge accelerator facilities [46, 47]. This is in contrast to ultrafast electron diffraction experiments with subrelativistic electrons, which usually are tabletop setups that can be operated by a single scientist.

emergence of attosecond metrology [54]—a technique which since has formed and refined our understanding of dynamics on atomic time scales (see [55] and references therein), albeit without the equivalent spatial resolution.

Inspired by the success of attosecond physics and driven by the desire to combine its temporal resolution with the sub-atomic spatial resolution offered by electron diffraction, various schemes to produce attosecond electron pulses emerged around that time [56–59]. Techniques borrowing from conventional particle beam physics using microwave cavities [60–62] allow the compression of electron pulses down to durations of tens of femtoseconds [63–65]. These concepts are based on a field-induced and time-dependent manipulation of an electron pulse’s velocity distribution. The aim is to decelerate particles in the leading part of the pulse and accelerate those in the trailing part. A pulse prepared in this way will self-compress upon further propagation (see Chapter 2). From a conceptual point of view it is possible to generate sub-femtosecond pulses by those means [57]. In practice, however, laser-to-microwave synchronization issues [66, 67] and environmental constraints [66] prevent this approach from fully unfolding its capabilities.

A way to circumvent synchronization issues in optical-pump electron-probe experiments, is to manipulate electron pulses directly with light from the same laser source as used for electron pulse generation and sample excitation. However, this is by no means a trivial task. A linearly polarized, electromagnetic plane wave interacting with an electron cannot transfer net momentum to the particle in free space [68]. In a classical picture, the electron wiggles in the electromagnetic field, but because it gets accelerated or deflected as much in one way as in the other during the interaction, the effect averages to zero. In a quantum picture, this is equivalent to saying that the dispersion relations (i.e. the relation between a particle’s energy and its momentum) of the free electron and the photon do not match and thus an interaction between the two cannot simultaneously fulfill energy and momentum conservation. Consequently, controlling free electrons by all-optical means requires special interaction geometries and schemes.

One of the first ideas to manipulate electrons by purely optical means dates back to the year 1933 in which Kapitza and Dirac proposed that electrons can be scattered off a standing optical wave just like from a crystal [69]. The Kapitza-Dirac effect is based on stimulated Compton scattering, which allows an electron to emit a photon absorbed from one beam into another optical beam. In this way, energy and momentum conservation of the process is guaranteed resulting in a recoil of the electron. Due to the low coupling strength of free electrons to visible light, the phenomenon stayed elusive until the development of very powerful laser sources and could only be demonstrated conclusively nearly 70 years after its proposal [70]. Meanwhile, this ponderomotive scheme has also been demonstrated for electron energy

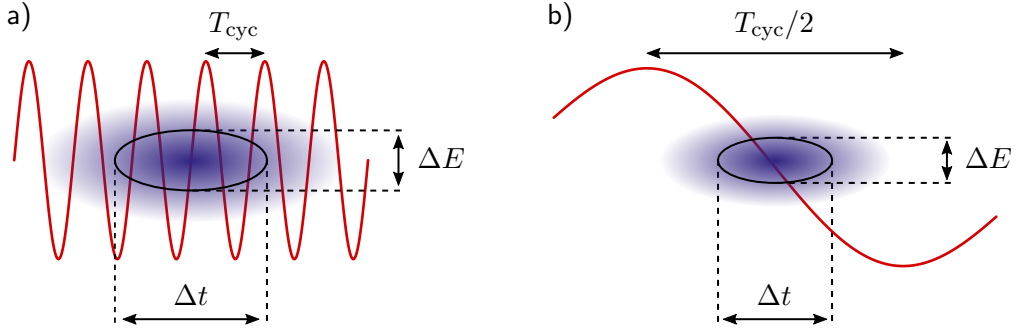


**Figure 1.2:** Two regimes of all-optical electron pulse manipulation. a) Photonic regime. The optical cycle duration is much shorter than the electron pulse duration. b) Sub-cycle regime. The electron pulse duration is much shorter than one optical cycle. Photonic effects vanish (see text).

modulation [71] and was used to generate attosecond electron pulse trains [59, 45]. Longitudinal energy transfer to electrons in free space can also be achieved by using the on-axis electromagnetic fields of focused, radially polarized laser pulses [72].

All-optical electron pulse manipulation schemes, which involve a third body facilitate the necessary conservation of momentum and energy. Evanescent optical fields with wavefronts modulated by virtue of nanofabricated dielectric structures allow to accelerate electron beams with high gradients and promise to outperform microwave-based accelerators [73–75]. They can also be used to deflect electron pulses and thereby provide a gating mechanism to generate femtosecond electron pulse trains [76]. Optical near-fields, confined to sub-wavelength dimensions do not obey the dispersion relation of the free (far-field) photon, allowing for energy modulation of the electron beam in multiples of the photon energy. This is the basic principle behind the technique of photon-induced near field microscopy (PINEM, [77]). It is also applied in optical electron microscopy beam manipulation schemes [78, 79] or electron pulse gating methods [80]. Similar momentum modulation effects can be realized by the conceptually simpler approach of introducing a laser-irradiated, symmetry breaking element in form of a dielectric or metallic membrane, which the electrons can transit. In this way the interaction gets truncated before it averages to zero. This element allows for electron acceleration [81], energy modulation [82, 83], and attosecond electron pulse train generation and detection [43, 44] directly with laser pulses. It is also one of the key elements used in this work.

All of the above schemes operate in a regime where the electron pulse duration  $\Delta t$  is much longer than the duration of an optical cycle  $T_{cyc} = 1/\nu$  (see Fig. 1.2 a). If we seek to manipulate an entire electron pulse monotonically in time, as it is required for its compression (see Chapter 2), we need to decrease the optical frequency  $\nu$ , such that the electron pulse duration is substantially shorter than an optical half-cycle

(Fig. 1.2 b):

$$\Delta t \ll \frac{T_{\text{cyc}}}{2} = \frac{h}{2E_{\text{ph}}}, \quad (1.1)$$

with the photon energy  $E_{\text{ph}} = h\nu$  and Planck's constant  $h$ . Likewise, Heisenberg's uncertainty principle puts a lower limit to the bandwidth product of energy ( $\Delta E$ ) and time (minimum pulse duration):

$$\Delta E \Delta t \geq \frac{h}{4\pi}. \quad (1.2)$$

Combining the two relations yields

$$E_{\text{ph}} \ll (2\pi)\Delta E. \quad (1.3)$$

We see that the photon energy is less than the energy bandwidth of the electron pulse, if the optical cycle gets substantially longer than the electron pulse duration. Therefore, spectral features on the order of the modulating photon energy vanish if the interaction becomes sub-cycle. In turn, the presence of photonic sidebands in the electron spectrum (see for example Refs. [77, 84, 82, 78, 43, 83]) indicate a cycle-averaged interaction, which at best can produce pulse trains but never *isolated* electron pulses.<sup>3</sup> In order to compress isolated electron pulses we therefore need to work in a non-photonic regime where electrons are controlled by less than a single cycle of the electromagnetic field (see Fig. 1.2 b).

To this end, electromagnetic waves oscillating roughly a thousand times slower than visible light are required. Optically generated terahertz waveforms (see for example Ref. [88]) fulfill this requirement. Their comparably long cycle duration ( $\sim$  ps) and wavelength ( $\sim$  mm) nicely match common electron pulse dimensions used for UED, while synchronization to the driving laser source is inherent. Taking the electron pulse manipulation capabilities of microwave technology and combining them with optical momentum transfer concepts to obtain sub-cycle control *and* inherent synchronicity in the terahertz frequency domain, is what this work is focused on.

### 1.3 Terahertz control of electron pulses: scope of this thesis

The present thesis reports the development and application of all-optical electron pulse control schemes at terahertz frequencies to overcome the current limitations of UED and to enable novel experimental concepts with ultrafast electron pulses. The

---

<sup>3</sup>This is similar to the notion of interference from slits in time [85, 86, 84] and analogous to optical attosecond pulses and their spectrum [87].

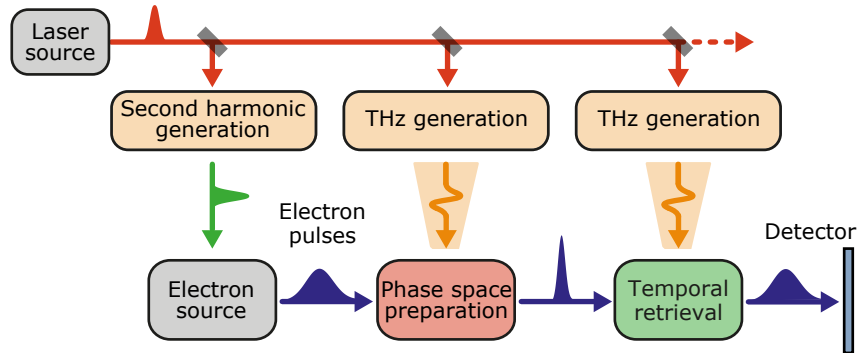


**Figure 1.3:** Conceptual layout of the terahertz-based electron pulse manipulation experiments of this thesis. A single femtosecond laser source, whose output (red) is split into three arms, drives the respective frequency conversion stages required for electron pulse generation, manipulation and characterization. Adapted from [89].

range of this thesis spans from the theoretical investigation of phase-space dynamics of terahertz-manipulated electron pulses, over the development of a simple-to-realize frequency conversion scheme to generate single-cycle terahertz transients, to the design and implementation of a variety of all-optical electron pulse compression and characterization concepts. Those concepts include the realization of a phase-space shaping scheme to measure electron energy loss spectra by purely optical means; a terahertz-based, multidimensional electron pulse control technique to form and measure tilted and compressed electron pulses by virtue of which a fundamental connection between pulse tilt angle and angular dispersion of matter waves was discovered and which finally led to the shortest isolated electron pulses generated by all-optical means. All of these terahertz-driven concepts have been realized for the first time in the course of this thesis.

The basic layout of the experiments conducted here is shown in Fig. 1.3. Electron pulses from a flat photocathode are triggered by the second harmonic of pulses from a driving laser source and subsequently accelerated to kinetic energies of tens of keV in a static electric field such that they move with roughly half of the speed of light. Those electron pulses with durations of few hundreds of femtoseconds then interact with a single-cycle terahertz pulse generated from the same laser source. Appropriately designed interaction elements, such as bow-tie shaped resonators or thin metallic membranes allow the efficient momentum transfer from the electromagnetic wave to the charged particles in the pulse. In particular, the deceleration of electrons in the leading part of the pulse and acceleration of those in the trailing part leads to compression of the entire electron pulse along its propagation axis such that it becomes shorter in time. Compression factors of nearly 20, resulting in pulses as short as 12 fs (root-mean-squared) were achieved by these means. This pulse duration

is not only on par with the record for the shortest sub-relativistic electron pulses so far [64], but also the high temporal robustness of this scheme renders these pulses directly suitable for probing of fastest lattice dynamics in condensed matter systems.

In addition to time-dependent acceleration, the terahertz-based phase-space preparation stage (Fig. 1.3, red box) can also be used to deflect electron pulses in time. It has been found in this thesis, that the complex interplay of acceleration/deceleration and deflection, both as function of space and time, allows the deliberate generation of compressed and tilted electron pulses whose tilt angle with the propagation axis is defined only by the orientation of the interaction element. Tilted electron pulses can be used to eliminate temporal mismatch between excitation and probe pulses in constrained experimental geometries and will therefore facilitate and improve future UED experiments. Furthermore, it has been found, that the tilt angle of these pulses obeys a relation to angular dispersion that was previously only known for non-massive particles.

At the temporal retrieval stage (Fig. 1.3, green box), electrons in a pulse are deflected as a function of their arrival time, which allows the measurement of their pulse duration with femtosecond-resolution via the concept of terahertz streaking developed here. In combination with appropriate imaging settings, also the spatio-temporal shape of the electron pulse is retrieved. The precise determination of particle arrival times allows electron energy spectra to be measured in a time-of-flight fashion, featuring demonstrated few-eV resolution over a base energy of 70 keV. This determination of energy spectra of femtosecond electron pulses enables the time-resolved investigation of inelastic scattering processes without conventional, bulky and expensive electron spectrometers.

The results gained in the course of this dissertation, already influenced other research on all-optical beam manipulation schemes. Prior to this work, terahertz pulses had only been used to accelerate electron pulses in a waveguide [90], while other manipulation and characterization schemes were still in a proposal stage [56, 91–94]. Since then, new terahertz-based concepts for manipulation of femtosecond electron pulses of up to relativistic energies have been demonstrated by other research groups [95–98]. The methods developed here have already enabled new electron microscopy concepts [99], inspired attosecond pulse train detection schemes via streaking [44, 100] and might one day drive next generation x-ray sources [101].

Given this broad range of capabilities, it is conceivable that terahertz-based electron pulse control schemes emerge as a substantial building block of charged particle beamlines. The present work may be seen as a contribution to this dawning paradigm shift in experimental particle physics as well as a major leap towards ultimately overcoming the temporal limitations of electron imaging techniques to resolve the most fundamental atomic dynamics in space and time.

## Outline of this thesis

This cumulative thesis is based on five original publications [102, 89, 103–105], which are reproduced in Chapters 3–7.<sup>4</sup> Each of these chapters begins with a preface, which gives additional background information and puts the respective original article in the context of this thesis. These introductory sections are also meant to (i) summarize the results to provide the reader a comprehensive overview without prior knowledge of the respective publication and (ii) emphasize the author’s contribution. The overall structure is as follows.

**Chapter 2** provides a theoretical treatment of electron pulse control in the longitudinal phase space. The therein derived and previously unpublished results provide a comprehensive theoretical framework of the later experimental work. It can be regarded as an extended introduction to pulse compression with temporal lenses.

**Chapter 3** deals with terahertz waveform generation from optical pump pulses in the near-infrared region to be used for electron pulse control. Using a slab-like LiNbO<sub>3</sub> structure with a silicon prism as output coupler allows the efficient generation of single-cycle terahertz transients by properly choosing the ideal pump focusing conditions. The value of this simple-to-realize scheme is demonstrated by its application in the various electron pulse manipulation schemes of this work in Chapters 4–7. The main part of this chapter is based on the publication [102].

**Chapter 4** details the first-time realization of an all-optical electron pulse compression and characterization experiment to avoid synchronization issues. Based on terahertz driven, bow-tie shaped resonators, compression factors of  $\sim 12$  are measured. The compressed electron pulses exhibit a passive temporal long term stability of a few femtoseconds, demonstrating the reliability of this setup for UED, which also has been proven by a subsequent independent pump-probe experiment [99]. The terahertz-based streaking concept for temporal electron pulse characterization with few-femtosecond resolution, laid out in this chapter, is used in all of the following experiments. The main part of this chapter has been previously published in [89].

**Chapter 5** demonstrates a novel concept to measure energy spectra of femtosecond electron pulses at tens of keV in an all-optical fashion. Energetic signatures of electron pulses that have probed a sample carry valuable structural information that can be used as a signal in a pump-probe experiment (see Fig. 1.1). The measurement concept relies on the ability to precisely determine particle arrival times in a compressed electron pulse via terahertz streaking. It is demonstrated by recording an electron energy loss spectrum of a thin aluminum foil with few-eV resolution at a base kinetic energy of 70 keV. Simulations show how this concept can be extended to

---

<sup>4</sup>Labels of equations, figures and references of the original articles have been modified to follow style and numbering of this thesis.

obtain meV-resolution. The results, reprinted in this chapter, have been previously published in [103].

**Chapter 6** treats the experimental generation of tilted electron pulses and contains a scientific discovery that has been made in the course of this thesis, which goes beyond technical achievements and demonstration of concepts. Using an ultrathin foil that electrons can transmit and terahertz pulses are reflected of, it has been found that electron pulses can not only be compressed but also tilted with respect to their propagation axis. The electron pulse tilt angle is solely determined by the angular configuration of electron and terahertz wave incident angles. This finding is supported by an excellent agreement between theory and experimental data. While this practical finding has great potential to improve time-resolution of UED experiments with constrained excitation geometries, it has also been discovered that electron pulses seem to obey the same relation between tilt angle and angular dispersion which previously was only known for optical pulses. The indication that the angular dispersion concept also holds for matter waves, might fuel future research on this topic and provide a more general understanding of electron pulse manipulation concepts. This research has been reported in [104], which the the main part of this chapter is a reprint of.

**Chapter 7** completes the terahertz-based electron pulse control experiments of this thesis. Applying the previous experimental as well as theoretical insights on electron pulse compression dynamics, a reduction of the electron pulse duration from 490 fs down to 28 fs (both FWHM) has been achieved. This has been done using a velocity-matched, terahertz-pulse-irradiated ultrathin mirror for electron pulse compression instead of bow-tie resonators. It could be shown, that the long-term as well as short-term temporal stability over 12 hours is on a few-femtosecond level. The measured pulse durations are well reproduced by simulations, which also show a way to generate isolated attosecond pulses. Meanwhile, the pulse compression scheme developed here can be used and is already in use for investigation of fastest structural dynamics and collective carrier motions. These results on electron pulse compression have been published in [105] and are reprinted in the main part of this chapter.

**Chapter 8** concludes the thesis by summarizing the insights gained in its course. It points towards promising future applications in ultrafast electron imaging and beyond.



# Phase space picture of electron pulse compression

In this chapter we investigate the dynamics of electron pulse compression in detail, making use of a statistical phase space approach. Thereby we derive fundamental relations between experimentally accessible parameters and the compressed electron pulse duration. The governing equations are in close analogy to the optical imaging equations for Gaussian beams and therefore allow us to treat temporal lenses with well established optical concepts. The chapter is concluded by using this approach to analyze the performance of two different applications of temporal lenses.

## 2.1 Femtosecond single-electron pulses for ultrafast imaging

Free electron pulses for tabletop ultrafast electron diffraction and microscopy are commonly generated by illumination of a cathode with a laser pulse of photon energies larger than the cathode material's work function. Flat photocathodes in a back or front illuminated geometry are a common choice for that purpose, but laser-triggered cold field emission needle-tips or Schottky emitters are also used as electron sources due to their superior beam quality [106–108]. Because photoelectron emission is a nearly instantaneous process [109], the emitted electron pulse resembles the temporal shape of the triggering laser pulse. For electron pulses to be suitable for diffraction and microscopy with the highest spatial resolution, they need to be accelerated to kinetic energies  $E_{\text{kin}}$  in the range of 30 . . . 300 keV.

Using the relativistic relation for the total energy  $E_{\text{tot}}$  of a particle

$$E_{\text{tot}} = \gamma m_e c^2 = m_e c^2 + E_{\text{kin}}, \quad (2.1)$$

with the electron rest mass  $m_e$ , the Lorentz factor  $\gamma = (1 - \beta^2)^{-\frac{1}{2}}$ , where  $\beta$  is the ratio of electron velocity  $v$  and the speed of light in vacuum  $c$ , yields

$$\gamma = 1 + \frac{E_{\text{kin}}}{m_e c^2} \approx 1 + \frac{|U_{\text{acc}}|}{511 \text{ kV}} \quad (2.2)$$

and

$$\beta = \sqrt{1 - \frac{1}{\gamma^2}}. \quad (2.3)$$

Here,  $U_{\text{acc}}$  is the static acceleration voltage of the electron source. For the electron energies considered,  $\gamma$  is in the range of 1.06 ... 1.59, which corresponds to electron pulse velocities in the lab frame of (0.33 ... 0.77)  $c$ . Hence, in contrast to relativistic electron pulses of kinetic energies larger than a few MeV, where  $\beta\gamma \approx \gamma$ , in our case  $\beta\gamma \sim \beta$ .

Real electron pulses have a finite energy bandwidth  $\Delta E$ . For planar femtosecond photocathodes in the absence of space charge, this energy spread is on the order of 1 eV or below [110]. It commonly results from a mismatch between the cathode material's work function and the photon energy of the triggering laser pulse [110]. Even when matching the photonic excitation by tuning the optical wavelength [110, 111], a finite energy spread remains as a result of the laser excitation bandwidth. Inhomogeneous emission sites, inelastic electron scattering and the density of states in the cathode material further contribute to the energy spectrum of the electron pulse. Consequently, this energy spread corresponds to a spread of forward velocity in the electron pulse  $\Delta v$ . Because the energy spread is small compared to the mean kinetic energy  $E_0$  of the electron pulse, we can linearize Eq. 2.1 which yields

$$\Delta v \approx \frac{\Delta E}{\beta_0 \gamma_0^3 m_e c}, \quad (2.4)$$

where  $\gamma_0 = \gamma(E_0)$  and  $\beta_0 = \beta(\gamma_0)$ . As an example, a 1-eV energy spread of an electron beam at 100 keV corresponds to a velocity spread of 626 m/s. This velocity is much lower than the speed of light and allows us to treat intrapulse dynamics nonrelativistically.

Unlike photons, higher energy electrons travel faster in vacuum than electrons of lower energy. Therefore an energy spread leads to an inevitable temporal broadening of an optically generated electron pulse upon acceleration [110] and subsequent propagation. However, this initially detrimental dispersive effect also opens up the possibility of compressing the electron pulse down to a duration much shorter than the initial. The mechanism of this effect, its conditions and consequences are subject of the remainder of this chapter.

For simplicity, we restrict the description of the electron pulses and their dynamics to the longitudinal phase space, assuming no coupling between forward acceleration/deceleration and deflection. The modulation of the longitudinal phase space is

treated as spatially homogeneous. We will see in Chapters 6 and 7 that for electron pulse compression, this assumption is very well justified under certain realistic, experimental conditions, known as velocity-matched interaction (see also [82, 104, 105]).

Furthermore, we neglect electron-electron interactions within the pulse, treating electrons as uncharged particles. This assumption is approximately valid for pulses of low charge or single-electron pulses [112]. The latter contain one electron per pulse on average. Because the electron emission process at the photocathode is of statistical nature, femtosecond electron pulses obey Poissonian statistics. The probability of having more than one electron in a pulse of a series containing one electron on average is therefore  $< 30\%$ . This probability decreases rapidly with decreasing average current. Therefore, repetitively generated single-electron pulses can, when averaged, be considered as one pulse of non-interacting particles, such as depicted in Fig. 2.1.<sup>1</sup>

Lastly, the assumption of point-like particles, which neglects quantum mechanical effects, is usually justified for electron pulses emitted from planar photocathodes. Due to the finite electron source size, which is determined by the laser spot size on the cathode and typically on the order of few to tens of microns [114, 115], as well as due to the finite energy spread, transverse and longitudinal coherence lengths are usually substantially smaller than the corresponding electron pulse dimensions [116]. This assumption allows us to neglect matter-wave phenomena in electron pulse compression [117] (see also Chapter 1).

## 2.2 Longitudinal phase space representation of an electron pulse

In the following, an electron pulse is described as an ensemble of  $N$  particles moving along the  $z$ -axis. Each electron is defined by its position  $z_n$  and forward velocity  $v_n$  corresponding to a defined coordinate in longitudinal phase space. Its configuration is described by the matrix

$$\mathbf{P} = \begin{pmatrix} z_1 & \dots & z_n & \dots & z_N \\ v_1 & \dots & v_n & \dots & v_N \end{pmatrix} = \begin{pmatrix} \mathbf{z} \\ \mathbf{v} \end{pmatrix}. \tag{2.5}$$

Figure 2.1 depicts an arbitrary phase space configuration  $\mathbf{P}$  of an electron pulse. The underlying distribution  $\varrho(z, v)$  is taken to be a bivariate normal distribution, which implies that its projection on position and velocity axis are of Gaussian shape

---

<sup>1</sup>Even though the single-electron approach requires comparably large accumulated measuring times, its practicability has been demonstrated in experiment [112] and substantiated by signal-to-noise considerations [113].

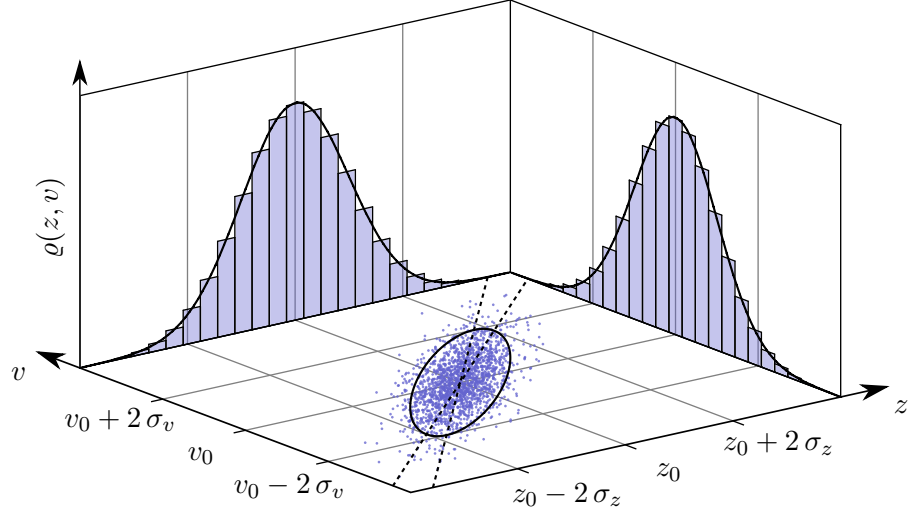


**Figure 2.1:** Phase space configuration  $P$  of an electron pulse. A particle is defined by its velocity and position (blue dots). Projections along  $z$  axis and  $v$  axis show particle histograms and the underlying distribution. The area defined by the emittance is shown as black ellipse. Dashed lines show the regression slopes.

with standard deviations denoted  $\sigma_z$  and  $\sigma_v$ , respectively.<sup>2</sup> The center or spatial mean value of the electron pulse is denoted  $z_0$ , it moves with a velocity of  $v_0 = \beta_0 c$ , which is the mean velocity. The full width at half maximum (FWHM) pulse duration of the electron pulse is linked to the statistical quantities by

$$\Delta t = \frac{2\sqrt{2\ln(2)}}{v_0} \sigma_z \quad (2.6)$$

and the FWHM energy spread according to Eq. 2.4 by

$$\Delta E \approx \gamma_0^3 v_0 m_e 2\sqrt{2\ln(2)} \sigma_v. \quad (2.7)$$

A useful statistical measure on phase space is the covariance matrix

$$\Sigma(\varrho) = \begin{pmatrix} \sigma_z^2 & \sigma_{zv} \\ \sigma_{zv} & \sigma_v^2 \end{pmatrix}. \quad (2.8)$$

Its diagonal elements are the squared standard deviations along the phase space dimensions of the electron pulse. The symmetric off-diagonal terms  $\sigma_{zv}$  represent the covariance of  $z$  and  $v$ , which is a measure for the velocity-position correlation  $\rho$  of the electron pulse, given by

$$\rho = \frac{\sigma_{zv}}{\sigma_z \sigma_v}. \quad (2.9)$$

<sup>2</sup>This definition allows us to easily switch between different definitions of pulse duration, such as full width at half maximum (FWHM) or root-mean-squared (rms).

Thus, for a phase space, which is uncorrelated in position and velocity ( $\rho = 0$ ), as shown in the left panel in Fig. 2.2,  $\Sigma$  is diagonal. The covariance matrix for a given phase space distribution  $\mathbf{P}$  can be estimated by  $\Sigma \approx (1/N)\mathbf{P}_0\mathbf{P}_0^T$ , where  $\mathbf{P}_0$  results from  $\mathbf{P}$  by row-wise subtraction of the respective mean values  $z_0$  and  $v_0$  [118].

In this chapter we will find expressions for the transformation of phase space configuration from an initial to a final state of the form  $\mathbf{P}' = \mathbf{M}\mathbf{P}_0$ .  $\mathbf{M}$  is a  $2 \times 2$  matrix with a determinant of unity, similar to optical ray transfer matrices [119]. Given  $\mathbf{M}$  and the initial covariance matrix  $\Sigma_0$ , the final covariance matrix  $\Sigma'$  of the transformed phase space is given by<sup>3</sup>

$$\Sigma' = \mathbf{M}\Sigma_0\mathbf{M}^T. \quad (2.10)$$

This transformation rule for the covariance matrix is a well known concept in particle physics (see for example [120, 121]). Also for our case, this rule largely simplifies the calculations that will be shown the next sections. It is central to our considerations, because all relevant statistical quantities, such as pulse duration, energy spread and phase space correlation can be derived from the covariance matrix via Eqs. 2.6, 2.7 and 2.9, respectively.

The covariance matrix is closely related to the emittance  $\varepsilon$ , which is another important quantity in particle physics. Beam emittance in each phase space plane is commonly defined as the area containing a certain fraction of all particles in a beam. In Fig. 2.1 this area is marked by the black ellipse. The lower the emittance of a given beam, the denser the particles are packed in phase space. Emittance is proportional to the square-root of the determinant of the covariance matrix [120]. The (normalized) longitudinal emittance is in analogy to Ref. [122] given by:

$$\varepsilon_{n,z} = \frac{4\pi\gamma_0}{c} \sqrt{\det(\Sigma)} = \frac{4\pi\gamma_0}{c} \sqrt{\sigma_z^2\sigma_v^2 - \sigma_{zv}^2}. \quad (2.11)$$

The prefactor of  $4\pi$  is conventional and refers to a 95 % criterion. Stated simply, the square of the longitudinal emittance is proportional to the product of pulse length and energy spread minus their mutual correlation. For simplicity, we will refer to the longitudinal emittance as  $\varepsilon_z = \sqrt{\det(\Sigma)}$  for the remainder of this chapter. Notably, emittance is conserved for phase space transformations  $\mathbf{M}$ , because

$$\begin{aligned} \varepsilon_z^2(\mathbf{P}') &= \det(\Sigma') = \det(\mathbf{M}\Sigma_0\mathbf{M}^T) = \det(\mathbf{M}) \det(\Sigma_0) \det(\mathbf{M}^T) \\ &= \det(\Sigma_0) = \varepsilon_z^2(\mathbf{P}_0), \end{aligned} \quad (2.12)$$

and  $\det(\mathbf{M}) = 1$ .

---

<sup>3</sup>This can be shown using the relation  $\mathbf{P}'\mathbf{P}'^T = (\mathbf{M}\mathbf{P}_0)(\mathbf{M}\mathbf{P}_0)^T = \mathbf{M}\mathbf{P}_0\mathbf{P}_0^T\mathbf{M}^T$ .

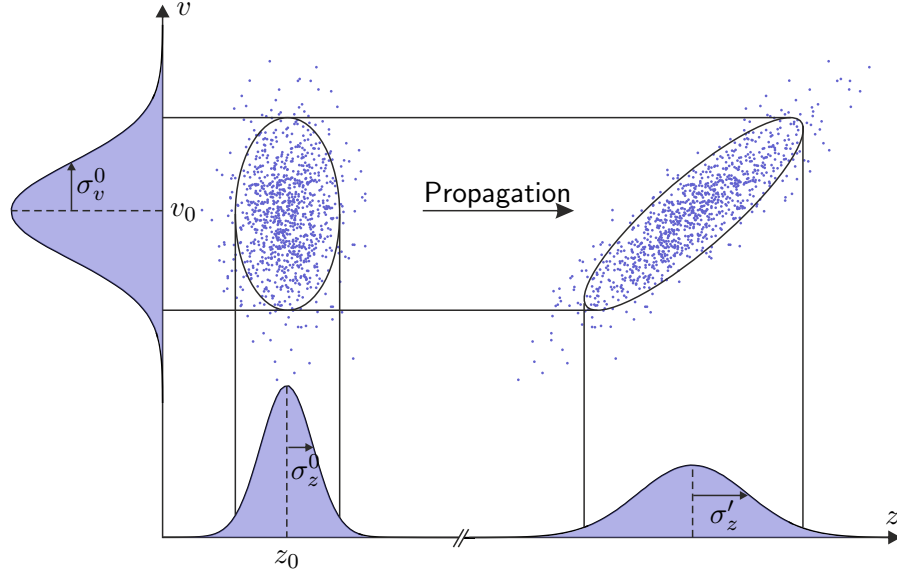


**Figure 2.2:** Phase space representation of electron pulse propagation. Projections show the respective space and velocity distributions. The electron pulse lengthens as correlations between position and velocity emerge. The velocity spread of the initial and the final pulse are equal.

### 2.3 Electron pulse propagation and the Rayleigh time

An electron at a position  $z_n$ , which is traveling for a time  $t$  in field-free space, reaches a new position  $z'_n$  according to  $z'_n = t \cdot v_n + z_n$ . For the entire pulse this corresponds to a transformation

$$\mathbf{P}' = \begin{pmatrix} z' \\ v' \end{pmatrix} = \begin{pmatrix} z + t \cdot v \\ v \end{pmatrix} = \mathbf{T} \mathbf{P}_0, \quad (2.13)$$

with the propagation matrix

$$\mathbf{T} = \begin{pmatrix} 1 & t \\ 0 & 1 \end{pmatrix}. \quad (2.14)$$

As depicted in Fig. 2.2, let us assume the initial phase space  $\mathbf{P}_0$  at  $t = 0$  is uncorrelated and the corresponding covariance matrix  $\Sigma_0$  therefore is diagonal. How does propagation affect the pulse properties? Using Eq. 2.10, we obtain

$$\Sigma' = \mathbf{T} \Sigma_0 \mathbf{T}^T = \begin{pmatrix} \sigma_z^{02} + (t \sigma_v^0)^2 & t \sigma_v^{02} \\ t \sigma_v^{02} & \sigma_v^{02} \end{pmatrix}. \quad (2.15)$$

As expected, the velocity spread stays unaltered ( $\sigma'_v = \sigma_v^0$ , see Fig. 2.2) and therefore same for the energy spread  $\Delta E' = \Delta E_0$ . The pulse length however changes according

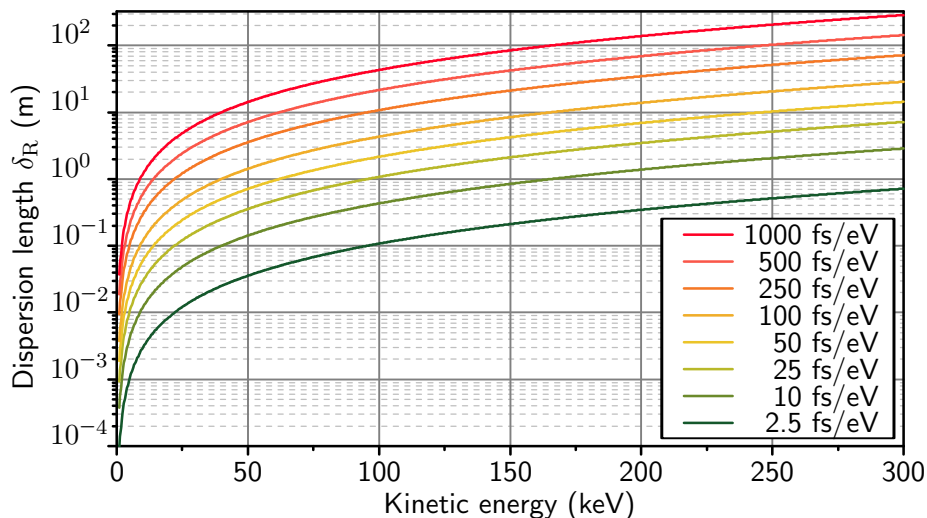


**Figure 2.3:** Dispersion length  $\delta_R$  of an electron pulse as function of kinetic energy for various ratios of initial pulse duration to energy spread (see legend). The energy spread is assumed to be small compared to the mean kinetic energy (Eq. 2.4).

to

$$\sigma'_z(t) = \sigma_z^0 \sqrt{1 + \left(\frac{t}{\tau_R}\right)^2}, \quad (2.16)$$

with

$$\tau_R = \frac{\sigma_z^0}{\sigma_v^0}. \quad (2.17)$$

Equation 2.16 states that the pulse lengthens first slowly and then approximately linear with propagation time. The key parameter is  $\tau_R$ , which is the propagation time for which the pulse length increases by a factor of  $\sqrt{2}$ . In analogy to optical Gaussian beams, we refer to this parameter as the *Rayleigh time*. It is given by the ratio of uncorrelated pulse length to velocity spread (Eq. 2.17).<sup>4</sup>

The *dispersion length*  $\delta_R$  corresponding to  $\tau_R$ , as the propagation distance for which the pulse duration increases by a factor of  $\sqrt{2}$  is given by

$$\delta_R = v_0 \tau_R \approx (\beta_0 \gamma_0 c)^3 m_e \frac{\Delta t_0}{\Delta E_0} \quad (2.18)$$

and an electron pulse of initial duration  $\Delta t_0$  propagating over a distance  $d$  changes accordingly as

$$\Delta t' = \Delta t_0 \sqrt{1 + \left(\frac{d}{\delta_R}\right)^2}. \quad (2.19)$$

<sup>4</sup>The relations expressed in Eqs. 2.16 and 2.17 are known as result of the analogue derivation in transverse particle phase space, where the equivalent to the optical Rayleigh length is the  $\beta$ -Twiss parameter [120, 121].

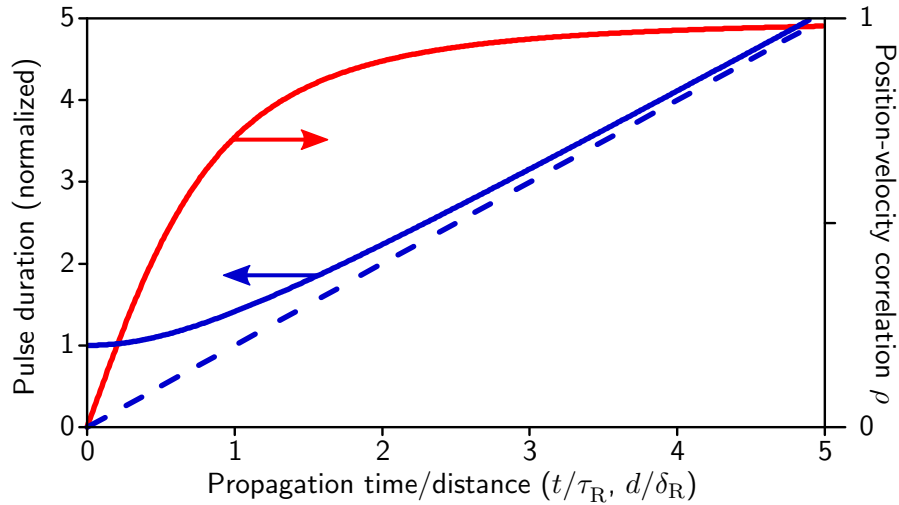


**Figure 2.4:** Evolution of electron pulse duration (blue, left axis) and position-velocity correlation (red, right axis) with propagation time (distance) relative to Rayleigh time (dispersion length). The blue, dashed line indicates linear pulse broadening.

Figure 2.3 shows  $\delta_R$  as a function of mean kinetic energy for various ratios of initial pulse duration to energy spread ( $\Delta t_0/\Delta E_0$ ; see legend). Due to the strong scaling with the third power of  $\beta_0\gamma_0$ , low energy electron pulse in general disperse much quicker than high energy electron pulses of same bandwidth ratio. For typical (uncompressed) electron pulses for UED/UEM (100 keV,  $\sim 100$  fs,  $\sim 1$  eV)  $\delta_R$  is on the order of a few meters. Even though typical electron beam lines are much shorter in length, the pulses there can only be assumed weakly correlated, unless other pulse broadening mechanisms, such as acceleration in an electrostatic field [110] and/or space charge effects [123, 124], have to be taken into account.

Not only the pulse duration increases during propagation, also correlations between position and velocity emerge. Intuitively, it is obvious that after some propagation time the particles of highest velocity or energy in the pulse are in the leading part of the pulse, whereas slower electrons with less kinetic energy are found in its trailing part (see Fig. 2.2). From the linear off-diagonal, i.e., the covariance terms in Eq. 2.15, we find for the correlation coefficient via Eq. 2.9:

$$\rho = \frac{\sigma'_{zv}}{\sigma'_z\sigma'_v} = \frac{t}{\sqrt{t^2 + \tau_R^2}} = \frac{d}{\sqrt{d^2 + \delta_R^2}}. \quad (2.20)$$

Correlations between position and velocity do not evolve linearly in time or propagation distance and again the Rayleigh time  $\tau_R$  (dispersion length  $\delta_R$ ) is the decisive parameter. Only for  $t \ll \tau_R$  (positive) correlation between position and velocity increases approximately linearly in time, with a slope given by  $1/\tau_R$ . If the pulse travels for times much longer than  $\tau_R$  the correlation  $\rho \approx 1$  and hardly changes. The

Rayleigh time thus can be regarded as the propagation time over which correlations emerge and for which the pulse roughly maintains its duration.

Figure 2.4 shows the evolution of correlation (Eq. 2.20) and pulse duration (Eqs. 2.16 and 2.19) in unitless form (red and blue curves, respectively). The expected resemblance with the focusing characteristics of Gaussian laser beams is apparent. The linear broadening of the pulse for  $t \gg \tau_R$  is indicated by the blue dotted line. Furthermore, we see that the pulse duration is minimized at  $t = 0$ , where the phase space is uncorrelated.

The preceding discussion highlights pulse propagation as a source of (positive) correlation, which leads to temporal broadening of an uncorrelated electron pulse. Conversely, for a negatively correlated electron pulse, propagation reduces the amount of correlation, leading to a shortening or temporal compression of the electron pulse in time. In the following section we will see how this can be realized and described within our framework.

## 2.4 Phase space preparation with temporal lenses

A temporal or longitudinal lens is an electron optical tool to manipulate the longitudinal velocity distribution of an electron pulse along its propagation coordinate. It can be used, for example, to slow down the leading part of an electron pulse and to accelerate its trailing part and vice versa. Consequently, the velocity-position correlation within the electron pulse is altered along with the velocity distribution. The temporal shape, however, stays the same. Only if such a pulse propagates further, these initial correlations will lead to a change in pulse length, that is, the pulse is focused or defocused in time.

Because the velocity modulation by a temporal lens occurs along the propagation coordinate of the electron pulse, its underlying mechanism must be time-varying. In practice, temporal lenses are established by the controlled interaction of a charged particle with an electromagnetic field. The integrated Lorentz force acting on a charged particle can alter the particle's momentum as a function of its arrival time.

Temporal lenses were first proposed and realized with gigahertz fields in suitable microwave cavities [57, 63, 61, 64], but they have now also been demonstrated with optical fields at low terahertz [89, 105, 95] (see Chapters 4 and 7) and infrared frequencies [43–45]. The tailored interaction of an electromagnetic wave with a particle beam is an area of active research interest (see for example Refs. [79, 83, 104]) and subject of Chapter 6 in this thesis.

For the phase space description of the action of a temporal lens, we assume it to impose a spatially linear change of forward velocity on the electron pulse of the form

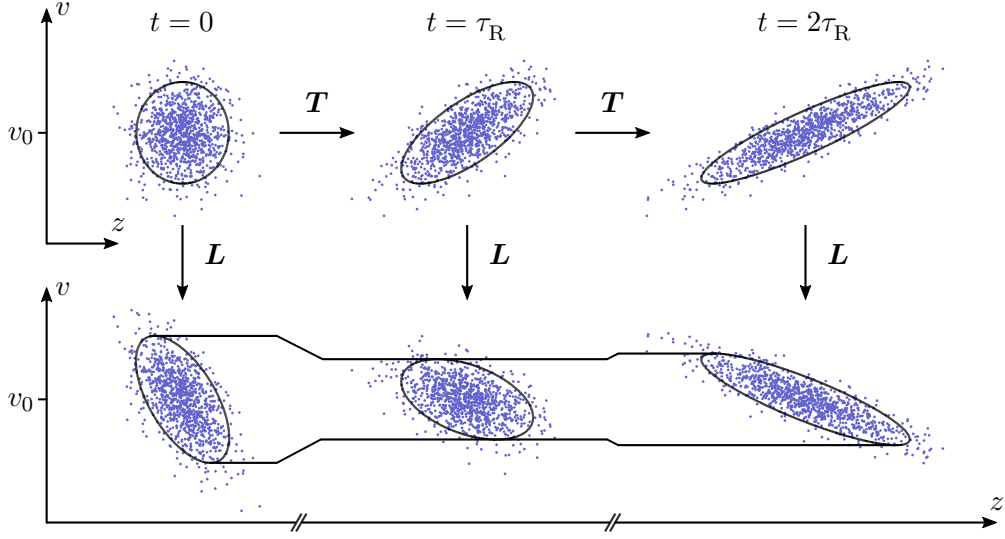


**Figure 2.5:** The effect of the same temporal lens on electron pulses after different stages of propagation. The temporal focal length is equal for all three cases. Velocity spread and therefore energy bandwidth is increased, decreased or unaltered (from left to right) depending on the amount of acquired correlation between position and velocity in the pulse.

$$\mathbf{P}' = \begin{pmatrix} Z \\ V - g_v \cdot Z \end{pmatrix} = \mathbf{L}\mathbf{P}_0, \quad (2.21)$$

with the temporal-lens matrix

$$\mathbf{L} = \begin{pmatrix} 1 & 0 \\ -1/f_t & 1 \end{pmatrix}. \quad (2.22)$$

The *compression strength*  $g_v$  is the inverse of the temporal focal length  $f_t$ . Here, both are expressed in temporal units.<sup>5</sup> The minus sign in the above equation is chosen to follow the convention that positive compression strengths (positive temporal focal lengths) lead to a temporal compression of an uncorrelated electron pulse. The optical analogy is a positive lens which focuses a collimated beam. A negative temporal lens can be established by switching the polarity or changing phase of the driving field, for example. In reality the assumption of linear phase space transformation is approximately fulfilled for electron pulses of durations shorter than a half period of the modulation frequency (see Chapter 1).

Figure 2.5 depicts modulated phase space representations of an initially uncorrelated electron pulse after different propagation times and therefore with different

<sup>5</sup>For different choices of phase space coordinates, such as time-energy [64, 89] or position-momentum [104], compression strength— $g_E$  and  $g_p$ , respectively—is expressed in the according units.

degrees initial of correlation. The (positive) compression strength in the three cases is always the same ( $f_t = 1.3\bar{3}\tau_R$ ). We observe that the final velocity spread is different in each case. For  $t = 0$  the initial phase space is uncorrelated and the action of the temporal lens increases the velocity spread and induces negative correlation. For the positively correlated pulse that is obtained after a propagation time  $\tau_R$  the velocity spread is decreased and so is the absolute value of correlation (central part of Fig. 2.5). For  $t = 2\tau_R$  velocity spread and correlation is of nearly same absolute value as before the modulation, but the sign of the correlation is inverted. Subsequent propagation of this pulse would lead to a decrease in pulse duration until the phase space resembles the initial phase space at  $t = 0$ . As we will see in the next section, the velocity spread which is induced by the temporal lens determines the minimum pulse duration.

Thus, for a complete description of electron pulse compression in phase space we need to consider not only the action of the temporal lens, but also propagation effects and the build up (or removal) of correlation before and after the velocity modulating element, i.e. the temporal lens. This is the subject of the following section.

## 2.5 Imaging with temporal lenses

The similarities in focusing behaviour of optical lenses and temporal lenses have been noted already in the early days of ultrafast electron diffraction and microscopy [125]. An imaging equation for temporal lenses, which incorporates pulse propagation times before and after the temporal lens ( $t$  and  $t'$ , respectively), has been given by Hilbert et al. [126], namely

$$\frac{1}{f_t} = \frac{1}{t'} + \frac{1}{t}. \quad (2.23)$$

This equation is the temporal lens analogue to the ray optical description of image formation with a thin optical lens of focal length  $f_{\text{opt}}$ . The corresponding optical equation is obtained by replacing the object (image) propagation time  $t$  ( $t'$ ) by object and image distances  $s$  and  $s'$ , respectively.

For Gaussian laser beams, the optical thin-lens formula has been extended by Self [127] to incorporate beam size effects and the (transverse) Rayleigh length  $z_R$  of the beam. It is given by

$$\frac{1}{f_{\text{opt}}} = \frac{1}{s'} + \frac{1}{s + z_R^2/(s - f_{\text{opt}})}. \quad (2.24)$$

In this section we derive a similar relation for imaging with temporal lenses that goes beyond Eq. 2.23 in that it includes the Rayleigh time  $\tau_R$  and therefore realistic beams with finite energy spread and pulse duration.

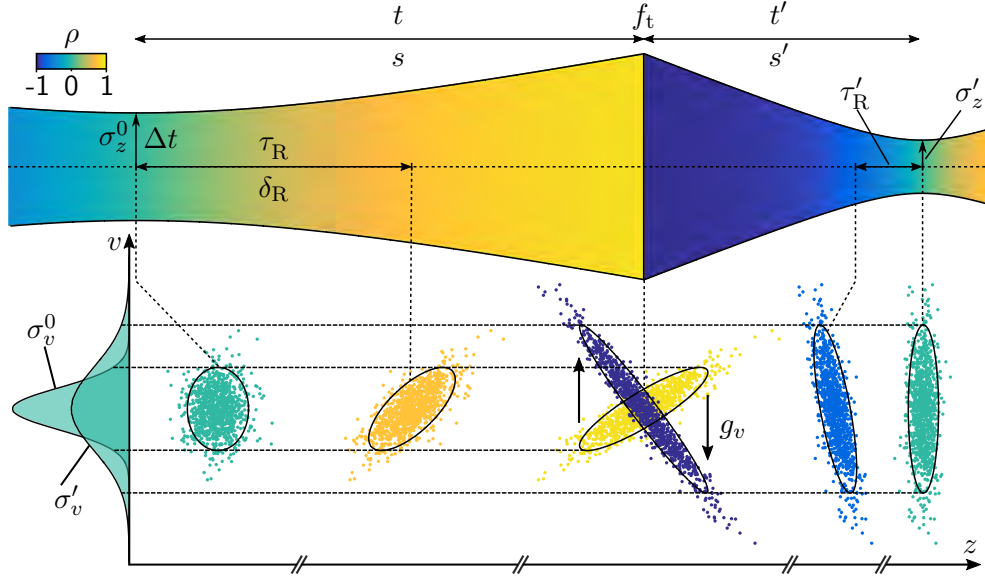


**Figure 2.6:** Temporal lens imaging geometry of electron pulse compression. The upper panel depicts the evolution of pulse duration and position-velocity correlation  $\rho$  (colorcode). The lower panel shows selected phase space representations and the projected velocity distribution before and after the temporal lens ( $f_t$ ).

### 2.5.1 The temporal lens equation

Figure 2.6 shows geometry and phase space representation for temporal lens imaging. Following Self's approach [127], we treat the temporal waist of the electron pulse before the lens as object with pulse length  $\sigma_z^0$  and velocity spread  $\sigma_v^0$ . As we have seen in Section 2.3, at this point there is no correlation between position and velocity of the particles in the pulse (see the green phase space representation in the lower panel of Fig. 2.6). The object Rayleigh time is  $\tau_R = \sigma_z^0/\sigma_v^0$ . The image is formed by propagation of this pulse for a time  $t$  to a temporal lens of strength  $g_v = 1/f_t$ . Upon propagation, a positive correlation  $\rho$  between position and velocity emerges (see color code). After the temporal lens the pulse propagates for a time  $t'$  until correlations are removed again and the image is formed by another waist of the temporal pulse profile ( $\sigma_z', \sigma_v', \tau_R'$ ).<sup>6</sup>

In our matrix notation this transformation from image to object phase space configuration ( $\mathbf{P}_{\text{obj}}$  to  $\mathbf{P}_{\text{img}}$ ) is given by

$$\mathbf{P}_{\text{img}} = \underbrace{\mathbf{T}' \mathbf{L} \mathbf{T}}_{=\mathbf{M}_{\text{img}}} \mathbf{P}_{\text{obj}}, \quad (2.25)$$

<sup>6</sup>In general, as in the optical case, object and image do not necessarily need to be real and  $t$  ( $t'$ ) can also take negative values.

<sup>7</sup>Here we use the shorthanded notation  $\mathbf{T}' = \mathbf{T}(t')$  and  $\mathbf{T} = \mathbf{T}(t)$  (see Eq. 2.14).

with

$$\mathbf{M}_{\text{img}} = \begin{pmatrix} 1 - \frac{t'}{f_t} & t + t' - \frac{tt'}{f_t} \\ -\frac{1}{f_t} & 1 - \frac{t}{f_t} \end{pmatrix}. \quad (2.26)$$

Because the image phase space is also uncorrelated (see Fig. 2.6), the covariance matrix must remain diagonal under this transformation:

$$\Sigma = \begin{pmatrix} \sigma_z^{02} & 0 \\ 0 & \sigma_v^{02} \end{pmatrix} \xrightarrow{\mathbf{M}_{\text{img}}} \begin{pmatrix} \sigma_z'^2 & 0 \\ 0 & \sigma_v'^2 \end{pmatrix} = \Sigma'. \quad (2.27)$$

From the conservation of longitudinal emittance (see Eq. 2.12) it follows that the uncorrelated bandwidth product is conserved and thus

$$\sigma_z' \sigma_v' = \sigma_z^0 \sigma_v^0, \quad (2.28)$$

which is equivalent to

$$\Delta t' \approx \Delta t \frac{\Delta E}{\Delta E'}. \quad (2.29)$$

For typical energy spreads in UED, the latter approximation is very well justified [128]. Equations 2.28 and 2.29 state that the electron pulse duration changes in proportion to the relative change in energy bandwidth. Therefore, to obtain the shortest possible pulse duration, the energy gain must be as large as possible—or acceptable. Usually, in practice, this maximum energy gain is limited by the field strength of the electromagnetic wave that drives the temporal lens or its modulation period.

Demanding that the object and image phase-space are free of position-velocity correlations, expressed in Eq. 2.27 and using the covariance transformation rule (Eq. 2.10) allows us to find a relation between image and object pulse propagation times ( $t$ ,  $t'$ ) and the temporal focal length  $f_t$  (see Appendix A). The result is given by

$$\frac{1}{f_t} = \frac{1}{t'} + \frac{1}{t + \tau_R^2/(t - f_t)}. \quad (2.30)$$

This equation is the temporal lens imaging analogue to Self's Equation (Eq. 2.24) and has been derived in the course of this thesis. It is the generalization of Eq. 2.23 for beams of finite pulse duration and energy spread, which are both contained in  $\tau_R$  (see Eq. 2.17). As for the optical case [127] it converges to the ray optical equation, given by Eq. 2.23 [126] for  $\tau_R \rightarrow 0$ . Equation 2.30 allows to find the compression strength required for obtaining the shortest pulse duration for a given geometry. Its derivation, which is detailed in Appendix A, is only based on the assumption of uncorrelated image and object phase space and linear transformations. The fact

that it nevertheless resembles Eq. 2.24 for a perfectly coherent Gaussian laser beam is quite remarkable and in turn means that the formation of a beam waist even for a fully coherent beam can also be explained in the framework of correlations in a beam of incoherent particles. It suggests that for the given conditions, the imaging equations for the formation of a temporal waist also holds for the fully coherent case.

From Eq. 2.27 we furthermore obtain the magnification of the temporal lens system, that is, the degree of compression it offers. Its derivation can be found in Appendix A. Again, it resembles the expression for a Gaussian beam [127] and is given by

$$m = \frac{\sigma'_z}{\sigma_z^0} = \frac{\sigma_v^0}{\sigma'_v} = \frac{1}{\sqrt{[1 - (t/f_t)]^2 + [\tau_R/f_t]^2}}. \quad (2.31)$$

As we have seen before, the reduction in pulse length is equivalent to the increase in velocity (energy) bandwidth. Magnification of smaller 1 means pulse compression and bandwidth increase, whereas for  $m > 1$  the energy spread is reduced, that is, the beam is more monochromatic, but the pulse duration is increased. In Section 2.7 we will treat the latter case in more detail.

The Rayleigh time of the pulse after the temporal lens is given by

$$\tau'_R = \frac{\sigma'_z}{\sigma'_v} = m^2 \tau_R. \quad (2.32)$$

Equations 2.30 and 2.31 together with Eq. 2.32 fully describe the image formation of one or multiple temporal lens systems. They allow for the calculation of the final electron pulse duration for given input parameters of propagation distances, phase-space correlation, velocity/energy spread and pulse length/duration. Furthermore, the equations are invariant under the substitutions:  $t \rightarrow s$ ,  $t' \rightarrow s'$ ,  $f_t \rightarrow f_z$  and  $\tau_R \rightarrow \delta_R$ , meaning that they can also be expressed in spatial units.

Unlike in optics (Eq. 2.24), where focal lengths of individual lenses are usually fixed and image and object distances  $s$  and  $s'$  can be varied more easily, for electron pulse compression it is usually the distances (and therefore the pulse propagation times), which are fixed. Adjustments are usually performed by changing the compression strength  $g_v = 1/f_t$  as for example in Refs. [64, 89, 105]. Equation 2.30 gives this required compression strength as a function of the experimental parameters, which when combined with Eq. 2.31 allows us to predict the pulse duration in the temporal focus. For instance, when taking the parameters of the pulse compression experiment demonstrated in Chapter 7,<sup>8</sup> we obtain a predicted FWHM electron pulse duration in the temporal focus of 24 fs. This is in quite good agreement with the actually

---

<sup>8</sup>These are: kinetic electron energy of 75 keV, uncorrelated energy spread of 1.3 eV (FWHM), initial pulse duration of 490 fs (FWHM), object and image distances of 0.4 m and 0.5 m, respectively.

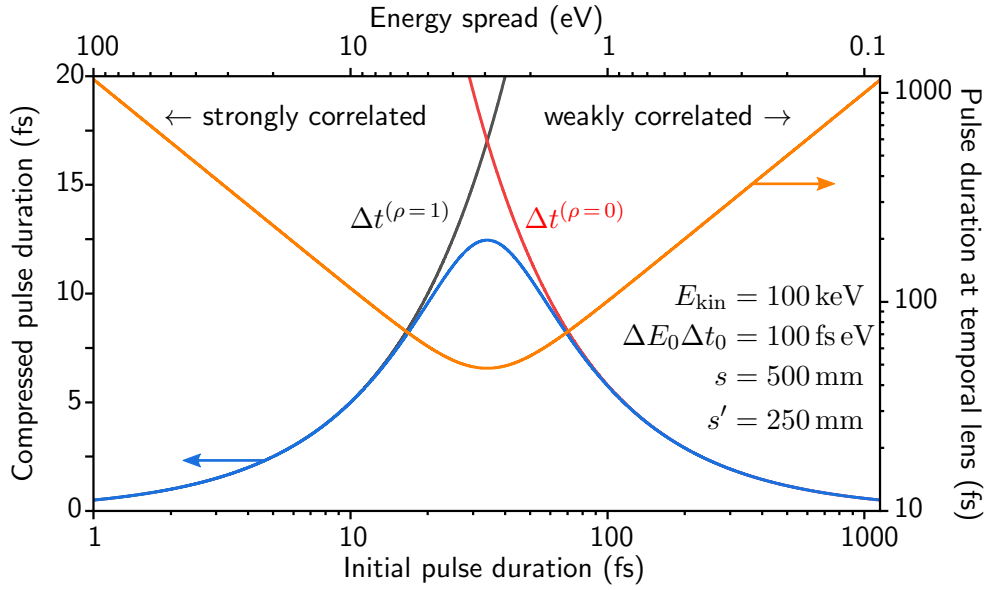


**Figure 2.7:** Minimum compressed pulse duration (image pulse duration, blue line) according to Eqs. 2.30 and 2.31 as a function of initial (object) pulse duration for a pulse of constant emittance and parameters as given in the legend. The energy spread changes accordingly (upper axis). The pulse duration at the temporal lens is shown as orange line. Asymptotic cases of  $\rho = 1$  and  $\rho = 0$  are shown as black and red lines, respectively. All quantities are given as FWHM values.

measured value of 28 fs, given that the equations predict the shortest possible pulse duration for the actual experimental parameters.

### 2.5.2 Pulse compression with a single temporal lens

The capabilities of the temporal lens imaging relations (Eqs. 2.30 and 2.31) are demonstrated exemplarily in Fig. 2.7. There, the compressed electron pulse duration (blue line) of a 100-keV electron pulse is plotted as a function of initial electron pulse duration and energy spread. The longitudinal FWHM-emittance of 100 fs eV is thereby kept constant. The orange line shows the electron pulse duration at the position of the temporal lens (right axis). Object and image distances are 0.5 m and 0.25 m, respectively.

Starting with an initially long electron pulse of small energy spread (all to the right), a reduction of initial pulse duration first increases the compressed electron pulse duration as, due to the constant emittance, the energy spread goes up. The compressed pulse duration has a maximum at the point when the dispersion length  $\delta_R \propto \Delta t_0 / \Delta E_0$  (Eq. 2.18) equals the object distance  $s$  (see also Fig. 2.6). At this point the pulse duration of the electron pulse at the position of the temporal lens

(orange line) is minimal. For longer initial electron pulses, the pulse duration at the temporal lens is approximately equal to the initial pulse duration and the pulses therefore are only weakly correlated.

To the left of the maximum in Fig. 2.7, that is, for a further reduction of the pulse duration at the cost of increasing energy bandwidth, we again observe a decrease in the compressed pulse duration. This decrease is approximately linear in initial pulse duration for values  $< 10$  fs and does not depend on the energy spread. In this regime, the energy spread, however, determines the pulse duration at the temporal lens as now the dispersion length is much shorter than the object distance ( $\delta_R \ll s$ ). The particles in the pulse are therefore highly correlated in position and velocity at the temporal lens.

The black and red lines in Fig. 2.7 depict the compressed pulse duration in the asymptotic cases of  $\rho = 1$  ( $\tau_R \rightarrow 0$ ) and  $\rho = 0$  ( $t = 0$  and  $t' = f_t$ ) at the temporal lens, respectively. The two traces give good approximations to the final pulse duration in the temporal focus unless  $\delta_R \approx s$  (center part of Fig. 2.7). The compressed pulse duration in the two cases is given by

$$\Delta t^{(\rho=0)} \approx \Delta E_0 \frac{s'}{m_e (v_0 \gamma_0)^3} \quad (2.33)$$

and

$$\Delta t^{(\rho=1)} = \Delta t_0 \frac{s'}{s}. \quad (2.34)$$

In the uncorrelated regime (Eq. 2.33), the compressed pulse duration is mainly determined by the initial energy spread of the electron pulse  $\Delta E_0$  and in particular independent of the initial electron pulse duration. A reduction in compressed pulse duration in this regime can be achieved by a decrease in energy bandwidth at the source and/or higher electron pulse energies. For electron beam lines with negligible pulse broadening during acceleration [110], this is the regime of relevance due to the naturally large Rayleigh times (see Fig. 2.3).

In the correlated regime (Eq. 2.34), on the other hand, the minimum compressed pulse duration is independent of any energetic parameters. The magnification of the initial pulse of width  $\Delta t_0$  is solely determined by the geometric ratio of image and object distance. This case is identical to the geometric ray optics picture [126] and the focal distance is given by Eq. 2.23. In reality, we find this situation for rather short and broadband electron pulses and/or large propagation distances. Space charge and (slow) acceleration of the electron pulse enhance correlations [123, 110], but because these effects generally also lead to a nonlinear deformation of phase space, their treatment is beyond the framework presented here. Nevertheless, even then Eq. 2.34 may still yield a good first approximation and qualitative insight.

When it comes to designing a temporal lens setup for electron pulse compression, one needs to first consider which regime is the best and realistic to work in. To this end an estimation of energy spread, initial pulse duration and acceleration/propagation effects is in order. For some applications it might be best to work with comparably long initial electron pulses, if it allows for generation of narrow-band initial electron pulses that are only weakly correlated at the compressor. This is especially the case for high energy electron pulses. Conversely, the correlated regime offers independence from energetic effects and thus works equally well at any acceleration voltage. Using few-femtosecond or even attosecond laser trigger pulses here is beneficial as it allows for achieving shortest compressed electron pulse durations—even if this comes at the cost of large bandwidth.

The here derived equations govern electron pulse compression and temporal imaging dynamics. They are the basis for design of a temporal lens setup. In practice, however, often timing uncertainties (jitter) as well as energy fluctuations limit the achievable electron pulse duration. We treat these effects in the following section.

### 2.5.3 Susceptibility to timing jitter and energy fluctuations

The case distinction by the degree of propagation-induced correlation at the temporal lens, as we did in the previous section, is also instructional when it comes to the question of influence of timing jitter and energy drifts, which often set the practical limit for the compressed electron pulse duration.

From Eqs. 2.33 and 2.34 we know that the compressed pulse duration in the uncorrelated regime is determined by the initial energy spread of the electron pulse, whereas in the correlated regime it is proportional to the initial pulse duration. The same dependencies apply to the case of initial energy and timing offsets  $\delta E$  and  $\delta t$ , respectively. The temporal shifts  $\delta t'$  of the compressed electron pulse are thus given by

$$\delta t'_{(\rho=1)} = \frac{s'}{s} \delta t, \quad (2.35)$$

$$\delta t'_{(\rho=0)} \approx \frac{s' \delta E}{m_e (\beta_0 \gamma_0 c)^3}. \quad (2.36)$$

This behavior can be visualized by invoking a lens picture as shown in Fig. 2.8. In panel a, the case of an uncorrelated electron pulse at the temporal lens is depicted as ray diagram. It is analogue to the case of a infinite object conjugate and finite image conjugate, that is, a collimated beam focused by a thin lens. All rays that are parallel to the (temporal) optical axis (black lines) represent mono-energetic trajectories which arrive simultaneously at the temporal focus, regardless of their initial offset in time ( $\delta t$ ). In other words, a pulse that is initially delayed in time arrives later at

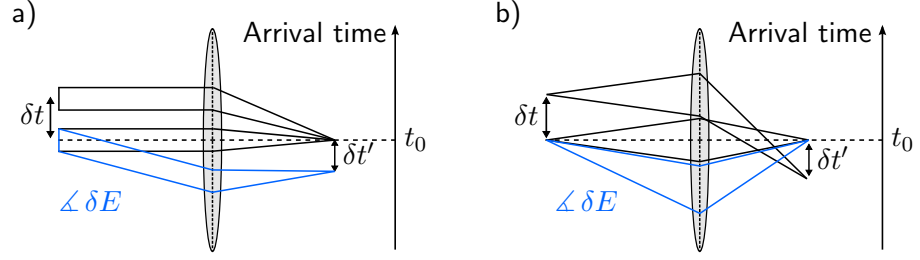


**Figure 2.8:** Temporal lens model for visualization of timing jitter and energy fluctuations. a) Uncorrelated case. Initial delays  $\delta t$  of pulses of equal energy are compensated by the temporal lens (black lines). Pulses of different energy arrive at different times  $\delta t'$  at the position of the temporal focus (blue lines). b) Correlated case. The timing of pulses arriving at the temporal focus depends on the initial timing (black lines) and is independent of energy fluctuations (blue lines).

the temporal lens and obtains a velocity kick, which just compensates for the initial lag. This additional velocity kick allows the pulse to arrive at the same time as an undelayed pulse would have arrived, albeit with a higher velocity, corresponding to a larger angle with the temporal optical axis. Conversely, an electron pulse with a small energy offset ( $\delta E$ , blue lines) arrives with a temporal offset  $\delta t'$  at the temporal focus.

The opposite behavior is true for the case of a strongly correlated pulse at the temporal lens, as depicted in Fig. 2.8 b. Here, initial temporal shifts affect the pulse's arrival time at the temporal focus, whereas energy offsets (blue) are irrelevant.

When it comes to achieving the shortest possible pulse duration, it is in both cases beneficial to work at shortest possible image distances. Not only will the compressed pulses be shorter than (see Eqs. 2.34 and 2.33), but also the susceptibility to fluctuations of any kind have less influence on the electron pulse arrival time. Short imaging distances imply short focal lengths and in turn high compression strengths, which may not be realistic to achieve (especially for low modulation frequencies, see Section 2.4). Therefore, when designing a pulse compression experiment an estimation of  $\delta t$  and  $\delta E$  is necessary.

For example, let us assume a high voltage power supply for the electron source, which is known to drift by  $\pm 1$  V at a central voltage of 30 kV. With a distance of 0.5 m between temporal lens and temporal focus, this will lead to timing fluctuations of  $\pm 78$  fs for an uncorrelated pulse ( $t \ll \tau_R$ ). Increasing the central voltage to 100 kV reduces this susceptibility to 12 fs/V. If, however, the timing stability between pump and probe pulse is known to be even better than that, it is worthwhile considering working in the correlated regime. This is possible and particularly advantageous if the initial electron pulse duration can be made very short, that is, on the order of  $\delta t$ .

Then, even at moderate magnifications  $\sim 1$ , temporally robust electron pulses can be expected.<sup>9</sup>

For the above considerations we have assumed a temporal lens, whose modulation is stable in time.<sup>10</sup> In reality, however, also the time varying electromagnetic field, which is inherent to a temporal lens, may exhibit significant fluctuations in time relative to the electron pulse. Therefore, the above values for arrival time jitter are understood as relative to the timing of the temporal lens ( $t_0$ , see Fig. 2.8). Because such temporal lens induced fluctuations are usually uncorrelated to the initial electron pulse fluctuations, it a high degree of stability between the optical pump pulse and the temporal lens is crucial. While microwave-based temporal lenses usually need elaborate synchronization schemes [129, 66, 67] to this end, all-optical schemes offer a high degree of passive synchronization [89, 105] up to interferometric stability [44, 100, 45]. In Section 2.6, a possibility to overcome this source of fluctuation is proposed.

We furthermore can make use of the energy dependence of Eq. 2.36 to detect energy modulations, which occur in between the electron source and the temporal lens. We will encounter this equation in the context of all-optical time-of-flight electron energy analysis in Chapter 5, albeit as result of a complementary derivation.

## 2.6 Application I: the multistage compressor

In the previous sections we have outlined the basics for electron pulse compression in the longitudinal phase space picture. Now we apply our formalism to the subsequent application of multiple temporal lenses for electron pulse compression. The use of such a multistage compressor has been suggested in literature [89, 130, 45] to overcome the limitations of current electron pulse compression schemes, but has neither been realized yet, nor investigated analytically.<sup>11</sup> Such an assembly involving two temporal lenses for electron pulse compression offers great potential not only for the compressed pulse duration, but also in terms of timing stability.

As we have seen in Section 2.5, working with shortest possible distances  $s'$  between temporal lens and temporal focus is advantageous for achieving shortest compressed electron pulse durations (see Eqs. 2.33 and 2.34 in Section 2.5). Also in this case the susceptibility to timing jitter and energy fluctuation is reduced (see Eqs. 2.35 and 2.36

---

<sup>9</sup>This is under the assumption that the additional timing offset caused by the change in the acceleration potential can be neglected. For typical parameters such as  $U_{\text{acc}} \sim 100$  kV and acceleration distances  $\sim 1$  cm, this shift is well below 1 fs/V.

<sup>10</sup>The expression “stable in time” here refers to the stability of the temporal lens with respect to a clock at the temporal focus, which is usually, represented by an optical pump pulse.

<sup>11</sup>Simulations for special cases, however, have been published. See for example the Supplementary material of Ref. [45].

in Section 2.5.3). However, short imaging distances imply high compression strength, which may not be realistic at arbitrary modulation frequencies, especially in the low terahertz range. On the other hand, low modulation frequencies are preferred for the compression of isolated electron pulses. In particular, the electron pulse duration should be shorter than a half-cycle of the modulation.

For keV-electron beams, temporal focal lengths on the order of millimeters were achieved with near-infrared modulation fields [43, 44] and ponderomotive schemes have been demonstrated to allow pulse compression over a drift distance of only tens of micrometers [45]. Because in all of these experiments the initial electron pulse duration is much larger than the modulation period, trains of electron pulses with attosecond duration emerge. Even though these pulses have turned out suitable for attosecond electron diffraction and microscopy [44], their application is restricted to the study of repetitive cycle dynamics. In order to cover the whole range of laser induced phenomena, bridging the gap between cycle-induced (attosecond) dynamics and fluence-dependent (femtosecond/picosecond) dynamics, isolated attosecond electron pulses are required as probe.

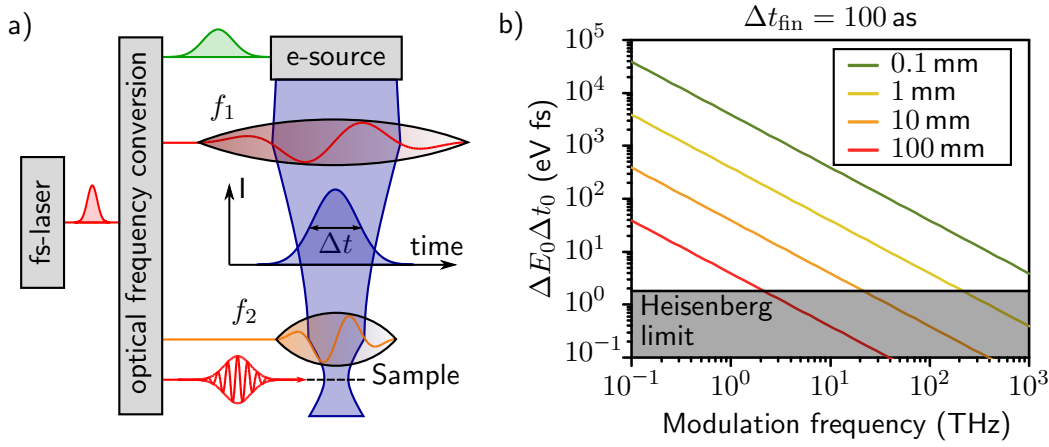
The schemes of Refs. [43–45] in principle allow for the generation of isolated attosecond electron pulses, but they require a sufficiently short input electron pulse duration, namely in the few-femtosecond range.<sup>12</sup> An additional temporal lens prior to the final compression stage offers a possibility to fulfill this requirement.

Figure 2.9 a shows a conceptual drawing on how to achieve sub-femtosecond electron pulses using two subsequent temporal lenses. The concept is driven by a single laser source, whose output is split into different parts. Because in each arm the optical frequency demands for the experiment are different, suitable wavelength conversion schemes are required. The electron pulses are triggered by optical pulses with a mean photon energy (or multiples thereof) closely matching the cathode material’s work function in order to minimize energy spread. The laser pulse duration there is chosen as to obtain the best possible compromise between the optical and electron pulse bandwidth [110]. Those two requirements can for example be met by virtue of a noncollinear optical parametric amplifier (NOPA) [111].

The first, pre-compressing temporal lens is established close to the output of the electron source and provides a low-frequency modulation of the longitudinal phase space with a temporal focal length  $f_1$  on the order of 1 m or less. It may be established by well-synchronized microwave cavities [64, 66, 67] or directly driven by low-frequency, terahertz fields using resonators (see Chapter 4), waveguides [95]

---

<sup>12</sup>This input electron pulse duration is ideally much shorter than a modulation half cycle such that the velocity change along the pulse is nearly linear. However, if a reduced pulse contrast is tolerable, input pulse durations larger than the optical half-period can be used (see Chapter 7).



**Figure 2.9:** Double-stage electron pulse compressor. a) Conceptual layout for electron pulse compression based on two temporal lenses. b) Longitudinal bandwidth product (FWHM) required for obtaining 100-as electron pulses as a function of modulation frequency for various temporal focal lengths (see legend). The precompressed electron pulses are assumed to be as long as a modulating half cycle.

or other symmetry-breaking elements such as an electron-transmitting metal mirror (see Chapters 6 and 7).

The pre-compressed electron pulse is then injected into a second temporal lens of shorter modulation period and substantially higher modulation strength, enabling a temporal focal length  $f_2 \sim 1$  mm. This last stage of compression is assumed to be perfectly, meaning for example interferometrically, stabilized with respect to an optical pump or characterization pulse, which locks the time zero of the experiment. The temporal lens realizations described in [43–45] all fulfill the above requirements for the second stage.

The temporal focus of the first temporal lens ( $f_1$ ) coincides with the position of the second temporal lens ( $f_2$ ), as depicted in Fig. 2.9 a. It implies that the object distance of the second lens is zero and therefore its magnification  $m_2$  given via Eq. 2.31 by

$$m_2 = \frac{f_2}{\sqrt{(\delta'_R)^2 + (f_2)^2}}, \quad (2.37)$$

where  $\delta'_R = m_1^2 \delta_R$  (Eq. 2.32) is the dispersion length after the first lens (magnification  $m_1$ , initial dispersion length  $\delta_R$ ). The final image distance  $s'_2$  (Eq. 2.24) reduces to

$$s'_2 = \frac{f_2}{1 + (f_2/\delta'_R)^2}. \quad (2.38)$$

Apparently, there is a maximum image distance of  $\delta_R/2$  for  $f_2 = \delta'_R$ , which means that the temporal focus must always be within a range  $s'_2 < \delta'_R/2$ . A temporal focus

further away cannot be generated. The magnification at this point is  $1/\sqrt{2}$ . With  $f_2$  increasing beyond  $\delta'_R$ , which is equivalent to a reduction in compression strength, the temporal focus moves towards the lens again, while the magnification converges to 1, that is, no compression at all.

To go from the few-femtosecond into the attosecond regime of electron pulse duration, we are more interested in the opposite case of strong compression, that is, low magnification ( $m_2 \ll 1$ ), which is equivalent to  $f_2 \ll \delta'_R$  (strong temporal lensing). From Eq. 2.38 it follows that then  $s'_2 \approx f_2$ . The case is now analogue to the uncorrelated regime discussed in Section 2.5 and the compressed pulse duration is given by Eq. 2.33. Let us, however, express this relation in quantities, which are more relevant for our scenario, where the electron pulse length has already been precompressed to a value of  $\Delta t' = m_1 \Delta t_0$ . We find for the final pulse duration

$$\Delta t_{\text{fin}} = \frac{f_2 \varepsilon_z}{v_0^3 \Delta t'}, \quad (2.39)$$

where  $\varepsilon_z$  is the (conserved) longitudinal emittance (see Section 2.2). Equation 2.39 expresses the final pulse length  $\Delta t_{\text{fin}}$  after a multistage compressor independent of the parameters of the previous stages. It states that for the shortest electron pulses in the final temporal focus, the pulses incident on second lens should be as long as possible. As in practice, the acceptable pulse duration is set by the modulation period of the second temporal lens (see above), a small product of  $f_2$  and  $\varepsilon_z$  is required.

In Fig. 2.9 b, the required longitudinal bandwidth product  $\Delta E_0 \Delta t_0$  to obtain 100-as pulses is plotted against the modulation frequency of the temporal lens for electron pulses with kinetic energy of 100 keV. The electron pulses are assumed to be precompressed to the modulation's half cycle. Therefore the lines approximate the upper bandwidth limits for the given focal lengths (see legend). We observe that high modulation frequencies require small bandwidth products, which may not be possible to achieve or even violate the uncertainty principle (grey area). Fig. 2.9 b, therefore provides a quick overview of the limits of a double stage compressor based on Eq. 2.39.

Figure 2.10 a shows the evolution of the FWHM electron pulse duration  $\Delta t$  for a double-stage compressor with  $f_1 = 0.5$  m and  $f_2 = 1$  mm and electron pulse bandwidth products as given in the legend. The first lens is positioned 0.5 m from the (uncorrelated) source. It precompresses the electron pulse to few-fs duration. Because for the given parameters, the pulses at the first lens are uncorrelated, the pulse duration is proportional to the initial energy spread and temporal focal length. This product sets the maximum possible modulation frequency of the final stage (see Eq. 2.33). Furthermore, we observe that the final, minimum pulse duration after the second lens is determined by initial pulse duration  $\Delta t_0$ . In general, assuming uncorrelated input pulses at both lenses, we can simplify Eq. 2.39 via Eq. 2.33 and find

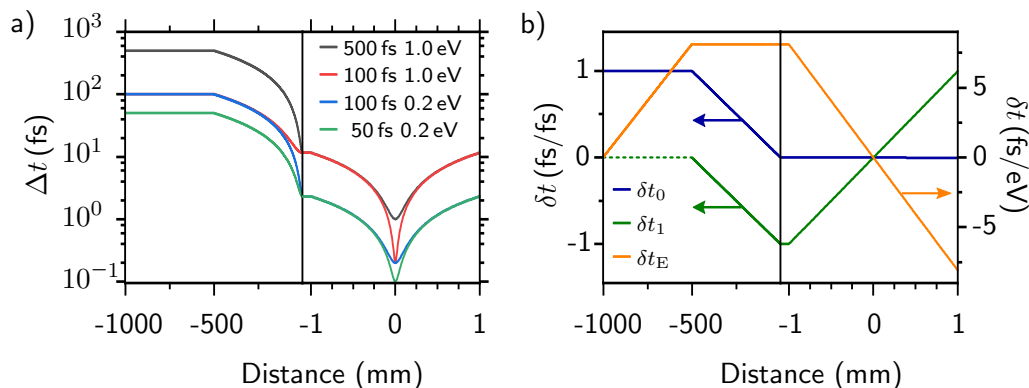


**Figure 2.10:** Performance of a double-stage electron pulse compressor. a) Evolution of electron pulse duration (FWHM) for various bandwidth products (see legend). The central energy is 100 keV. The first lens is at  $-500$  mm; the second lens is at  $-1$  mm (temporal focus at 0). b) Influence of various causes for electron pulse arrival-time jitter: initial pulse drifts (blue, left axis), fluctuations of the first temporal lens (green, left axis) and initial energy fluctuations (orange, right axis). All for the case of 100 fs eV and assuming linear phase-space transformations.

$$\Delta t_{\text{fin}} = \frac{f_2}{f_1} \Delta t_0. \quad (2.40)$$

Therefore for a sufficiently large ratio of the two temporal focal lengths it is possible to compress arbitrary pulses down to attosecond duration.

Let us now further analyze the timing stability of such a double-stage compressor. We assume the second stage to be stable with respect to an arbitrary time zero. In practice, this reference point is for example set by an optical pump pulse or the phase of a pulse characterization scheme (see Chapter 4). Because the electron pulse incident on the second temporal lens is uncorrelated, it is not susceptible to timing variations of the incoming (pre-compressed) electron pulse (see Section 2.5.3 and Fig. 2.8), which suggests a high temporal robustness of this electron pulse compression scheme.<sup>13</sup> However, electron pulses with a temporal offset with respect to the first stage will get a velocity kick changing their mean velocity, which influences the final pulse's timing and therefore needs to be taken into account. This can be done by virtue of the jitter-susceptibility approach introduced in Section 2.5.3 and extending it to incorporate two temporal lenses with variable offsets.

Figure 2.10 b shows the relative influence of timing drifts of electron pulses starting with an offset  $\delta t_0$  (blue line) or being out of phase with the first lens ( $\delta t_1$ , green line).<sup>14</sup> Initial offset in time are compensated for by the first lens and the blue line

<sup>13</sup>This conclusion has also been drawn (undergirded by simulations) by Kozák et al. [45].

<sup>14</sup>The depicted case is for  $\Delta t_0 = 100$  fs and  $\Delta E_0 = 1$  eV. Differences to the other three cases of Fig. 2.10 a are only minor.

goes to zero at the temporal focus (see Section 2.5.3). Offsets of the electron pulse with respect to the first lens, however, are increasing on the way to the first temporal focus, exhibiting a one-to-one relation there: the electron pulse will arrive with the same delay that it had with respect to the zero-crossing of the first lens. The second temporal lens compensates this offset and the green line crosses zero in the final temporal focus. This situation is similar to the effect of initial energy fluctuations on the electron pulse's timing (orange line). While they are maximum at the first temporal lens and its focus, also they go to zero in the temporal focus of the second temporal lens.

So not only timing drifts of optical components prior to the final temporal lens are compensated by this scheme, it is also robust against energy fluctuations as for example caused by an instable acceleration voltage. We can thus conclude: when it comes to the temporal stability of electron pulses, it is beneficial to apply a double-stage approach, if

- the temporal lenses are operated in the uncorrelated regime (low degree of correlation at the position of the lens, see Section 2.5),
- the timing stability of the first temporal lens is better than a half-cycle of the modulation period of the second lens and
- the second temporal lens is substantially stronger than the first ( $m_2 \gg m_1$ ) and stabilized to the global time zero of the experiment.

These requirements can be met by virtue of a combination of already demonstrated electron pulse modulation schemes, namely

- a high-acceleration-field electron source [115] to avoid position-velocity correlations at the first temporal lens,
- a first temporal lens, which can be stabilized on a few-fs level [66, 89, 105] and
- a second temporal lens with focal lengths of few millimeters and interferometric stability [43–45].

Such a double-stage compressor is then able to produce background-free, isolated attosecond electron pulses to be used for optical-pump-electron-probe studies with sub-fs-cycle resolution (see Refs. [48, 28] for proposed experiments).

## 2.7 Application II: the dynamic monochromator

So far we have treated temporal lenses foremost as tools for electron pulse compression, but the possibilities for longitudinal phase space modulation they provide

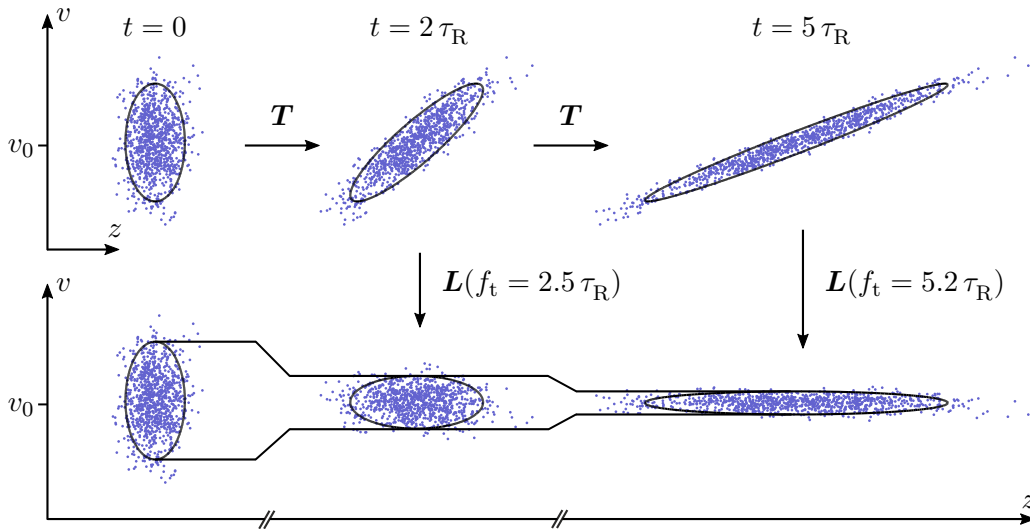


**Figure 2.11:** Reduction of electron pulse energy bandwidth with temporal lenses. Depending on the initial degree of correlation between position and velocity acquired during propagation, the electron pulse can be made more monochromatic after applying a temporal lens of appropriate strength (Eq. 2.41).

are broader than that—just like optical lenses can do more than just focus. Another application is to use a temporal lens for collimation instead of focusing, which corresponds to making the electron pulse more monochromatic.

A highly monochromatic electron beam is desired for many applications in conventional electron microscopy like electron energy loss spectroscopy (EELS) [131] or for avoiding chromatic aberrations in electron optical lens systems. To this end most modern (transmission) electron microscopes are equipped with monochromators [132].

Temporal lenses offer the possibility to decrease the energy or velocity bandwidth of an electron pulse. As we know from the conservation of emittance (Eq. 2.12) this benefit must come at the cost of increased pulse duration. The main idea behind this *dynamic monochromator* is illustrated in Fig. 2.11. An initially uncorrelated electron pulse propagates for a time  $t$  and correlations between positions and velocities of the particles within the pulse evolve which broaden the pulse in time (see Section 2.3). If we now apply a positive temporal lens of just enough strength to remove these correlations, the energy bandwidth is reduced, while the pulse remains stretched.

In our temporal lens imaging picture this is equivalent to making the image time  $t'$  equal to zero. The temporal waist then coincides with the temporal lens.<sup>15</sup>

<sup>15</sup>Depending on the degree of correlation, also imaging distances other than zero can be realized for bandwidth reduction. Such setting, however, will necessarily lead to a less monochromatic, but shorter pulse.

The required focal length to achieve this situation for an initially uncorrelated pulse having propagated for a time  $t$  can be found by virtue of Eq. 2.30, which yields

$$f_t^{(t'=0)} = \frac{t^2 + \tau_R^2}{t} = \tau_R \frac{1 + [t/\tau_R]^2}{t/\tau_R}. \quad (2.41)$$

Apparently, the temporal focal length that is required to collimate a pulse in time increases with propagation distance once it is beyond the Rayleigh time. Thus, for long and highly correlated pulses only weak temporal lenses are required to obtain a highly monochromatic beam.

From Eq. 2.28 we know that at a temporal waist a reduction of velocity spread is accompanied by a proportional increase in pulse length. The proportionality factor is the magnification (Eq. 2.31), which here is given by

$$m_{(t'=0)} = \sqrt{1 + \left(\frac{t}{\tau_R}\right)^2} \approx \frac{\Delta E_0}{\Delta E'}. \quad (2.42)$$

We see that for temporal collimation, the magnification is always greater unity. Therefore the pulse is longer than in the respective object waist of the system. If the temporal lens is placed within one Rayleigh time of the object waist, the relative reduction in velocity bandwidth is  $\sim 1$ . For a temporal lens further away ( $t \gg \tau_R \Rightarrow \rho \approx 1$ ), the bandwidth reduction, to a good approximation, scales inversely with propagation time or propagation distance  $d$ :

$$\Delta E' \approx \frac{\tau_R}{t} \Delta E_0 = \frac{\delta_R}{d} \Delta E_0. \quad (2.43)$$

The further away the point of collimation from the waist, the more monochromatic the beam becomes. The pulse duration is increased in proportion (Eq. 2.29). Still the pulse broadens upon further propagation, but now at a slower rate.

For some experimental configurations  $\tau_R$  ( $\delta_R$ ) might be too large to achieve a substantial reduction in energy spread over practical propagation distances (see Fig. 2.3). A way around this problem, is to decrease the initial pulse duration  $\Delta t_0$ , if possible. Because of the energy dependence of Rayleigh time  $\tau_R$  and dispersion length  $\delta_R$  (see Eq. 2.18), it is the initial pulse duration which determines the final energy width:

$$\Delta E' \approx \frac{(v_0 \gamma_0)^3 m_e}{d} \Delta t_0. \quad (2.44)$$

Intriguingly, even if a reduction of initial pulse duration comes at the cost of increased initial energy spread at the cathode [110], the final energy bandwidth decreases proportional to  $\Delta t_0$ .

Another way to achieve most monochromatic electron pulses other than by reduction of input pulse duration, is to use an additional, negative temporal lens prior

to the monochromator as, in similar fashion, first proposed by Verhoeven et al. for microwave modulation [133] and investigated for terahertz modulation in Chapter 5 of this thesis. Setting the first lens such that it disperses the electron pulse ( $t' < 0$ ) and hence decreases  $\tau_R$ , allows for a substantial reduction in electron bandwidth without additional propagation distance.

A practical limit to this kind of dynamic monochromator is imposed by the cycle duration of the velocity modulation of the temporal lens with frequency  $\nu$ . For simplicity assuming that the maximum tolerable pulse duration at the temporal lens is equal to half of the modulation period, we obtain a minimum final energy bandwidth of

$$\Delta E'_{\min} = 2\nu \Delta E_0 \Delta t_0. \quad (2.45)$$

The last two terms in this equation represent the bandwidth product of the electron pulse, which is proportional to its longitudinal emittance. Thus, to achieve the minimum possible bandwidth it is crucial to work at both low modulation frequencies (long cycles) and low longitudinal emittance. For typical values of  $\Delta E_0 \Delta t_0 = 100 \text{ fs eV}$  and  $\nu_t = 0.3 \text{ THz}$ , we obtain a minimum energy bandwidth (FWHM) as low as 60 meV, which already is comparable to the performance of static monochromators used in state-of-the-art transmission electron microscopes [132].

In Chapter 5 we will see a simulation of a terahertz-based multi-temporal-lens approach for electron energy analysis. There, we also take into account the nonlinearities of the modulation and achieve meV-scale energy resolution by mainly sacrificing signal strength.



# High-average-power, intense THz pulses from a LiNbO<sub>3</sub> slab with silicon output coupler

This chapter is dedicated to the generation of intense single-cycle terahertz (THz) pulses for electron pulse compression (see Chapters 4–7 and Refs. [89, 103–105]). The method of THz pulse generation by optical rectification in a slab of LiNbO<sub>3</sub> with a silicon output coupler described here is used for all temporal lenses realized in the course of this thesis.

## 3.1 Preface

The choice of a suitable source of electromagnetic radiation required for longitudinal phase space manipulation of ultrafast electron pulses (see Chapter 2) is crucial to the design of an electron pulse compression setup. Key parameters in this respect are (carrier) frequency, electromagnetic field strength and synchronicity with the electron pulses. Temporal lenses have been realized with different driving sources covering a broad spectral range from few GHz to hundreds of THz.

Microwave sources, on the lower end of spectrum, are well developed and in widespread use to manipulate charged particle beams in combination with appropriate resonator cavities. They have been used to accelerate [134], deflect (streak) [135–137], chop [138, 139], and compress (bunch) [63, 61, 64] electron pulses of up to relativistic energies, enabling ultrafast electron diffraction at high temporal resolution [9]. While the typical wavelength ( $\sim$  cm) and cycle duration ( $\sim$  ns . . . ps) of radio frequency (RF) sources comply well with the common dimensions of ultrafast electron pulses, their synchronization to electron pulses from laser driven sources

remains a challenge. Elaborate synchronization schemes for fast microwave phase adjustments [66,67] and a well-controlled laboratory environment [66] are inevitable prerequisites to this end.

Laser pulses in the visible and near-infrared spectral domain, on the other end of the spectrum, provide inherent synchronization to electron pulses from laser driven sources and can be very well drift corrected by interferometrical means. The attainable electromagnetic peak field strength exceeds their RF counterpart by orders of magnitude. To make use of these advantages, the momentum transfer from an optical pulse to a charged particle beam requires approaches that go beyond RF technology—most of which on their own trigger great scientific interest [73,78,76,44]. However, the large discrepancy between the optical period ( $\sim 1$  fs) and the duration of typical keV-electron pulses ( $> 100$  fs) makes it rather difficult to alter an electron pulse's momentum in a uniform fashion. Nevertheless, electron pulse trains made of spikes with subfemtosecond duration have been realized with such optical control fields [43–45].

At the intersection of the infrared and the RF spectral domain, there is the terahertz range, which is commonly considered to span frequencies from 0.1 THz to 10 THz or 3 mm to 30  $\mu\text{m}$  in wavelength, respectively. For electron pulse manipulation and control, terahertz radiation combines the advantages of both domains. With cycle durations of  $\sim 1$  ps and the accordingly long wavelengths, a whole electron pulse can be controlled within less than a single (half) cycle. Furthermore, THz pulses can be generated by all-optical means, that is, nonlinear frequency conversion processes such as difference frequency generation and optical rectification [140]. Therefore, the generated waveform is in sync with the driving laser pulse's envelope and usually of few-to-single-cycle nature, enabling peak field strengths  $> 10^5$  V/m (see Fig. 3.5)—sufficient for temporal lenses with focal lengths of tens of centimeters, see Chapters 4–7. All of these features render terahertz-based approaches for electron pulse manipulation a promising path towards future applications as also manifest by the increasing number of publications concerning that topic (see for example [90,89,99,95,103,104,96–98,105]).

Even though terahertz transients with peak electric field strengths on the order of  $10^{10}$  V/m have been realized [141], the attainable conversion efficiency of the underlying second order nonlinear process rarely exceeds a few percent [142] and is typically on the order of  $10^{-4}$  [88]. A limiting factor in that respect is the lack of suitable materials having a large second order nonlinear coefficient and simultaneously allowing phase matching [140]. There usually is a considerable difference between the group velocity of the optical pump beam and the terahertz phase velocity. In consequence, the source of THz radiation inside the material, which is the nonlinear polarization induced by and co-moving with the optical pump beam, quickly detaches from

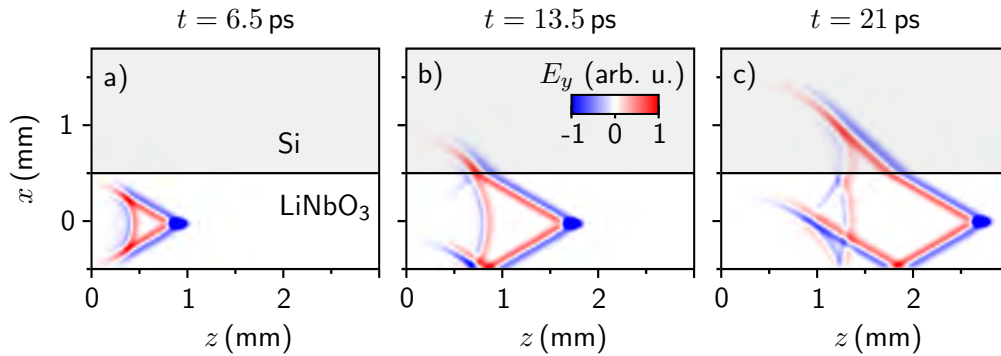


**Figure 3.1:** Visualization of single-cycle terahertz transient generation in a slab of  $\text{LiNbO}_3$  (FDTD simulation based on Ref. [147]). a) A pump laser pulse induces a bulletlike moving polarization (dark blue) via optical rectification in the nonlinear medium. The terahertz wave is emitted in a cone from this source. The  $y$  component of the electric field is shown in color scale. b) The terahertz wave is transmitted into the Si-prism with only minor losses. The lower interface fully reflects the wave. c) Field distribution in the structure after 21 ps of propagation in the medium. Two subsequent terahertz pulses are emitted.

the generated wave avoiding an efficient, collinear conversion (see Fig. 3.1). Various schemes have been realized to circumvent this effect, featuring for example the use of intensity-front tilted optical pump pulses [143], especially designed organic crystals [144] or wave-guiding structures [145, 146].

In the present chapter we make use of a conceptually simple approach to harvest the generated THz transient in an efficient way. The basic idea is to use a cylindrically focused optical pulse in a slab of  $\text{LiNbO}_3$  and couple out the non-collinearly generated THz (plane) wave by means of a silicon prism.

The principle of THz generation as described in this chapter is shown in Fig. 3.1. It depicts the results of a finite difference time domain simulation, solving Maxwell's equations as they are given in Ref. [147] for our experimental situation. Via optical rectification, the pump pulse induces a nonlinear polarization, which travels through the medium (dark blue). It is the source of the THz single-cycle transient, which is emitted in a double-sided cone from the pump pulse. The slab, in which the transient is generated, is covered with a Si-prism. It allows the THz wave to exit the crystal due to the nearly matching refractive indices of the two materials, which would be totally internally reflected (see lower cone), if the interface was air. The exit surface of the Si-prism is cut at an angle perpendicular to the THz wavefront as to reduce reflection losses when coupled out to air. It can be seen from the simulation and theory [147] that the emitted phase of the THz waveform is locked to the envelope of the optical pump pulse.

As in most non-collinear schemes, however, random pointing fluctuations of the pump beam result in a delay of the THz pulse, which is not (inherently) synchronized with electron pulses driven by the same laser source. This is especially severe for highly refractive THz materials such as LiNbO<sub>3</sub>. Geometrically, we find for our scheme a position dependent pulse delay  $\delta t$  of

$$\delta t = \left( \sqrt{n_{\text{THz}}^2 - n_{\text{gr}}^2/c} \right) \delta x \approx 15 \text{ fs}/\mu\text{m} \delta x, \quad (3.1)$$

where  $\delta x$  is the lateral pump beam displacement,  $c$  is the speed of light,  $n_{\text{THz}}$  and  $n_{\text{gr}}$  are the refractive index of the terahertz wave and the group refractive of the optical pump beam, respectively. Therefore a careful optical design minimizing beam waist pointing is mandatory for temporal-jitter-free operation. Possible routes around that are the use of collinear THz generation schemes or waveguides. As laser beam pointing can be measured fast and with high accuracy, active feedback on the pump pulse delay is another conceivable workaround.

In the light of its later use for electron pulse compression, this scheme offers striking advantages compared to, for example, tilted pulse front approaches. First of all, it is simple in its realization (see Fig. 3.2). Only requiring appropriate focusing optics and the LiNbO<sub>3</sub>-Si structure, it can be made very compact. The optimum focusing conditions and crystal geometry for most efficient THz generation are given in the article as Eq. 3.5–3.7 (see also Figs. 3.3 and 3.4). Other than tilted pulse schemes it does not require dispersive optics and accordingly large optical setups, which are more susceptible to drifts in pointing and timing. Furthermore, the slab-like structure facilitates heat removal and can therefore handle the large input average powers (see Fig. 3.7), which come with the comparably high laser pulse repetition rates required for femtosecond single electron diffraction (see Ref. [112] and Section 2.1). Lastly, the optical pump beam is hardly depleted (see Fig. 3.6). It can therefore be reused, for example for optical excitation of a UED sample or another THz generation stage.

A unique feature of the scheme is the adjustable peak THz frequency, which not only depends on the pump pulse duration, but also on the focusing parameters (see Eq. 3.3). In principle, this degree of freedom allows matching the THz waveform to the electron pulse duration or tune its peak frequency to the resonance frequency of a field enhancing structure (see Chapter 4).

All of the above features render this THz source our workhorse for isolated electron pulse manipulation. Slightly tweaked towards higher efficiency at lower input powers than described in the article, it is used for electron pulse compression with bow tie resonators (Chapters 4 and 5) and metal foils (Chapter 7) as well as for the generation of tilted electron pulses (Chapter 6). The use of two nearly identical THz generation stages for electron compression and temporal characterization passively

compensates timing fluctuations caused by beam pointing (Eq. 3.1) and allows for highest timing stability (see Chapter 7).

In the course of this thesis, the described terahertz transient generation scheme has been conceived, realized and studied in detail. The measurements strongly support the here developed theoretical predictions for peak frequency, power scaling and temperature dependence. The profound understanding of the underlying nonlinear processes, which have been gained in these experiments, allows finding the best pump beam parameters for the different laser sources used in this thesis and proves the versatility of this scheme. The results are originally published in Applied Physics B, Vol. 122, p. 30 in 2016.<sup>1</sup>

The following text (pp. 47–55) is a post-peer-review, pre-copyedit version of the article published in [102]. The final authenticated version is available online at: <http://dx.doi.org/10.1007/s00340-015-6315-6>.

---

<sup>1</sup>Author contributions: All experiments have been set up and conducted by MT and DE under the supervision of PB. Evaluation of THz and optical power measurements as well as electro-optic sampling (Figs. 3.3–3.6) by MT and DE. Evaluation of crystal heat deposition in LiNbO<sub>3</sub> (Fig. 3.7) by DE and PB. Theoretical treatment of THz generation by MT and of heat deposition by PB, both in discussion with DE. All authors interpreted the results and wrote the manuscript.



# High-average-power, intense THz pulses from a LiNbO<sub>3</sub> slab with silicon output coupler\*

Maxim V. Tsarev, Dominik Ehberger and Peter Baum

## Abstract

Many applications of THz radiation require high fields and high repetition rates at the same time, implying substantial average power levels. Here, we report high-power Cherenkov-type THz generation in a LiNbO<sub>3</sub> slab covered with a silicon prism outcoupler, a geometry in which the ratio between heat-removing surfaces and pump volume is naturally maximized for facilitating heat removal. At a conversion efficiency of 0.04 %, we achieve  $\sim 100$  times more output power than before with such geometry. Although about 10 % of the 15 W pump power is converted to heat via multi-photon absorption effects, the peak crystal temperature increases by only 8 K. This result is due to the focus' extreme aspect ratio of  $\sim 100$ , indicating the scalability of the approach to even higher average power levels. A line-shaped focus should be advantageous for removing heat in other optical conversions as well.

doi:10.1007/s00340-015-6315-6

© Springer-Verlag Berlin Heidelberg 2016

THz pulses (0.1—10 THz) at highest field strength and highest repetition rate are decisive for many spectroscopy and imaging applications, and highest average powers are therefore desirable. Optical rectification in LiNbO<sub>3</sub> (lithium niobate, LN) is particularly efficient, provided that the THz/pump phase/group velocities are matched, for example using tilted-intensity-front pulses [143, 142] or output couplers [145, 146, 148, 149]. Pulse energies of  $\sim 400 \mu\text{J}$  [143] and conversion efficiencies of 1.7 % [142] were obtained with tilted-front pulses. Waveguides [145, 146] are ideal for nJ-level pulses from laser oscillators with a record efficiency of 0.08 % in this regime [148]; using amplified 50- $\mu\text{J}$  laser pulses, 100-nJ THz pulses were achieved at a repetition rate of 1 kHz [149].

---

\*This is a post-peer-review, pre-copyedit version of the article published in [102]. The final authenticated version is available online at: <http://dx.doi.org/10.1007/s00340-015-6315-6>.

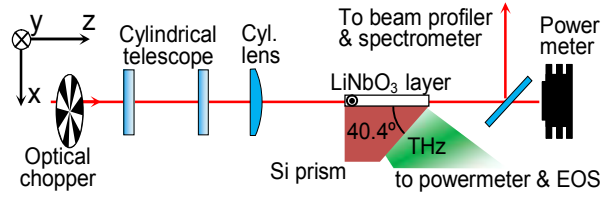


**Figure 3.2:** Experimental setup. 300- $\mu$ J, 15 W femtosecond laser pulses are cylindrically focused into a LiNbO<sub>3</sub> slab for THz generation. EOS, electro-optic sampling.

In most of the femtosecond optical-to-terahertz converters based on LiNbO<sub>3</sub> [143, 142, 148–151], the key limitations for efficiency are photorefractive damage of the crystal at a pump peak intensity of about several hundred GW/cm<sup>2</sup> [149] and, at lower intensities [142], free-carrier absorption of THz radiation [152]. However, in the regime of highest average power [153], LiNbO<sub>3</sub> can additionally be thermally damaged due to significant heat deposition caused by multi-photon absorption of the pump [150, 151]. Even before physical damage occurs, THz generation suffers from an increasing THz absorption coefficient at elevated temperatures [154].

Laser science has reacted to thermal challenges with disks, rods or fibers, i.e., shapes optimized for heat removal [155–157]. In nonlinear optics, ultrathin crystals are in principle ideal [158], but efficient conversions generally require phase-matching and mm-long propagation. Here, we consider a line-shaped focus in a slab-like crystal. This geometry, featuring sideways heat removal, should in principle be as efficient as a disk or slab laser. For THz generation with femtosecond pulses, the interaction volume used in Cherenkov-type schemes [147, 159] should therefore be ideal for heat management at highest average power levels. This work aims at providing some first indications.

The experimental setup is depicted in Fig. 3.2. Pump pulses are obtained from a Yb:YAG thin-disk amplifier [153] (50 kHz repetition rate, central wavelength of  $\lambda = 1030$  nm and full-width-at-half-maximum intensity duration of  $\tau_{\text{FWHM}} \approx 1000$  fs). About 15 W of average power were available for this experiment, i.e. pulses with an energy of up to  $W = 300 \mu\text{J}$ . The  $y$ -polarized pump laser beam propagates along the  $z$ -axis. A two-lens cylindrical telescope and another cylindrical lens are used to magnify the beam in  $y$  direction and to focus it in  $x$  direction into a thin slab ( $1 \times 10 \times 10 \text{ mm}^3$ ) of stoichiometric MgO:LiNbO<sub>3</sub> with its  $c$ -axis oriented along the laser polarization. Optical rectification produces  $y$ -polarized THz radiation that is outcoupled [160] by an optically contacted Si prism. The angle of the Si prism ( $40.4^\circ$ ) corresponds to the half-apex angle of the Cherenkov wedge [161] and therefore provides close-to-normal incidence of the generated THz radiation onto the exit surface of the Si prism. The emitted THz beam (green) is collected by a  $90^\circ$  off-axis

parabolic mirror with 50.8 mm effective focal length and focused either to a pyroelectric power detector (Gentec-EO), beam profiler (Pyrocam-III, Spiricon Inc) or electro-optic sampling crystal (ZnTe, 1 mm). A 25-Hz chopper periodically blocks the incoming laser for lock-in detection in the power measurements. We also monitor the spectrum, beam profile and power of the pump pulses as transmitted through the LiNbO<sub>3</sub> slab.

To determine the optimum shape of the pump laser's line focus, we apply a simplified analysis based on Refs. [148, 147]. Neglecting losses and dispersion, the THz energy collected by a finite aperture with a collection half-angle  $\theta_{\text{lim}}$  can be written as

$$W_{\text{THz}} \propto W^2 z_{\text{slab}} \int_0^{\theta_{\text{lim}}} \frac{T(\theta) \cos \theta}{[\tau_{\text{eff}}^2 + w_y^2 \sin^2 \theta / c^2]^2} d\theta, \quad (3.2)$$

where  $z_{\text{slab}}$  is the length of the crystal,  $\theta$  is the (out-of-horizontal plane) angle of THz emission to air,  $T(\theta)$  is the Fresnel power transmission coefficient at the Si-air interface.

$$\tau_{\text{eff}}^2 = \tau^2 + w_x^2 (n_{\text{THz}}^2 - n_{\text{gr}}^2) / c^2 \quad (3.3)$$

is the effective duration of the THz pulse.  $\tau$ ,  $w_x$  and  $w_y$  are the  $1/e^2$  optical pulse duration ( $\tau = \tau_{\text{FWHM}} / \sqrt{2 \ln 2}$ ) and sizes of the optical beam in  $x$  and  $y$  directions, respectively.  $c$  is the speed of light, and  $n_{\text{THz}} = 5$  and  $n_{\text{gr}} = 2.2$  are the terahertz refractive index and the optical group refractive index of LiNbO<sub>3</sub>, respectively [147, 162]. The peak THz frequency is  $\nu_{\text{THz}} = 1 / (\pi \tau_{\text{eff}})$  [147]. For large  $w_y$  (at large enough single-pulse energy; see below), all divergences are small and the integrand in Eq. 3.2 tends to zero at  $\theta_{\text{lim}}$ . This allows to simplify Eq. 3.2 to

$$W_{\text{THz}} \propto W^2 \frac{z_{\text{slab}}}{w_y \tau_{\text{eff}}^3}. \quad (3.4)$$

Hence, for a given optical pulse energy, fixed  $w_y$  and  $z_{\text{slab}}$ , the THz energy is governed by  $\tau_{\text{eff}}$ , whose lower limit is set by the pump pulse duration  $\tau$ . Therefore, an optimum focus size in  $x$  direction is given by

$$w_x^{\text{opt}} \approx c\tau / (n_{\text{THz}}^2 - n_{\text{gr}}^2)^{1/2}. \quad (3.5)$$

Basically, a smaller focus would not significantly increase the THz yield, whereas a larger focus would restrict the output spectrum to lower frequencies [147]. The Rayleigh length  $z_{\text{R}}$  associated with  $w_x$  approximates the applicable size of the LiNbO<sub>3</sub> slab in  $z$  direction:

$$z_{\text{slab}}^{\text{opt}} \approx z_{\text{R}} = \pi w_x^2 n_{\text{ph}} / \lambda. \quad (3.6)$$

Here,  $n_{\text{ph}} = 2.15$  is the optical refractive index of LiNbO<sub>3</sub>. Reducing  $w_y$  results in linear scaling of THz energy according to Eq. 3.4, but the peak intensity should stay

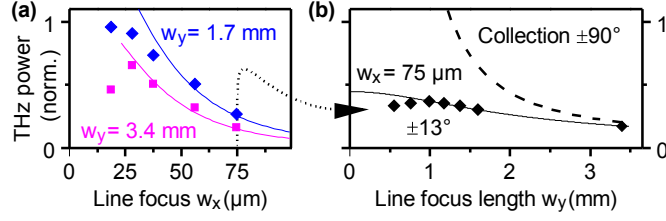


**Figure 3.3:** THz power depending on focus size in  $x$ - (a) and  $y$ - (b) dimension at 80  $\mu\text{J}$  pumping. Experimental data (diamonds, squares) is compared to the prediction given by Eq. 3.2 (solid lines). The dashed line corresponds to the case of  $\theta_{\text{lim}} = 90^\circ$ .

below saturation level,  $I_{\text{sat}} \approx 100\text{GW}/\text{cm}^2$  [161, 163]. We obtain

$$w_y^{\text{opt}} = \sqrt{8/\pi^3} W / (I_{\text{sat}} w_x^{\text{opt}} \tau). \quad (3.7)$$

Basically, a smaller focus would induce too strong saturation and a larger focus would reduce the efficiency.

For the available laser pulses, we obtain  $w_x^{\text{opt}} \approx 57 \mu\text{m}$ ,  $w_y^{\text{opt}} \approx 3.2\text{mm}$  and  $z_{\text{slab}}^{\text{opt}} \approx 21\text{mm}$ . This extreme aspect ratio ( $\sim 100$ ) makes the laser-excited volume basically a plane, ideal for heat removal. In the experiment, we had a  $10 \times 10\text{mm}$  LiNbO<sub>3</sub> crystal available, so  $z_{\text{slab}} = 10\text{mm}$ . From Eq. 3.3, we predict [147] a spectrum peaked at  $\nu_{\text{THz}} \approx 0.265\text{THz}$  for optimum focus sizes.

The THz beam is a quasi-plane wave perpendicular to the Si prism's tilted surface and efficiently emitted if divergences are smaller than the limit of total internal reflection at the Si-air interface,  $\sim 17^\circ$ . The effective source sizes in the experiment are approximately  $w_{\text{hor}}^{\text{THz}} \approx z_{\text{slab}} \cos(40.4^\circ)/2 \approx 3.8\text{mm}$  (rectangular shape) in the horizontal plane ( $x$ - $z$ ) and  $w_y^{\text{THz}} \approx w_y/\sqrt{2} \approx 2.4\text{mm}$  (Gaussian shape) in  $y$  direction. At 0.265 THz, the half-angle divergences in air are  $\theta_{\text{hor}} \approx c/(2\nu_{\text{THz}} w_{\text{hor}}^{\text{THz}}) \approx 8.5^\circ$  and  $\theta_y \approx c/(\pi\nu_{\text{THz}} w_y^{\text{THz}}) \approx 8.6^\circ$  for the predicted optimum geometry. Hence, losses by total internal reflection are negligible.

We experimentally validated the focus optimizations predicted by Eqs. 3.2-3.7 by applying 80- $\mu\text{J}$ , 50-kHz pump pulses and measuring the relative THz generation efficiency for varying focus sizes in both dimensions (Fig. 3.3). At fixed  $w_y$  (Fig. 3.3 a), a decreasing  $w_x$  leads to increasing THz output in accordance with Eq. 3.4 (solid lines). Only at smallest  $w_x$  there are some deviations due to the peak intensity exceeding  $I_{\text{sat}}$ . For a fixed  $w_x$  (Fig. 3.3 b), the agreement with Eq. 3.4 (dashed line) is given only at above  $w_y \approx 3\text{mm}$ . Below this value, the THz divergence in air exceeds the parabolic mirror's acceptance angle ( $\pm 13^\circ$ ). Equation 3.2 (solid line in Fig. 3.3 b) takes this into account, providing good agreement.

The consequences of suboptimal focusing become apparent by studying the dependencies of the THz output on the pump pulse energy for different focus sizes. Of

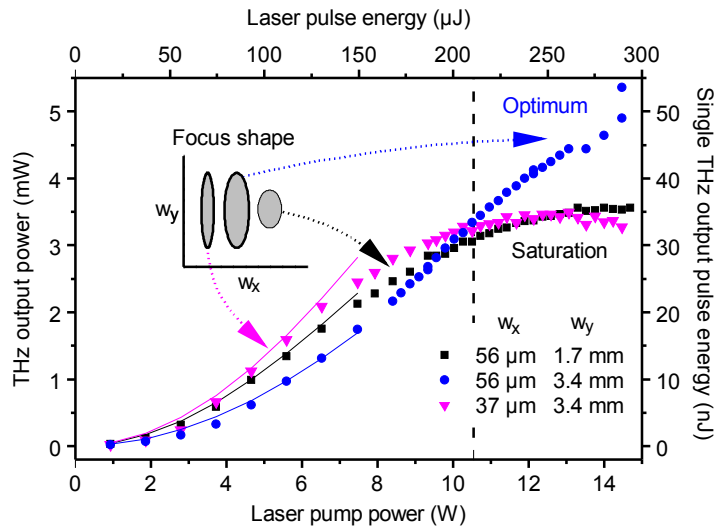


**Figure 3.4:** Emitted THz single-pulse energy for different focusing sizes. Pump power is given for the chopper-open intervals and THz energy for only the  $+x$  Cherenkov pulse (see text). Solid lines, quadratic dependence expected for low power.

the three traces shown in Fig. 3.4, one approximates the predicted optimum conditions (blue dots). The solid lines are plotted using Eqs. 3.2–3.4 and depict the quadratic dependences expected in the low-power regime. Tighter focusing in both directions (black, magenta) produces somewhat higher yields at low powers in accordance with Eqs. 3.2–3.4, but leads to earlier saturation.

We measured the electric field and spectrum for 200- $\mu$ J pump pulses at  $w_x = 56 \mu\text{m}$ ,  $w_y = 3.4 \text{ mm}$  by electro-optic sampling in a 1-mm-long ZnTe crystal. For derivation of the electric field from the electro-optic modulation, we follow Ref. [164], using an electro-optic coefficient of  $r_{14} = 3.8 \text{ pm/V}$  and taking into account the Fresnel reflection at the entrance surface of the ZnTe crystal ( $n = 2.78$ ) and the losses from the two surfaces of a Teflon lens ( $n = 1.43$ ) within the sampling setup. The relative modulation measured at the peak of the THz field was  $\Delta I/I_0 = 0.113$ , where  $\Delta I$  is the difference between the signals in the balanced detectors and  $I_0$  is their sum. Following Ref. [164], this corresponds to a THz electric field strength in air of  $\sim 5 \text{ kV/cm}$ ; the additional consideration of the phase mismatch in the detector crystal and finite probe pulse duration [165, 166] yields a peak value of  $\sim 7.2 \text{ kV/cm}$ . In the time domain, we find that the THz radiation consists of two single-cycle pulses: a first one emitted in the  $+x$  direction (Fig. 3.5 a) and a second one emitted in the  $-x$  direction and totally reflected. This pulse appears  $\sim 15 \text{ ps}$  later and has the opposite polarity. The measured spectrum of a single pulse (Fig. 3.5 b) peaks at 0.26 THz, as predicted. Figure 3.5 c depicts the THz beam waist profile; the shape is round and the full-width-at-half-maximum dimensions are 1.3 mm and 1.3 mm along

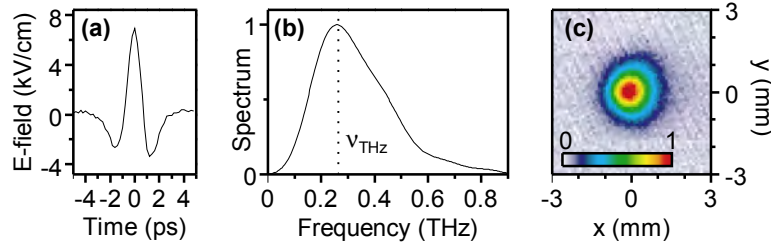


**Figure 3.5:** (a) THz electric field at 10 W pump power. (b) Spectrum; the dashed line marks the peak as predicted by theory. (c) THz beam profile at focus at 4 W pump power.

the 40.4° angled direction and  $y$ , respectively. This is close to the physical limit at 1.2 mm central wavelength, indicating good wave front quality. Assuming the same profile at full power, we estimate a peak field strength of  $\sim 30$  kV/cm at the focus.

With close-to-optimum focus sizes (blue traces in Fig. 3.4) and maximum available pump power (15 W), the maximum THz output is 5.3 mW at a conversion efficiency of  $4 \times 10^{-4}$ . The average THz power is by a factor of  $\sim 100$  higher than reported before with the slab geometry [149] and 3.3 times larger than the output achieved with a tilted-pulse geometry using the same laser [153].

The crucial advantage of this scheme, however, is an extremely efficient heat removal, as we will show in the following. Figure 3.6 shows a measurement of LiNbO<sub>3</sub>'s transmission coefficient in dependence on incoming pulse energy and focus conditions (compare Fig. 3.4). All transmitted radiation was collected (200–1200 nm). Figure 3.6 shows the results, revealing an intensity-dependent transmission decrease by up to 25%. We attribute this to an effective four-photon absorption process [150, 151], most likely a combination of the direct effect with sequential absorption via second harmonic generation or intermediate states including polarons [167, 168]. Similarly to Ref. [151], we neglect lower-order or higher-order absorption processes and approximate the optical intensity  $I$  to change with the distance  $z$  inside the crystal as

$$\frac{dI}{dz} = -\delta_{4\text{ph}} I^4, \quad (3.8)$$

where  $\delta_{4\text{ph}}$  is the four-photon absorption coefficient. The beam shape  $I(x, y)$  at each  $z$  was assumed constant via  $w_x$  and  $w_y$ , i.e., diffraction effects were neglected. The solid curves are the result with  $\delta_{4\text{ph}} = 30 \times 10^{-7} \text{ cm}^5/\text{GW}^3$ . The two curves at  $w_x = 56 \mu\text{m}$  fit the data well; some deviations for  $w_x = 37 \mu\text{m}$  at  $> 150 \mu\text{J}$  are attributed to aberrations in the experiment at such tight cylindrical focusing, or shortcomings of our simplified absorption model at tightest focus conditions. The inset shows the calculated (black line) and measured (diamonds) beam profile after the LiNbO<sub>3</sub> slab for  $w_x = 56 \mu\text{m}$ ,  $w_y = 1.7 \text{ mm}$  and 300  $\mu\text{J}$  pump energy. Reasonable agreement in both experiments indicates that an effective four-photon absorption

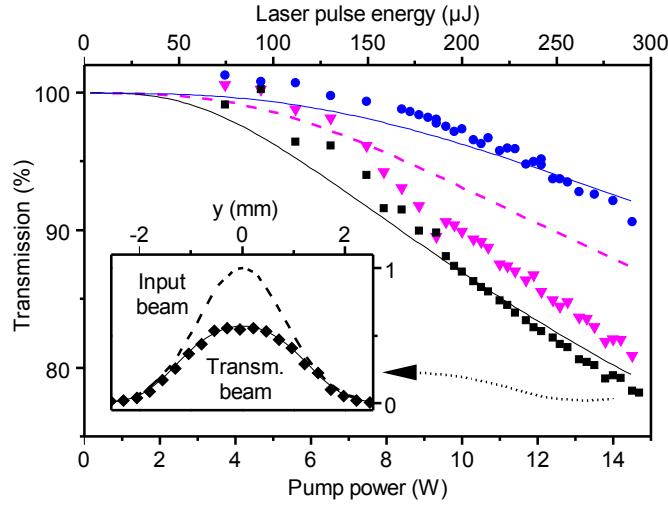


**Figure 3.6:** Optical power transmitted through the crystal for three different focus sizes (black, magenta, blue symbols according to Fig. 3.4) with a four-photon absorption fit (solid/dashed lines). Inset: Diamonds, measured beam profile (intensity) at the exit surface of the crystal; solid line, four-photon absorption fit; dashed curve, beam profile before the crystal (almost Gaussian).

coefficient seems appropriate for determining the order of magnitude of nonlinear absorption at our experimental conditions. We note that a 30 times lower  $\delta_{4ph}$  was roughly estimated before [151].

At optimum focus and maximum power (15 W in the chopper-open intervals or 7.5 W on average), about 10% is deposited within the LiNbO<sub>3</sub> crystal and heats it up (see Fig. 3.6). The pumped volume in our experiment is a very thin slab with an aspect ratio of  $\sim 60$  and 180 (comparing  $w_x$  to  $w_y$  and  $z_{slab}$ , respectively). We estimate the peak temperature in our experiment by assuming that  $P_{heat} = 1.5$  W (see blue trace in Fig. 3.6) are deposited in the chopper-open intervals in the area  $w_y z_{slab}$  ( $3.4 \times 10$  mm<sup>2</sup>). Assuming a Gaussian profile along  $w_y$  and a constant profile along  $z$  provides a peak heat density of  $\sqrt{2/\pi}/(w_y z_{slab}) \approx 3.5$  W/cm<sup>2</sup>. Since heat conduction along the extended dimensions  $y$  or  $z$  is negligible, a one-dimensional model with constant temperature gradient along  $x$  predicts the peak temperature increase:

$$\Delta T_{peak} \approx \frac{\sqrt{2/\pi} P_{heat} D_{sink}}{w_y z_{slab} k_{LN}}, \quad (3.9)$$

where  $k_{LN} \approx 5$  W m<sup>-1</sup> K<sup>-1</sup> [169] is LiNbO<sub>3</sub>'s thermal conductivity;  $D_{sink} \approx 1$  mm denotes the distance between the excitation plane and the crystal's back surface. The crystal is in this approximation assumed in good contact with a heat sink. We obtain  $\Delta T \approx 8$  K for 15 W of pump power. This low value is a direct consequence of the line-like pump focus with high aspect ratio.

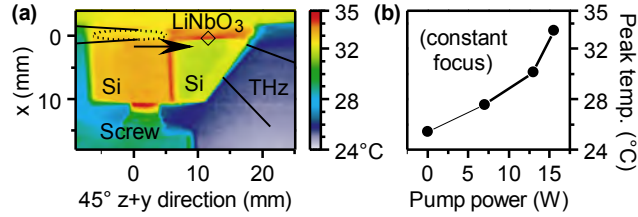


**Figure 3.7:** Heat deposition in LiNbO<sub>3</sub>. (a) Thermal image of the generating LiNbO<sub>3</sub>/Si structure, viewed from above at an angle of 45°. The dashed line indicates the optical focus shape. The temperature within LiNbO<sub>3</sub> slab is evaluated at the diamond-marked position assuming an emissivity of 0.95. (b) Peak temperature for increasing pump power (chopper-open intervals) at constant, optimum focus dimensions (3.4 mm × 56 μm). The rather low temperatures are caused by the disk-like heat removal toward the metal mount (top).

In the experiment, the crystal was mechanically pressed onto an anodized aluminum mount with no particular adhesion layer. Figure 3.7 a shows a thermal camera image (SC305, FLIR Systems GmbH) taken at 7–13 μm wavelength and from 45° from top for 300-μJ pump pulses. The thermal camera was focused approximately to the center of the crystal in order to measure the peak temperature inside, at an estimated accuracy of ~ 1 K. Figure 3.7 b shows the measured peak temperature (diamond) for different input powers, providing an approximate indication of the peak temperature inside the crystal. We note that in this experiment the average power and pulse energy were reduced at constant repetition rate and therefore in proportion; the measured temperature is therefore nonlinearly increasing with power. Interesting is the last data point at ~ 15 W: although ~ 10 % of the applied power is deposited via four-photon absorption, the LiNbO<sub>3</sub> slab heats up by less than 10 K, which is the same order of magnitude as predicted via Eq. 3.9. This agreement indicates that heat removal in a disk-like geometry is indeed efficient. We note that the experimental  $D_{\text{sink}}$  of 1 mm is much larger than necessary; it could in principle be reduced down to 2–3 times  $w_x$  while maintaining proper beam propagation. According to the model, this would reduce the peak temperature further by a factor of about 5–10.

We have now enough information for predicting the general scaling behavior of temperature and conversion when going to much higher average power levels. An increase of repetition rate causes a proportional increase of temperature. A factor of ten seems tolerable, and the scheme therefore offers efficient THz conversion at up to hundreds of kHz repetition rate. Intriguingly, at constant repetition rate, an increase of pump pulse energy predictably causes neither efficiency decrease nor temperature increase. Basically,  $w_x^{\text{opt}}$  depends only on pulse duration and is constant (Eq. 3.5); therefore,  $z_{\text{slab}}^{\text{opt}}$  is also constant (Eq. 3.6). The spot width  $w_y^{\text{opt}}$  increases in proportion to the pulse energy (Eq. 3.7), and the peak intensity stays constant.

Therefore, the deposited power via four-photon absorption is also constant per area, and the peak temperature stays essentially unchanged (Eq. 3.9). For example, ten times higher pulse energy and repetition rate than in the experiment, i.e., 3 mJ at 500 kHz (1.5 kW), would give  $w_x^{\text{opt}} \approx 57 \mu\text{m}$ ,  $w_y^{\text{opt}} \approx 3.2 \text{ cm}$ ,  $z_{\text{slab}}^{\text{opt}} \approx 21 \text{ mm}$  and  $\Delta T_{\text{peak}} \approx 80 \text{ K}$ , which seems quite acceptable. This promising scaling law is a direct consequence of the line focus with high aspect ratio.

In summary, high-energy THz generation in  $\text{LiNbO}_3$  with a slab geometry is roughly as efficient as with tilted pulses in a prism [153], but offers reduced experimental complexity and minimizes thermal load in a scalable way. Shaping the focus aspect ratio appears to be a promising concept for reducing thermal effects [170–172] in other nonlinear optical conversions as well. This concept should be generally applicable in nonlinear optics whenever the pulse energies are large enough for shaping the focus aspect ratio at constant intensity without losing on Rayleigh length, hence in most modern femtosecond laser applications.

## Acknowledgments

We acknowledge funding from the European Research Council and the Munich-Centre of Advanced Photonics. M.V.T. acknowledges support under the agreement 02.B.49.21.0003 between Ministry of Science and Education of Russia and University of Nizhny Novgorod and by RFBR Grant 15-02-08328.



# All-optical control and metrology of electron pulses

Previously, we had laid out the theoretical requirements for electron pulse compression (Chapter 2) and demonstrated a straightforward way of optically generating single cycle terahertz pulses (Chapter 3). In the present chapter the first-time application of terahertz transients for compression and temporal characterization of electron pulses is described.

## 4.1 Preface

Ultrafast electron imaging schemes rely on short electron pulses to capture the finest atomic dynamics in a specimen. While the generation of electron pulses by optical means, i.e., using the photoelectric effect, is comparably simple, keeping an electron pulse of finite energy bandwidth short is rather difficult due to intrinsic dispersion effects (see Chapter 2). In Chapter 2 we also learned that despite these effects, it is nevertheless possible to form very short pulses at a specific point in space (the temporal focus) by virtue of so-called temporal lenses.

A temporal lens usually relies on the time-varying momentum transfer from an electromagnetic wave to an electron pulse. In free space, however, electron momentum manipulation is not possible using linearly polarized, electromagnetic plane waves [68], which are a good approximation for our optically generated terahertz transients (Chapter 3). Imposing boundary conditions as to allow for efficient particle velocity modulation is therefore crucial. Resonantly driven microwave cavities are a conventional choice to achieve the desired electron velocity modulation [63, 62], but these devices are restricted with respect to acceleration gradients and laser synchronization [66, 67]. Over the course of the past decades, these limitations have inspired

the invention of various laser-driven momentum transfer schemes, which, for example, make use of ponderomotive effects [70, 71], localized optical near-fields [77, 78] and dielectric or metallic interfaces [73, 82, 100]. But the high modulation frequencies ( $> 100$  THz) of direct laser driven concepts prevent longitudinally uniform pulse manipulation. Such a pulse manipulation is however possible with fields of frequencies smaller than 1 THz, because the pulse “fits” within one half-cycle of the modulating field. As it has been shown in Chapter 3, such fields with field strengths above  $10^5$  V/m can be generated in an all-optical fashion, which ensures passive laser-synchronicity.

In this chapter, the first-time realization of electron pulse compression with optically generated terahertz fields is demonstrated. The use of a bow-tie shaped terahertz resonator (see inset of Fig. 4.1) excited by our single-cycle terahertz transients allows efficient electron momentum modulation of the entire pulse within less than one half-cycle. As the electrons swiftly pass through the near fields inside the tilted resonator (see Fig. 4.1), they pick up momentum depending on the phase of the electric field inside the resonator. This concept allows to reduce the FWHM electron pulse duration by more than an order of magnitude down to 75 fs (Fig. 4.3).

High-resolution temporal characterization of these electron pulses is achieved using another terahertz driven bow-tie resonator that basically acts as an ultrafast oscilloscope. A particle that is incident perpendicular to the resonator plane gets deflected as a function of its arrival time. An electron pulse of finite duration is therefore smeared out on the detector (see Fig. 4.2 A). From the width of this streak, the temporal electron pulse shape can be reconstructed (see Appendix B and Fig. 4.3 C). This streaking methodology is central to all following experiments described in Chapters 5–7. It features few-femtosecond temporal resolution and inherent synchronicity to the optically generated electron pulses (see Fig. 4.4). Since the first demonstration in the original article [89], that this chapter is based on, the streaking concept has been picked up and implemented for terahertz-based temporal characterization of electron pulses of up to relativistic energies [95, 97, 98].

A precursor experiment on electron deflection from an electron-transmitting thin foil irradiated with terahertz pulses is also contained in this chapter’s underlying article (see Fig. 4.5).<sup>1</sup> Even though this concept’s inherently complex angular dependencies were not yet completely unveiled at this point, the results demonstrate the possibility of a resonator-free momentum transfer scheme. In this way, the experiment largely influenced and inspired this thesis’ progress. The later obtained theoretical and experimental insights (see [173] and Chapter 6) led to the develop-

---

<sup>1</sup>The results of this experiment, conducted by Waldemar Schneider and Andrey Ryabov, have not been obtained in the course of this thesis.

ment of advanced electron pulse control schemes and culminated in the generation of the shortest terahertz-compressed electron pulses reported to date (see Chapter 7).

The realization of terahertz-based electron pulse compression and characterization is a central result of this thesis. It has been achieved in cooperation with Catherine Kealhofer and with assistance from Andrey Ryabov. To this end, the existing electron beamline [174] was upgraded to allow electron pulses to intersect with the terahertz beams at the resonator structures. This upgrade required a dedicated redesign of the experimental setup that was performed in the course of this thesis and which enabled its unprecedented temporal stability (Fig. 4.4). Furthermore, the electron pulse streaking technique developed here is also used in all of the later reported electron pulse compression experiments in this thesis. Measurement and evaluation routines, such as reconstruction of the temporal electron pulse profiles from streaking data (see Appendix B) and data visualization via deflectograms (Fig. 4.3 A and B), originate from this work. The detailed study of electron pulse compression characteristics (Fig. 4.3 C and D) and the physics of optical to electron momentum transfer, later led to a significant improvement in compressed electron pulse duration (Chapter 7) and novel techniques for electron pulse shaping and characterization (Chapters 5 and 6). The details of the present study have first been published in *Science* (Vol. 352, pp. 429–433) in 2016.<sup>2</sup> The following text (pp. 61–72) is the author’s version version of the article published in [89]. The supplementary material to this article is given in Appendix B.

---

<sup>2</sup>Author contributions: Experiments on electron pulse compression and streaking with bow tie resonators (Figs. 4.2–4.4) have been set up and conducted by CK and DE together with AR. Evaluation by CK, DE, AR and PB. Simulations of compressed electron beam profiles (Fig. 4.3 C and D) by CK. Design of bow tie resonators by AR. Realization and analysis of experiments on electron pulse deflection at a thin metallic foil (Fig. 4.5) by WS and AR. Experimental concept and supervision by PB and FK. All authors discussed and interpreted the results and contributed to the writing of the manuscript.



# All-optical control and metrology of electron pulses\*

Catherine Kealhofer, Waldemar Schneider, Dominik Ehberger, Andrey Ryabov, Ferenc Krausz and Peter Baum

## Abstract

Short electron pulses are central to time-resolved atomic-scale diffraction and electron microscopy, streak cameras, and free-electron lasers. We demonstrate phase-space control and characterization of 5-picometer electron pulses using few-cycle terahertz radiation, extending concepts of microwave electron pulse compression and streaking to terahertz frequencies. Optical-field control of electron pulses provides synchronism to laser pulses and offers a temporal resolution that is ultimately limited by the rise-time of the optical fields applied. We use few-cycle waveforms carried at 0.3 THz to compress electron pulses by a factor of 12 with a timing stability of  $< 4$  femtoseconds (rms) and measure them by field-induced beam deflection (streaking). Scaling the concept towards multi-THz control fields holds promise for approaching the electronic time scale in time-resolved electron diffraction and microscopy.

[doi:10.1126/science.aae0003](https://doi.org/10.1126/science.aae0003)

Electron beams controlled with temporally varying electric fields enabled the first oscilloscopes and electronic computers; today, they are essential to free-electron lasers [46, 175], ultrafast streak cameras [135–137] and femtosecond imaging and diffraction techniques [176, 32, 177]. Microwave technology at GHz frequencies has been the workhorse for ultrafast electron pulse control thus far, with applications ranging from particle acceleration to ultrafast pulse compression and high-resolution streak cameras. Unfortunately, microwave components suffer from appreciable phase drifts, and laser-microwave synchronization below 10 fs becomes technologically challenging [66, 178, 179]. Laser field-driven dielectric accelerator structures operating near petahertz frequencies are being developed for next-generation particle accelerators [75, 120], but the short wavelength ( $\sim 1 \mu\text{m}$ ) and oscillation period ( $\sim 1$  fs) place

---

\*This is the author's version of the work. It is posted here by permission of the AAAS for personal use, not for redistribution. The definitive version was published in [89] [doi:10.1126/science.aae0003](https://doi.org/10.1126/science.aae0003).

extreme requirements on the input beam emittance and pulse duration [75, 120]. In between, there is the regime of THz frequencies. Femtosecond-laser-generated plasma waves exhibit THz longitudinal fields, which can accelerate electrons efficiently to the relativistic and ultrarelativistic energy domain [180]. However, the excessive energy, divergence and insufficient timing control of the resultant several-to-multi-MeV electron pulses impair their utility for most of the above applications and particularly for ultrafast electron diffraction and microscopy.

Pulsed THz fields can be generated in a much more controlled way from the coherent nonlinear polarization of matter, e.g., by optical rectification [88]. The pulses can reach field strengths on the order of  $10^{10}$  V/m [141], and their half-cycle durations ideally match practical electron bunch dimensions (fs-ps in time and  $\mu\text{m}$ -mm in diameter). In addition, THz control fields derived from a single ultrafast laser via nonlinear optics result in near-perfect (potentially sub-femtosecond) temporal synchronization, offering the potential to substantially surpass the performance of microwave-laser synchronization and obviating the need for locking electronics. Therefore, THz and infrared radiation generated from laser-driven coherent nonlinear polarization is ideally suited for controlling electron pulses, as indicated by simulations [56, 91–94] and recent experiments on controlling nanoscale photoemission [181] and electron acceleration in a dielectric waveguide [90].

#### 4.2.1 Concept and implementation

Figure 4.1 depicts the experimental implementation of our THz-field-controlled electron beamline consisting of two functional units, one for pulse compression and one for temporal characterization by streaking [182, Appendix B]. Near-1-ps pulses from a Yb:YAG-based regenerative amplifier [153] drive two optical rectification stages for generating few-cycle THz pulses. With the same laser, electron pulses with on average  $\sim 1$  electron per pulse are generated by two-photon photoemission from a gold thin-film photocathode and electrostatically accelerated to 70 keV. The optical rectification stages produce near-single-cycle pulses at a carrier frequency of 0.3 THz with pulse energies up to 40 nJ, implying field strengths of up to  $\sim 10^6$  V/m under gentle focusing conditions. These are used to control the electron pulse’s momentum, energy, duration or timing.

We use butterfly-shaped metal resonators (inset to Fig. 4.1) to mediate the interaction between the electrons and the terahertz fields. The THz electric field is enhanced in the plane of the resonators and confined to sub-wavelength dimensions so that energy and momentum conservation in the electron-photon interaction can be satisfied [183].

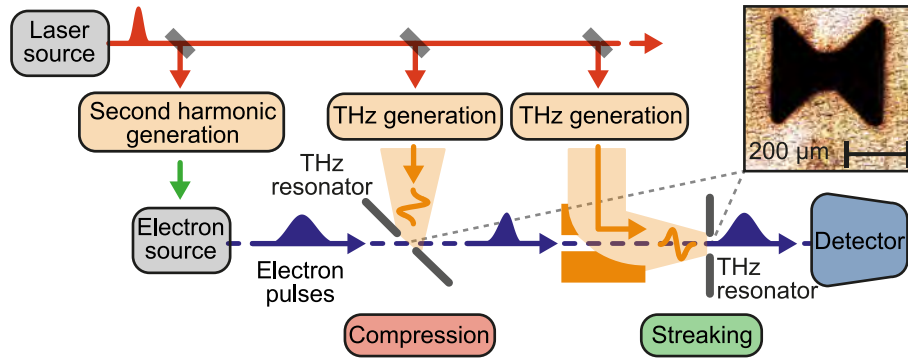


**Figure 4.1:** Experimental setup. A 1-ps laser pulse from a Yb:YAG regenerative amplifier is frequency-doubled and generates electron pulses from a thin-film gold photocathode. The laser also drives two optical-rectification stages, each generating single-cycle THz pulses with energy of up to 40 nJ. THz resonator structures are laser-machined in a 30- $\mu\text{m}$ -thick aluminum foil (inset). A first element, used for compression, is oriented at  $45^\circ$  to the electron beam, providing time-dependent longitudinal forces on the electrons. The second THz control stage, used for streaking, is oriented normal to the beam, resulting in time-dependent transverse deflection.

Electrons passing through the resonator structures experience a net change in momentum that corresponds to the integral of the Lorentz force along their trajectories. This change varies periodically as a function of arrival time of the electron in the THz field. The first THz control stage uses a tilted resonator to provide force components longitudinal to the electron beam for temporal compression. The second THz control stage, oriented normal to the beam, provides a delay-dependent deflection for temporal characterization.

The root-mean-square (rms) electron beam radius is  $3\ \mu\text{m}$  at the compression resonator and  $11\ \mu\text{m}$  at the streaking resonator, at least 8 times smaller than the resonator mode dimensions. Because the electron pulse from the source is shorter than 1 ps and hence shorter than the half cycle of the THz field, the latter exerts a uniform but time-dependent force on the electron wavepacket in all dimensions. This force imparts acceleration and/or compression at the first stage and time-dependent deflection (i.e., streaking) at the second stage. As a result, the pulsed electron beam is entirely under control of a single intense-pulse laser system and its optical fields.

### 4.2.2 Electron pulse compression

Even without any space charge, electron pulses unavoidably have a finite duration after acceleration due to dispersion [57]. Electron pulse compression is therefore indispensable for reaching sub-phonon or electronic timescales in diffraction [64]. Electron pulse compression requires deceleration and acceleration of the electron when arriving before or after the mean electron arrival time, respectively. For pulse

compression with THz fields, the first butterfly microstructure is oriented at an angle of  $45^\circ$  with respect to the electron beam. THz pulses are incident at an angle of  $45^\circ$  at the metal surface and hence normal to the electron beam (Fig. 4.1), so that the THz-excited resonance provides time-dependent force components parallel to the electron beam. In analogy to microwave compression, the time-dependent fields permit compression of the electron pulse substantially below its initial duration [64] and hence down to attosecond duration in the absence of space charge [57]. Note that in the limit of one- or few-electron pulses, the pulse duration is understood as the ensemble distribution of electron arrival times with respect to the laser reference.

The effective strength of the compression stage is quantified by  $g_E$ , the energy imparted to the electrons in the forward direction with changing delay time. In the experiment,  $g_E$  is proportional to the incoming THz peak field strength divided by the cycle period. After the interaction, the electron pulse becomes shorter as it propagates, reaching a minimum duration at a distance

$$f_c = m_e (\gamma\beta c)^3 / g_E \quad (4.1)$$

where  $c$  is the speed of light,  $m_e$  is the mass of the electron,  $\beta$  is the ratio of the electron speed to the speed of light, and  $\gamma = 1/\sqrt{1-\beta^2}$ . Localized THz fields enhanced to merely  $10^6$  V/m are sufficient to yield a  $g_E$  of 50 eV/ps and hence produce a convenient temporal focus at a distance of tens of centimeters from the compression stage, depending on central energy [182, Appendix B].

### 4.2.3 Temporal characterization

To measure the temporal profile of the electron pulse, the second stage is configured to provide a terahertz-driven delay-dependent deflection, which we dub streaking, in analogy to microwave-driven and laser-field-driven devices. We first tested the temporal characterization with the uncompressed pulse. The time-dependent deflection of the beam yields a deflectogram (Fig. 4.2 B), i.e. the beam profile (in the plane of deflection) plotted vs. delay of the electron pulse with respect to the THz field. At the zero crossings of the field, the deflection is a steep function of time, and the beam width increases due to the finite-duration electron pulse. Raw images of the electron beam were recorded on the phosphor-covered camera with the THz deflecting field switched on and off and timed to yield maximum streaking of the beam (Fig. 4.2 A). At the maxima and minima, minimal spreading occurs. The electron pulse duration and the time-dependent optical forces are determined by fitting the data of Fig. 4.2 B assuming an instantaneous momentum transfer transverse to the electron beam induced by the THz field as a function of the electron arrival time.

The deflection is proportional to the integral of the Lorentz force along the electron's trajectory and closely follows the electric field's temporal profile inside the slit

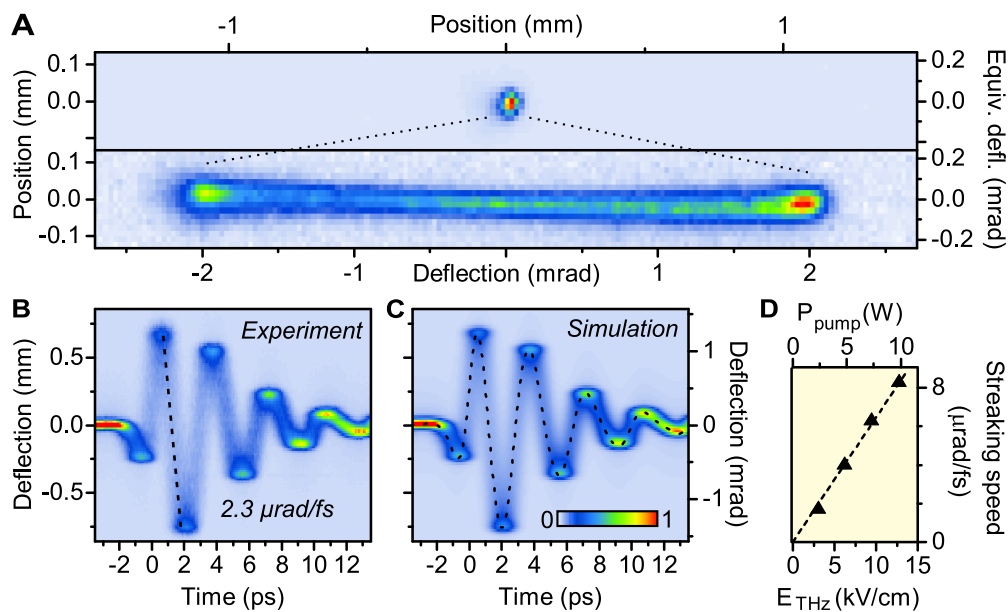


**Figure 4.2:** All-optical THz streak camera. **(A)** Images of the electron beam on the camera with and without the THz field. The full width at half maximum of the streaked beam is  $\sim 50$  times larger than that of the un-streaked spot. **(B)** Time-dependent deflection (deflectogram) measured by varying the delay between the electron pulse and the streaking THz. Images of the beam are integrated along the un-streaked direction to determine a one-dimensional profile at each time-delay. **(C)** Simulated deflectogram, result of a fit simultaneously characterizing the electron pulse duration and the streaking field, dotted line. The fitted electron pulse duration is 930 fs. **(D)** Streaking speed vs. input THz field strength; the linear relationship supports a direct, field-driven interaction.

due to near field confinement, as a consequence of the electron traversing the field-enhanced region within a tiny fraction of the field oscillation period. This is in sharp contrast with attosecond streaking, which operates in the opposite limit (transit time much longer than the streaking field duration) so that the streaking spectrogram mimics the vector potential of the streaking field [184]. A spline interpolation through four support points per picosecond is used for modelling time-dependent deflection, and a Gaussian temporal profile is assumed for the electron pulse. Figure 4.2 C shows the calculated deflectogram with the fitted time-dependent deflection. The electron pulse duration is 930 fs full width at half maximum (FWHM), consistent with a propagation-induced temporal spread resulting from a 0.6-eV initial energy spread of the electron pulse.

The deflectogram displays sustained deflection oscillations far beyond the duration of the near-single-cycle incident THz driving pulse. The best fit yields a resonance frequency of  $0.29 \pm 0.01$  THz of the resonator with a decay rate of  $4.5 \pm 0.4$  ps resulting from radiative and resistive damping.

Figure 4.2 D shows the resultant maximum streaking speed as a function of incident peak THz field strength in this range. The highest value measured exceeds  $8 \mu\text{rad}/\text{fs}$ , corresponding to a streaking speed of  $4.4 \mu\text{m}/\text{fs}$  at the camera in our experimental geometry. The distance over which all momentum change accumulates is determined by the THz near-field decay length ( $\sim 100 \mu\text{m}$ ) and the foil thickness ( $\sim 30 \mu\text{m}$ ). The resulting interaction length is some 100 times smaller than in conventional streak cameras [135, 136], removing a significant limitation of their temporal resolution.

In the THz field-driven streak camera, temporal resolution is dictated by the beam quality and signal-to-noise ratio. At an incident THz field strength of  $1.3 \times 10^6$  V/m, the root mean square (rms) beam width on the camera of 1.6 pixels ( $25 \mu\text{m}$ ) corresponds to 6-fs resolution (rms). With  $\sim 1000$  detected electrons, the beam quality and signal-to-noise allow detection of displacements or spot width changes of 0.1 pixels ( $1.56 \mu\text{m}$ ). A displacement of 0.1 pixels corresponds to 0.4 fs accuracy of arrival time measurements, whereas a 0.1-pixel increase of the spot size from the unstreaked value corresponds to a 2 fs (rms) or  $\sim 4.5$ -fs (FWHM) pulse duration. These resolutions are achieved with a signal accumulation time of 6 s and improve with longer integration. These values represent a near-two-order-of-magnitude improvement over the state-of-the-art of microwave streak cameras [135, 136], obtained already at THz fields of  $\sim 10^6$  V/m as opposed to  $10^{10}$  V/m available [141]. As a consequence, our THz streaking concept may allow the direct measurement of sub-femtosecond electron pulses [59, 78] and their timing drifts.

#### 4.2.4 Compression and measurement

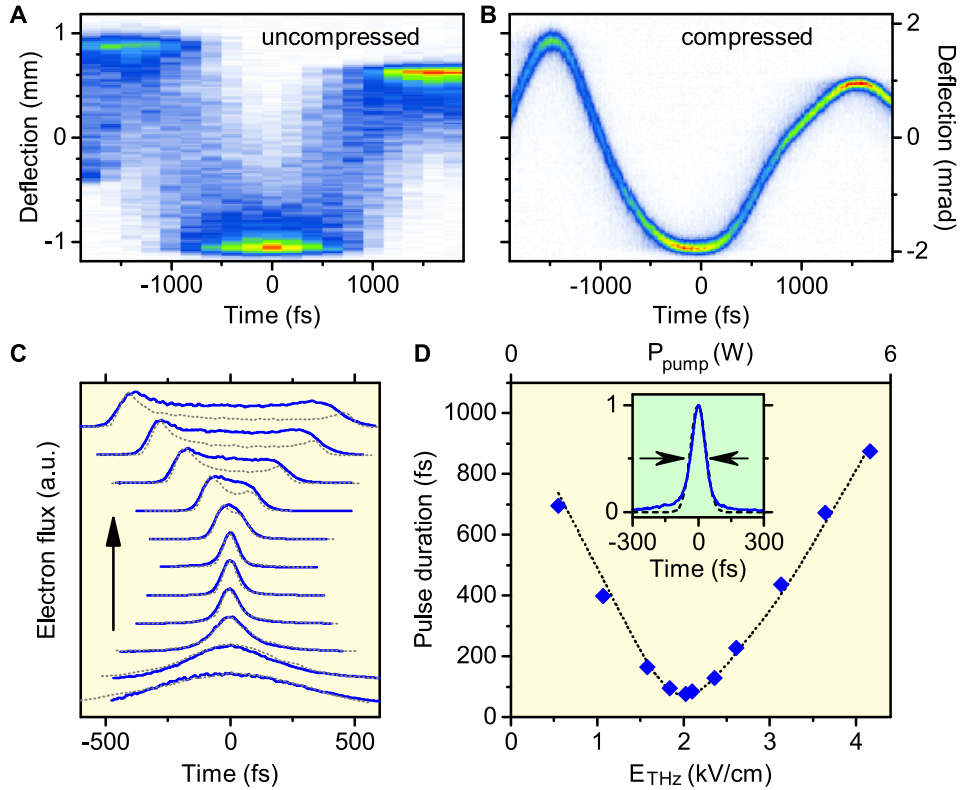
Figure 4.3 A and 4.3 B show streaking deflectograms with and without THz field compression, respectively. In the latter, the THz field strength of the compression stage has been adjusted to produce a temporal focus at the streaking stage. A pronounced sharpening of the trace can be seen in the vertical (streaking) direction, indicating a substantial reduction in electron pulse duration.

Figure 4.3 C shows the systematic evolution of measured electron temporal profile for a varying compression strength  $g_E$  [185]. The deflection as a function of time is reconstructed and used to perform the nonlinear transformation between the spatial profile of the streaked pulse and the underlying temporal profile of the THz-field-manipulated incident pulse [182, Appendix B]. The dotted lines depict the results of three-dimensional electron trajectory simulations [185].

The electron pulse (blue) first shortens to a minimum duration (5th trace) and afterwards lengthens again, with a double-peaked shape that is characteristic of over-compression by a sinusoidal field [59]. Figure 4.3 D shows the experimental and theoretical pulse durations versus THz-field strength and average power of the driving laser. The shortest pulse (inset to Fig. 4.3 D) has a FWHM duration of 75 fs, in excellent agreement with the simulation and a factor of 12 shorter than the original, 930-fs pulses and shorter than the half period of many fundamental phonon modes and molecular vibrations. Comparison of the shortest measured pulse shape with a Gaussian profile (dotted line) reveals a deviation; this is a consequence of the THz field's residual curvature over the time scale of the incoming, uncompressed electron pulse. Optimized electron sources with sub-100-fs duration [106] will reduce this effect; the particle-tracing simulations [182, Appendix B] show that 3-fs (FWHM) compressed pulses can be generated with a smaller source size and the 100-fs incoming pulses achievable if the photoemission energy is matched to the work function [32, 57]. This would be an order of magnitude shorter than the 28-fs (FWHM) pulses generated in the single-electron regime so far [64] and allow the study of light-driven electronic motion via sub-cycle diffraction [28, 48].

#### 4.2.5 Electron-laser timing metrology

Femtosecond pump-probe crystallography with electrons [32] or with x-ray free-electron lasers [46, 175] suffers from laser-electron timing jitter at the sample location, typically caused by imperfect laser-microwave synchronization [178, 179]. In contrast to the statistical electronic processes in the photodiodes used for microwave synchronization [66], laser-generated THz fields are, within the attosecond response time of the underlying nonlinear polarization, perfectly locked in time to the intensity profile of the pump pulses. Timing jitter/drift between the laser pump pulse and the



**Figure 4.3:** THz-driven electron pulse compression. Comparison of deflectograms for (A) uncompressed (930 fs) and (B) compressed (75 fs) pulses at time-steps of 200 fs and 10 fs, respectively. The deflectograms were measured sequentially and have a temporal resolution of  $\sim 9$  fs (rms). (C) Measured temporal profiles of the electron pulses (blue traces) as the compression strength is increased (black arrow), taking into account for long pulses the curvature of the time-dependent deflection. Simulated temporal profiles ( $10^4$  particle trajectories) [182, Appendix B] are superimposed (dotted black lines). Differences between the measured and simulated pulses are due in part to the curvature of the streaking field, which reduces the streaking time-resolution at times far from zero. (D) Electron pulse duration (FWHM) vs. incident THz field strength. The measured values are plotted as blue diamonds, and the simulation is shown as a dotted black line. The inset shows the shortest measured pulse profile (5th trace from the bottom of part (C)).

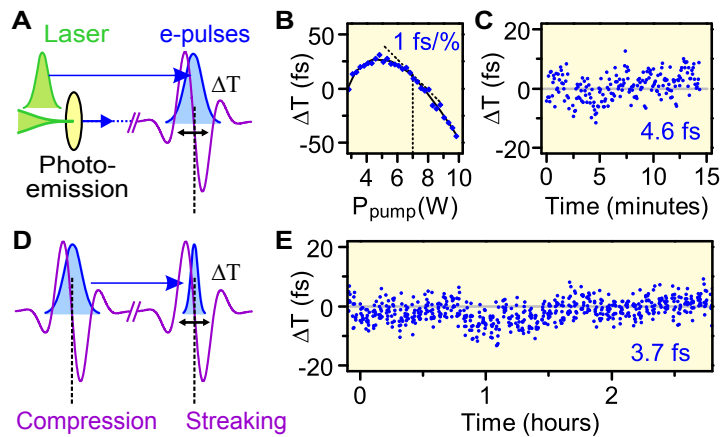


**Figure 4.4:** Passive few-femtosecond synchronization. **(A)** Concept for measuring arrival-time drifts between the uncompressed electron pulses and the optical streaking field. **(B)** Systematic coupling of laser fluctuations to timing drifts. Measuring shifts in the THz zero-crossing time with increasing laser pump power reveals a slope of less than 1 fs per 1 % change in laser power in a wide range of operation conditions. **(C)** Measured timing drift between photoemitted electron pulses and the THz field cycles at 10-s intervals. The integration time for each data point is 1 s. **(D)** Concept for measuring the arrival-time drift between THz-compressed electron pulses and the streaking field cycles. **(E)** Result with 6-s integration times reveals passive longer-term synchronization. The jitter values in **(C)** and **(E)** are rms deviations; statistical errors are 3.5 fs and 2.7 fs, respectively.

electron probe pulse can only originate from extrinsic effects, such as fluctuations in path lengths or laser pulse energy.

Experimentally, we studied drifts of the electron pulse with respect to the THz field by setting the near-field-enhanced streak camera to a constant delay and recording the beam deflection over time (Fig. 4.4 A). First, we scrutinized a possible role of amplitude-to-timing conversion in the nonlinear optical rectification process. Figure 4.4 B shows the change in electron–THz-field timing when varying the laser pump pulse intensity before the THz generation crystal. We observe a systematic change in timing, but the slope at the operation conditions (7 W) is only 1.0 fs per one percent change in laser power, which is negligible for our laser system, whose intensity drifts and shot-to-shot energy fluctuations are below 2 % [153].

In a second experiment, we measured drifts of the photoemission electrons with respect to the streaking THz field by turning the THz control field off. For periods longer than 1 s we obtain 4.6 fs (rms) over 15 min (Fig. 4.4 C). Finally, we repeated this measurement with the THz-driven pulse compression activated, with integration times of 6 s and after  $\sim 2$  h of laboratory thermalization, measuring 3.7 fs rms over three hours (Fig. 4.4 E). This vastly outperforms the long-term stability of state-of-

the-art laser-microwave synchronization with feedback loops [32] and also compares favorably to the record value (5 fs rms) achieved with direct microwave extraction from a laser pulse train and data post-processing [66]. We expect that the measured, residual 3.7-fs drift could be further decreased by minimizing the (currently meter-scale) optical path lengths and/or stabilizing them interferometrically. We note that synchronization in the all-optical scheme is entirely single-pulse-based and therefore few-femtosecond stability can be maintained at any—and especially at very low—laser repetition rate. A clock or master oscillator is not required.

#### 4.2.6 Direct THz-electron interaction at a foil: a THz cathode-ray-tube oscilloscope

Enhancement of the THz field by a microstructure resonator has proven highly beneficial for electron pulse control and metrology, but some experiments might require more direct control, avoiding the localization and limited spectral response inextricably linked to resonators. For a direct electron-THz interaction, we realized a resonator-free interaction geometry based on a symmetry-breaking surface [82, 81]. In the depicted concept (Fig. 4.5 A), a thin metal foil (70-nm aluminum) acts as a mirror for THz radiation, and electrons transmitted through it experience an abrupt extinction of the electromagnetic field, leading to net deflection. The combination of angles is chosen such that extended beam profiles experience a homogeneous time dependence owing to lateral phase matching [82].

Fig. 4.5 C and 4.5 D depict measured and calculated streaking deflectograms of an uncompressed electron pulse at an energy of 90 keV, exhibiting excellent agreement. Although the peak deflection is smaller than for the resonator-based setting, the deflectogram clearly exhibits single-cycle behavior, preserving the incident THz pulse’s ultrabroadband spectrum without alteration [153]. Fig. 4.5 B shows the peak-to-peak deflection as a function of the incoming THz field strength, revealing the expected linear dependence. Electrons delivered in a nearly collimated beam are directly (and spatially uniformly) deflected directly with the field cycles, advancing the century-old cathode-ray-tube oscilloscope to the terahertz domain. Owing to the 1-fs-scale timing accuracy of the sampling electron pulse, the cut-off frequency of this THz cathode-ray oscilloscope is dictated by the inverse electron pulse duration,  $> 10$  THz with the demonstrated compressed pulses,  $> 100$  THz with the few-fs electron pulses predicted by the simulations, and  $> \text{PHz}$  with the isolated attosecond electron pulses feasible with multi-stage compression (see below).

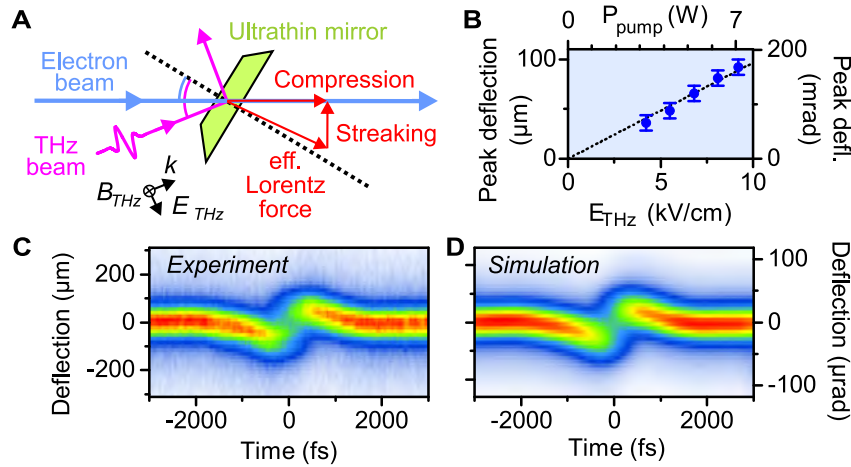


**Figure 4.5:** Resonance-free single-cycle streaking. **(A)** Resonator-free concept for mediating the electron-THz interaction using an ultrathin THz mirror. The angles of the THz beam and the foil are chosen for lateral phase matching across arbitrarily large electron and THz beam profiles. **(B)** Measurement of peak deflection vs. incident THz field strength. **(C)** Experimental deflectogram revealing single-cycle behavior. **(D)** Simulated deflectogram with an electron pulse duration of 800 fs.

### 4.2.7 Conclusions and outlook

Our demonstrated generic and scalable all-optical methodology for the control and characterization of ultrafast electron pulses used laser-generated sub-cycle THz transients for twelve-fold electron pulse compression, followed by a temporal profile characterization with a 10-fs resolution. Electron-transparent foils mediating the electron-field interaction permit time-energy phase-space manipulation of collimated electron beams of any size and, conversely, the temporal characterization of optical field transients up to frequencies only limited by the electron pulse duration, which – as opposed to the photon pulse in electro-optical sampling – may be shortened to less than 1 fs [57]. Alternatively, resonant structures dramatically lower the THz power by a factor  $> 1000$  for effective compression and characterization of ultrashort electron pulses. Whereas the former opens the prospect of a PHz-bandwidth cathode-ray oscilloscope as an alternative to attosecond photon-pulse metrology [184], the latter may lead to unprecedented spatio-temporal resolutions in pump-probe electron diffraction and imaging.

The moderate field strengths applied in our experiment offer the potential for increasing the interaction strengths by more than two orders of magnitude, limited by the high values of electrical breakdown at THz frequencies. This will result in correspondingly reduced propagation distances between subsequent THz control

stages, which, in turn, should improve the passive few-fs timing stability into the sub-femtosecond regime. Simultaneous compression of 100-fs-scale input electron pulses to near-1-fs duration will permit spatiotemporal imaging of the fastest structural and infrared-field-driven electron dynamics in molecular systems [48] as well as condensed matter [28] by single-electron diffraction [112] or microscopy [176] and allow measuring microscopic/atomic scale electric field waveforms up to frequencies of visible light.

The demonstrated all-optical control may also be helpful for manipulating ultra-bright multi-electron bunches. Compact electron guns have demonstrated sub-200-fs electron pulses with sufficient charge for single-shot structural dynamics studies [32]. Our concept is directly applicable to them as well. Alternatively, single-shot ultrafast electron diffraction may be advanced into the few-femtosecond regime and possibly beyond by THz-streaking 100-fs-scale probe pulses after passage through the sample [136]. The unprecedented temporal resolution of the THz-driven streak camera could also be used to characterize electron micro-bunching in free-electron lasers, supplementing THz-based diagnostics for the X-ray output [186, 187]. The demonstrated concept is scalable to higher THz frequencies and multiple stages, offering the potential for cascaded compression into the sub-femtosecond regime or direct injection into a single optical cycle of a laser-field accelerator [75]. This may, in the long run, lead to isolated attosecond electron pulses for recording dynamic changes of electron distribution in complex systems, including biological molecules and solid-state nanostructures.

## Acknowledgments

This work was supported by the European Research Council and the Munich-Centre for Advanced Photonics. We thank D. Frischke for preparing ultrathin aluminum foils. The authors declare no competing financial interests.

# Electron energy analysis by phase-space shaping with THz field cycles

In the previous chapter, a terahertz-based streak camera was introduced, featuring few-femtosecond temporal resolving power of electron pulse arrival times. This concept not only enables temporal characterization of electron pulses with unprecedented resolution (see Chapters 4, 6 and 7), its precision can also be used to retrieve electron energy spectra of femtosecond electron pulses. The realization of a method to do so is the subject of this chapter.

## 5.1 Preface

Ultrafast electron diffraction techniques usually rely on the signal of elastically scattered electrons from a sample under investigation, but the inelastically scattered electrons also carry valuable structural information that is contained in their energy spectrum. Access to the spectral information of keV-electron pulses is usually obtained using magnetostatic electron energy analyzers, which, due to their elaborate electron optics, impose stringent constraints on electron beam quality.

An alternative technique for the retrieval of electron spectra is based on time-of-flight (ToF) measurements. Determining the arrival time of a particle at a certain position relative to another particle which started from the same position at the same time, allows inferring their difference in velocity and, consequently, in kinetic energy. However, the higher the overall kinetic energy of the particles, the smaller their separation in time for a given propagation distance and energy difference. Therefore, ToF techniques are usually employed in the low electron energy regime of tens to hundreds of eV, where the arrival time differences are typically in the nanosecond range and can be read out by conventional electronics.

The few-femtosecond arrival time resolution of the terahertz-driven streak camera (Chapter 4) pushes the capabilities of the ToF concept towards new frontiers. Its combination with phase-space manipulation techniques via temporal lenses (see Chapter 2), as demonstrated in this work, allows to bring the energy resolution of the technique to the cathode limit, that is the intrinsic energy resolution given by the energy spread at the electron source, and potentially beyond (see also [188, 133]).

This chapter provides a detailed study of the capabilities of a terahertz-based, all-optical time-of-flight electron energy analyzer (THz-ToF). By virtue of the unique combination of terahertz-based electron pulse compression and streaking (see Chapter 4)<sup>1</sup>, electron energy loss spectroscopy [131] of a thin aluminum sample using 70-keV electron pulses is demonstrated with few-eV resolution (Fig. 5.2). Note, that at the time the experiment was conducted, the energy resolutions was mainly limited by restrictions in electron pulse compression using bow-tie resonators (Chapter 4). Using the improved electron pulse compression scheme described in Chapter 7, a resolution of below 1 eV (rms) is expected, only limited by the energy spread at the electron source.

Simulations shown in this chapter reveal that this limit can be circumvented by adding another temporal lens, which spreads the electron pulse in time prior to the sample and the subsequent compression of the pulse (see Fig. 5.3). Even though by doing so the electron pulse gains energy spread, the uncorrelated energy bandwidth reduces upon propagation. For a highly correlated electron pulse being compressed after the interaction with the sample, the energy resolution is improved in proportion to its increase in duration. This concept, as originally proposed in [133], is a variation of the dynamic monochromator scheme introduced in Section 2.7 of Chapter 2. In addition to this thesis' previous theoretical treatment, the simulations shown here also account for the nonlinearities and single-cycle behavior of the compressing terahertz field.

In the course of this thesis, the setup built for the electron pulse compression experiments of Chapter 4 has been extended to perform all-optical electron energy analysis as detailed in the following article. A proof-of-principle spectroscopic study has been conceived and realized along with phase-space simulations, which show a way to increase the energy resolution of the scheme. The results are published in *Structural Dynamics*, Vol. 5, p. 044303 in 2018.<sup>2</sup> The following text (pp. 75–86) is a reprint of the original article [103].

---

<sup>1</sup>The setup is nearly identical to the one described in Chapter 4, with the only addition being the sample from which the electron energy loss spectra were obtained (see Fig. 5.1).

<sup>2</sup>Author contributions: Setup by DE and CK. All experiments and data evaluation performed by DE under the supervision of PB and with assistance by CK. Numerical study by DE in discussion with PB and CK. All authors discussed the results and wrote the manuscript based on a first draft by DE.

# Electron energy analysis by phase-space shaping with THz field cycles

Dominik Ehberger, Catherine Kealhofer, Peter Baum

## Abstract

Time-resolved electron energy analysis and loss spectroscopy can reveal a wealth of information about material properties and dynamical light-matter interactions. Here, we report an all-optical concept for measuring energy spectra of femtosecond electron pulses with sub-eV resolution. Laser-generated terahertz radiation is used to measure arrival time differences within electron pulses with few-femtosecond precision. Controlled dispersion and subsequent compression of the electron pulses provide almost any desired compromise of energy resolution, signal strength, and time resolution. A proof-of-concept experiment on aluminum reveals an energy resolution of  $< 3.5$  eV (rms) at 70-keV after a drift distance of only 0.5 m. Simulations of a two-stage scheme reveal that pre-stretched pulses can be used to achieve  $< 10$  meV resolution, independent of the source's initial energy spread and limited only by the achievable THz field strength and measuring time.

© 2018 Author(s). Reprinted under the terms of the [Creative Commons Attribution 4.0 International](#) license.

doi:10.1063/1.5045167

## 5.2.1 Introduction

Ultrashort electron pulses of femtosecond and attosecond duration allow direct visualization of the fastest atomic and electronic processes in matter with simultaneous resolution in space and time [31, 33]. Diffraction patterns of crystalline materials or real-space images of complex morphologies obtained in a pump-probe way have already elucidated numerous ultrafast phenomena in gaseous, solid, and liquid environments [189, 34, 8, 190, 42, 41], and researchers are continuing to explore even more fundamental processes [130] or more complex materials [39].

Besides the tremendous spatial and temporal resolution offered by the latest technology advances [108, 89, 43–45, 65], there is also much useful information hidden in the energy distribution of the probing electrons. Electron energy loss spectroscopy

(EELS; see Ref. [131] for a review) is therefore a widespread method to obtain fundamental chemical and structural information from complex materials. For example, plasmonic [191] or vibrational excitations [192] can be probed with spectral and spatial resolution of  $\sim 10$  meV and  $< 1$  nm at the same time [192]. Recently, the capabilities of EELS have also been extended to the femtosecond domain [193]. Even core-loss spectra can be recorded with nanosecond temporal resolution [194].

An energy analyzer for electrons at energies of tens to hundreds of keV is central to these types of experiments. The desired resolution is  $< 1$  eV for studying laser-electron interactions [77, 82, 78, 76] and ideally meV for studying phonon excitations [192, 195] or details of plasmonic effects. Such resolution is typically achieved by rather bulky and expensive analyzers based on deflection magnets and chicanes. Also, those magnetostatic analyzers put stringent restrictions on the beam quality that are difficult to meet with laser-generated ultrashort electron pulses such as required for time-resolved investigations.

Time-of-flight (ToF) energy analyzers, on the other hand, measure the relative arrival times of particles in a beam after some drift distance and are, in principle, not limited by finite emittance. However, the nanosecond-scale response of state-of-the-art electronics has restricted the applicability of the ToF concept to rather low electron energies in the sub-keV regime [196]. Recently, 0.5-eV resolution of 30-keV pulses has been achieved by deceleration of the beam to a drift energy of only a few eV [197].

The close relation between time and energy in femtosecond electron pulses offers another, dynamical approach for energy analysis [188]. The idea is to measure arrival time differences with femtosecond instead of nanosecond resolution. Additionally, smart phase-space shaping prior to temporal detection allows for substantial improvement of the energy resolution at cost of time resolution [198]. A first demonstration of such type of ultrafast time-of-flight analysis was made with a series of microwave cavities [188, 198] that are synchronized to each other.

Here, we apply all-optically generated THz pulses for time-of-flight electron energy analysis. This approach avoids the need for temperature stabilization [66] or active synchronization [64, 67] to a femtosecond laser for pump-probe investigations. Throughout the experiment, the mean electron energy is left unaltered and thus no deceleration into a drift stage is required. The necessity of a magnetically shielded environment is largely reduced, because magnetic beam deflection scales inversely with the electron velocity. In addition, THz pulses are naturally synchronized to femtosecond lasers [89], facilitating high-resolution pump-probe investigations.

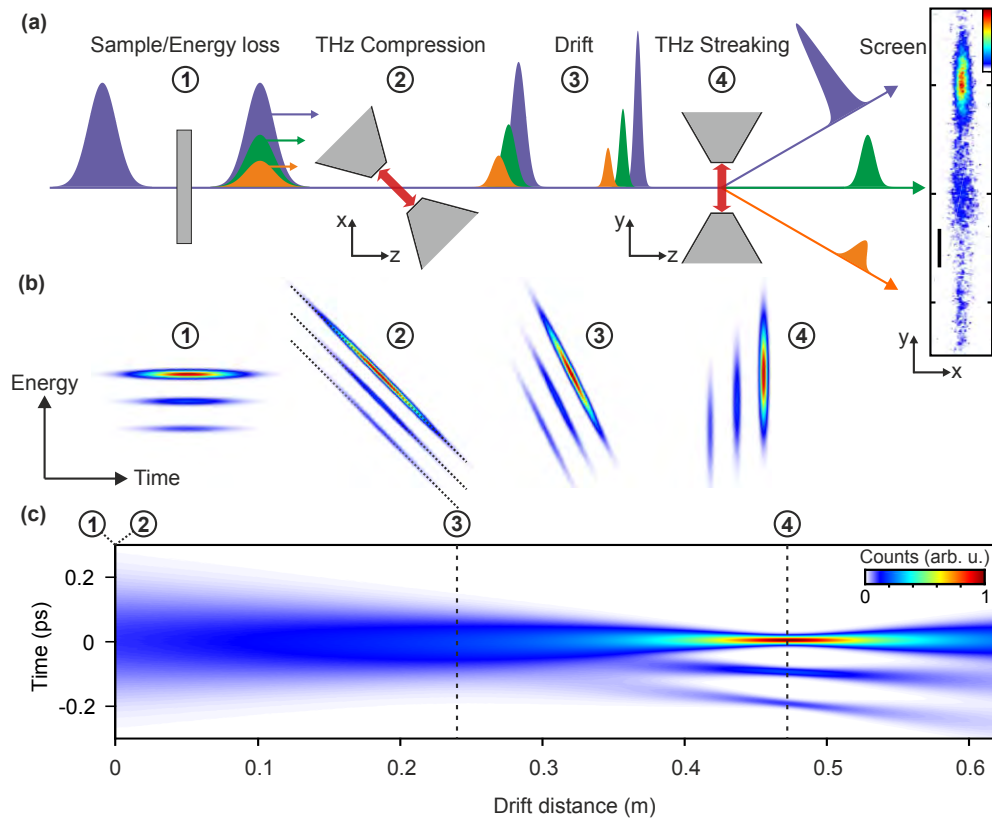
### 5.2.2 Concept for THz-based time-of-flight detection

Figure 5.1 a depicts the principle of operation of our THz-ToF detector and its essential components. An initial electron pulse (purple) from a laser-triggered photocathode interacts with a sample (grey) and thereby modulates the spectrum of the electron pulses in a material-specific way (green and orange pulses). Subsequently, the energy-modulated parts of the pulse travel at different mean velocities. The resulting arrival time differences are detected after a certain drift distance with femtosecond accuracy via streaking with THz-pulses [89]. As compared to conventional, electronic time-of-flight detectors, we have here  $10^3$ – $10^4$  times better resolution. This enhancement allows us to avoid any deceleration and few-eV drift stage.

Compression of the electron pulse in time can further enhance the resolution, because shorter electron pulses can better be detected in time. For compression, the electrons pass through a bow-tie shaped metal resonator (grey) again driven by THz field cycles. They obtain a longitudinal momentum kick, which varies in strength as a function of arrival time. By setting the timing such that earlier electrons in the pulse are decelerated and later ones accelerated, the resonator acts as a focusing lens in time [89]. It creates a correlation between a particle's position within the pulse (proportional to time) and its forward momentum (approximately proportional to energy). There is an analogy to optical lenses which establish a correlation between transverse beam position and angle with the optical axis [126]. Accordingly, a temporal focus—defined as the point in space of minimum pulse duration—is obtained at some drift distance from the compression element. If the electron spectrum is modulated, each part is focused approximately to the same temporal focus, but arriving at a different time. This temporally mapped spectrum is detected by the streaking of the beam with a second bow-tie resonator [89]. In the end, on a screen behind the streaking element, we detect a distribution of particle positions that reveals the energy spectrum.

Figure 5.1 b shows a phase-space representation of the concept. We start with an electron pulse with a zero loss peak and two different energy loss peaks (1). Next, there is the phase space transformation by the temporal lens for compression (2). Earlier electrons are slower than later ones. Next, the phase space distribution shears under propagation (3) until it is rotated by  $90^\circ$  with respect to its initial state. This position is the temporal focus (4). Here, measurements of distributions of electron arrival times via streaking become measurements of the initial energy distribution. Figure 5.1 c depicts the evolution of the temporal profile on the pulses' way to the temporal focus. At this position, the energy loss peaks are well separated from the zero loss peak.

Conversion from time to energy is approximated by linearization of the kinematic equations for relativistic electrons. The approximation is valid if the energy loss  $\delta E$



**Figure 5.1:** Setup and concept. (a) An electron pulse (purple) is modulated in energy via interaction with a sample (1). The pulse passes through a bow-tie resonator irradiated with a THz pulse and obtains a time dependent, longitudinal momentum modulation (2) that leads to compression upon further propagation (3). Electrons with different forward velocities (green, orange) are separated in time while being compressed. Temporal characterization in the temporal focus via streaking with a THz-illuminated bow-tie resonator (4) allows discriminating electrons of different initial energy on a screen (right panel; scale bar corresponds to 0.5 mm; linear color scale from 0 to 1 in arbitrary units). (b) Energy-time phase-space picture of this time-of-flight electron energy analysis with temporal lenses. Dotted lines indicate the compression slope. (c) Simulated evolution of the temporal profile of a 250-fs electron pulse with hypothetical energy losses of 5 eV and 10 eV. The initial energy spread of the source is set to 1 eV FWHM and we assume linear phase space transformations and no electron-electron interactions. The temporal focus is 46.8 cm behind the compression element, as in the experiment.

(typically  $< 100$  eV) is much smaller than the mean kinetic energy  $E_0$  of the beam (typically 30–300 keV). Using the Lorentz factor  $\gamma = (1 - \beta^2)^{-1/2} = 1 + E/(m_e c^2)$ , the electron velocity  $v = \beta c = c\sqrt{1 - \gamma^{-2}}$ , the speed of light  $c$ , and the electron mass  $m_e$ , we obtain

$$\frac{dv}{dE} = \frac{\partial v}{\partial \gamma} \frac{d\gamma}{dE} = \frac{c}{\beta \gamma^3} \frac{1}{m_e c^2} \quad (5.1)$$

and

$$\frac{dt}{dv} = -\frac{d}{v^2}. \quad (5.2)$$

With knowledge of  $E_0$  and the distance  $d$  between compression and streaking, we can convert arrival time differences  $\delta t$  to differences in energy via

$$\delta E \approx \frac{\beta_0^3 \gamma_0^3 c^3 m_e}{d} \delta t, \quad (5.3)$$

where  $\gamma_0 = \gamma(E_0)$  and  $\beta_0 = \beta(\gamma_0)$ .

Equation 5.3 also holds if there is a finite propagation distance between the sample and the compression element. Although the energy loss pattern (1) further disperses in time, the compressor offsets this effect. If electrons at a given energy arrive earlier or later, they obtain a correspondingly greater or lower longitudinal momentum kick and always arrive at the temporal focus at the same time [57]. Basically, the distribution (2) just shifts along the dotted lines. The analogy to the optical lens is apparent: it does not matter at which transverse position (time) the lens is hit, only the angle (energy) determines the transverse position of (arrival time at) the focus (temporal focus).

### 5.2.3 Experimental setup

In the experiment, we use frequency-doubled laser pulses from a 1-ps, Yb:YAG thin-disk laser with a central wavelength of 1030 nm (Ref. [153]) at 50 kHz to trigger electron emission from a back illuminated flat gold cathode that is held at  $-70$  keV with respect to a grounded anode that is 25 mm apart [111]. The same laser source is used to generate single-cycle THz pulses at 0.3 THz central frequency [153, 102] for compression and streaking with bow-tie resonators [89]. Both resonators are designed to resonantly match the central frequency of the driving THz pulses. In the center, the resonators have a clear aperture of 80  $\mu\text{m}$ . Two magnetic solenoid lenses, one before and one after the compression element are used to steer the electron beam through the resonators without clipping. Space charge effects are largely circumvented by using less than 10 electrons per pulse. The electron pulses first pass through a  $\sim 70$  nm thick freestanding Al foil where they lose energy by inelastic plasmon scattering; the total transmission through the foil is  $\sim 30\%$ . After propagation for 2 mm, the pulses

arrive at the first bow-tie resonator which serves as compression element. It is rotated by  $\sim 45^\circ$  around the  $y$  axis (see Fig. 5.1 a). The electron and the THz beams cross approximately at right angle. This configuration provides a non-zero component of the electric field along the electrons' trajectory [89]. The THz peak field strength impinging onto the first resonator is  $\sim 5 \times 10^5$  V/m in order to let the temporal focus coincide with the position of the second resonator used for streaking at a drift distance of  $d = (46.8 \pm 0.5)$  cm. The THz peak field strength driving the second resonator is  $\sim 1 \times 10^6$  V/m. The streaking resonator is excited collinearly with the electron beam. This configuration leads to a sideways deflection of the electron beam which is detected by a camera equipped with a scintillator screen [113]. In order to enhance the streaking resolution, we placed an aperture of 50  $\mu\text{m}$  diameter between compression and streaking stage.

Streaking profiles are obtained by integration of the screen images along the unstreaked dimension ( $x$ -axis, see Fig. 5.1 a). Alternatively, this screen direction could also be used for position-dependent EELS imaging. Figure 5.2 a shows a series of the measured streaking profiles as a function of the delay of the streaking THz field with respect to the electrons. We call such a representation a deflectogram [89]. The center of mass of the deflected electron pulse follows the streaking field inside the resonator. Around the zero crossing (dotted rectangle in Fig. 5.2 a), we measure a temporal resolution of 12 fs (rms). Via Eq. 5.3, this time resolution corresponds to an energy resolution of 0.6 eV.

### 5.2.4 Results

In the deflectogram of Fig. 5.2 a, we see a prominent zero loss deflection trace in addition to several weaker traces that are each delayed by roughly 300 fs. Figure 5.2 b shows a close-up of the region around the zero-crossing in Fig. 5.2 a that is marked with a dotted rectangle. We clearly see three distinct features that are delayed in time. Averaging along these traces and application of the time-energy conversion according to Eq. 5.3 yields the energy spectrum depicted in Fig. 5.2 c. We find two energy loss peaks at  $(14.9 \pm 0.2)$  eV and  $(29.9 \pm 0.3)$  eV. A third peak may be hidden in the background.

Aluminum's bulk plasmon has an energy of 15.0 eV [131]. The two observed EELS peaks are therefore the first-order and second-order plasmon losses in Al. From the width of the measured zero-loss peak, as shown in Fig. 5.2 c, we infer an upper limit for the energy resolution of 3.5 eV (rms) of our THz-ToF, which corresponds to a relative accuracy of  $5 \times 10^{-5}$ . Earlier measurements of electron pulse duration without the aluminum sample [89] indicate an energy resolution in our setup of down to 1.7 eV (rms). The electron pulse duration at the Al sample is in the femtosecond

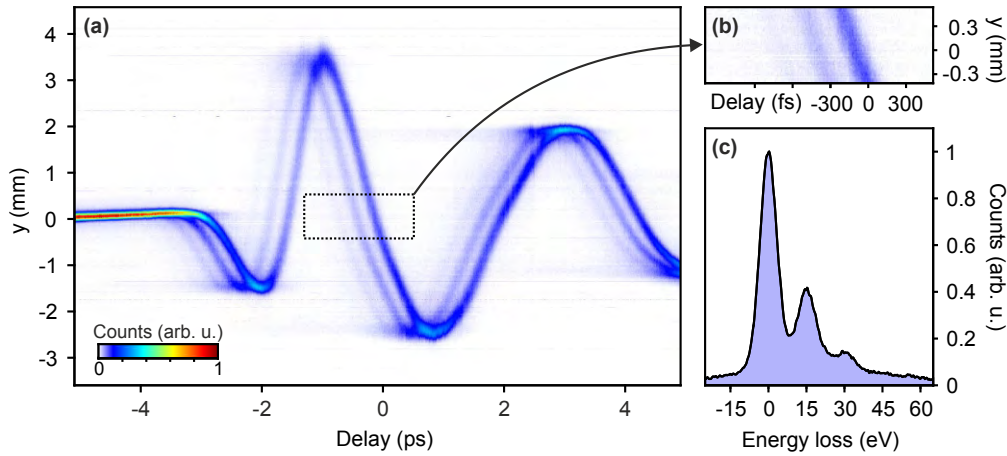


**Figure 5.2:** Experimental results. (a) Deflectogram of the compressed electron pulses after passage through a  $\sim 70$  nm thick aluminum sample. The two shadow traces indicate the energy loss due to inelastic plasmon scattering. (b) Details of the deflectogram. The loss traces are each delayed by  $\sim 300$  fs. (c) Measured electron energy loss spectrum of the Al foil. There are peaks at multiples of 15 eV, corresponding to the bulk plasmon energy.

regime and therefore the setup would, in principle, allow femtosecond pump-probe investigations.

### 5.2.5 Discussion

In the configuration presented above, the energy resolution is fundamentally limited by the bandwidth of the electron source (see Fig. 5.1 b). The typical bandwidths of laser-driven electron sources are 0.5–1 eV (Ref. [82]) or larger, depending on the amount of space charge. For flat cathodes, the initial energy spread can be reduced by matching the cathode material's work function to the triggering photon energy [111, 110], which, in principle, allows for a resolution of  $\sim 0.1$  eV. Electron beam monochromators like used in state-of-the-art electron microscopes [132] would help to improve the resolution even further. Practically, the resolution in our scheme is limited by the ability to compress the electron pulses. While timing problems due to jitter are largely avoided by our all-optical approach [89], nonlinearities of the phase space transformations and spatiotemporal distortions arising from magnetic solenoid lenses [199] are responsible for energy resolution imperfections. These temporal lens aberrations can be overcome by careful lens alignment [200], using shorter initial electron pulses, and by compression elements that allow for velocity matching [82, 100].

The finite cycle duration of the streaking THz field restricts the energy range that can be measured. For our experiment, the measurement window is  $\sim 80$  eV,

considering the turning points of the streaking trace as the main limiting factor. This range is already enough for most experiments on plasmons or optical modulations, but if necessary it can be improved by decreasing the drift distance  $d$  and increasing the compression and streaking field strengths. The spectral features will be denser in time and thus a broader energy range will be covered by a single streaking half-cycle. Such an increase in detection range would, for example, allow femtosecond core-loss spectroscopy with keV-scale energy losses.

The potential compactness of our THz-ToF is one of its most prominent features. The length of the necessary beam line is solely determined by the available THz field strength. The drift distance is determined by the shortest achievable temporal focal length and the energy resolution scales with the THz power at the streaking element. Electron beam modulation has been demonstrated with THz peak fields exceeding  $10^7$  V/m [95], about 20 times larger than in our experiment. With such sources, our THz-ToF could reach a length of merely centimeters.

### 5.2.6 Multi-stage THz-ToF for energy resolution beyond the cathode limit

An energy resolution even better than the initial energy spread of the electron source can be achieved by adding one more THz-electron interaction stage, as originally proposed by Verhoeven et al. for microwave cavities [198]. This THz stage acts a stretcher, that is, a negative temporal lens that accelerates the leading part of the pulse and decelerates its trailing part. A phase-space representation of this process is depicted in Fig. 5.3 a. Such a stretcher can, for example, be implemented with the well-established methods for compressors [89] but with THz cycles of opposite slope. During subsequent propagation, the electron pulse spreads in time much faster than without the stretcher. If such a chirped electron pulse loses energy in an inelastic scattering process, the parts with the loss are also chirped in the same way. After compression and streaking, the energy resolution is enhanced by factor that depends on the amount of additional electron chirp. However, in this case, nonlinearities of the THz field cycles have to be considered.

In order to investigate this possibility, we simulated the evolution of an EELS dataset with a hypothetical 100-meV modulation (for example, phonon excitations) as a function of stretcher field strength. We assume single-cycle THz pulses at a central frequency of 0.3 THz. The electron pulses have an energy of 100 keV, 100 fs initial duration, and 1 eV energy spread (both FWHM). The distance between stretcher and sample is 0.25 m.

The simulation employs a Monte-Carlo algorithm, which calculates the final arrival times of  $10^7$  classical particles after passing through the experiment. Each par-

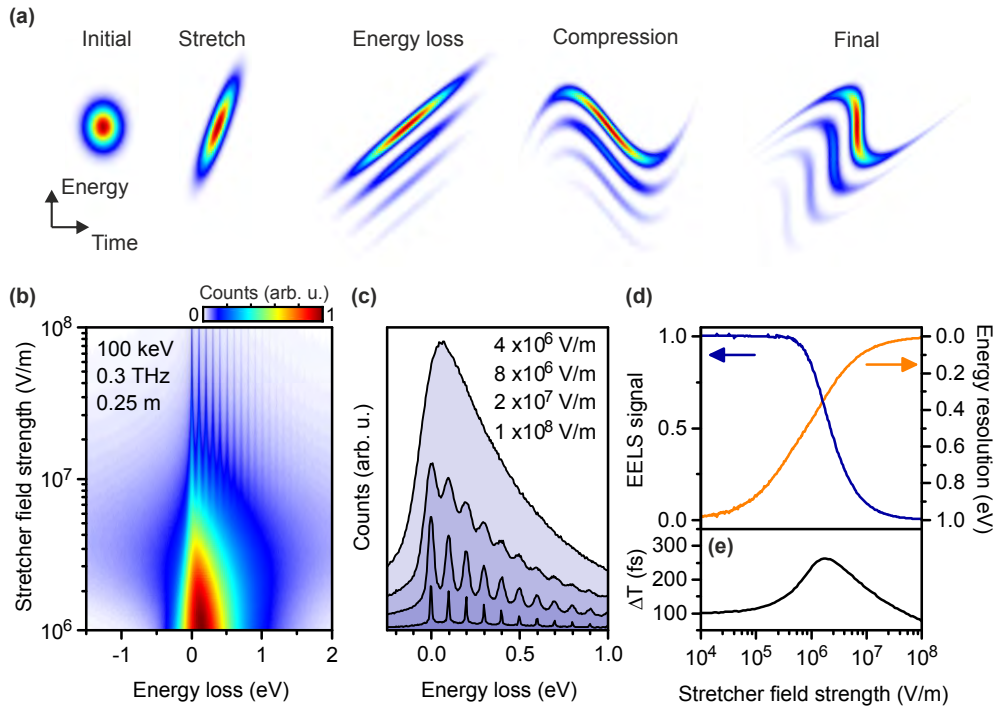


**Figure 5.3:** Simulation of a two-stage THz-ToF for increased energy resolution. (a) Sequence of phase space transformations. Here, nonlinearities of the THz fields at the compression stage are taken into account by assuming a single-cycle, sine-like velocity modulation. The compression therefore becomes, in part, nonlinear for strongly stretched pulses. (b) Electron energy loss spectra of hypothetical 100-meV features in an electron energy loss spectrum for different stretcher field strengths. The beam energy is 100 keV and modulation is made by single-cycle THz pulses with a central frequency of 0.3 THz. The source's initial energy spread and pulse duration are 1 eV and 100 fs (FWHM), respectively. The drift distance between stretcher and compressor is 0.25 m. (c) Resulting energy spectra for different stretcher field strengths as indicated by color. (d) Useful EELS signal (relative) and energy resolution (FWHM) as a function of the stretcher field strength. (e) Effective temporal resolution,  $\Delta T$ , defined as the FWHM of the longitudinal electron distribution at the sample within the FWHM of the EELS peaks.

ticle is defined by its velocity and longitudinal position and obtains a nonrelativistic velocity kick at the stretcher and compressor, which varies as a function of the arrival time. The strength of this sinusoidal modulation at the stretcher is varied and the strength of the compressor is chosen such that the temporal focus remains at 0.5 m. Energy loss at the sample is modeled by random, and uncorrelated velocity changes corresponding to the assumed fundamental energy loss and its multiples. Coulomb interactions between the particles are neglected.

Figure 5.3 b shows the simulation results, plotted as the effective electron energy loss spectrum as a function of the stretcher strength. We observe distinct spectral features to become visible above a stretcher field strength of  $\sim 10^7$  V/m. Below that value, only the envelope of the spectrum is visible without the details. The higher the stretcher strength, the finer the resolution, but the total number of useful electrons in the spectrum decreases. Figure 5.3 c shows cuts through Fig. 5.3 b at four selected THz field strengths. We see an improvement of resolution as well as a decrease in signal.

The increase in resolution is a consequence of the sheared phase space shape created by the stretcher (see Fig. 5.3 a). The decrease in electron count is caused by the finite cycle duration of the compressing THz pulse. The stronger the stretching, the longer the electron pulses become at the compressor. If they are longer than one THz half-cycle, some parts of the electron pulse are not compressed and arrive continuously at the temporal focus (see Fig. 5.1 a). Hence, there is in the final EELS data a constant background in energy (see Fig. 5.3 b) at highest field strength]. Nevertheless, depending on the required measuring times for achieving a sufficient signal-to-noise ratio, down to 10 meV resolution can be realized for the given parameters.

Figure 5.3 d summarizes these results. The energy resolution is taken from the simulations as the width of the zero-loss peak. We define the useful EELS signal as the number of electrons within the full-width half-max of the zero-loss peak and compare it to the case of perfectly linear phase space transformations for which there is no loss in signal. We see that the useful signal (blue) decreases in a nonlinear way with increasing stretcher field strength. The energy resolution (orange, FWHM) increases accordingly. A simple adjustment of the THz field strength at the stretcher can therefore be used to achieve the best compromise between signal strength and resolution for a given sample system.

Interestingly, the time resolution  $\Delta T$  of a potential pump-probe experiment does not significantly depend on such an alignment. The reason is that the single-cycle pulses used for compression act as a temporal filter that only compresses such electrons that arrive within the linear slope of the field around the zero crossing of the central half cycle. All other electrons only produce a constant background with neither energy nor time resolution. Figure 5.3 e depicts the effective time resolution

that can be expected for the chosen parameters. We see that for negligible stretching ( $< 10^5$  V/m), the time resolution remains 100 fs, the initial electron pulse duration after the gun. For stronger stretching,  $\Delta T$  becomes worse as the energy resolution improves (compare Fig. 5.3 d, orange line). Interestingly, if the stretching is further increased, the time resolution again improves, now mainly at cost of the reduction of signal strength (compare Fig. 5.3 d, blue line). This effect is different as compared to microwave approaches [198] and a direct consequence of the pulsed, single-cycle nature of our THz fields. Summarizing, it means that in our case, adjusting the energy resolution far beyond the cathode bandwidth limit always comes at the cost of signal strength. However, in situations where low signal is tolerable, the approach allows to have extraordinary high resolution in both energy and time, fundamentally limited only by the uncertainty principle.

### 5.2.7 Conclusions and outlook

In conclusion, we have shown an all-optical approach to measure energy spectra of femtosecond electron pulses via THz-based time-of-flight measurement in a temporal focus. The inherent synchronization of THz pulses with a pump laser pulse renders the scheme as a useful tool for time-resolved EELS measurements on femtosecond and potentially attosecond time scales. In contrast to magnetic chicanes or related approaches, our concept is largely independent of the electron beam's transverse emittance. It can therefore well be combined with high-brightness, flat emitter sources [33] which are useful for many pump-probe investigations of complex materials. In dense multi-electron pulses, linear stretching can be generated via the space charge expansion of elliptical electron packet shapes [124] instead of the THz-stretcher used here.

In practice, the presented concept offers a compact, simple, high-resolution pump-probe electron energy loss or gain spectrometer with table-top dimensions and without need for microwave electronics. One can conceive upcoming applications in concurrent research on, for example, time resolved electron spectroscopy [193, 201], quantum metrology of electron pulses [78], attosecond pulse generation [43–45], or photon induced near-field microscopy [77]. In waveform electron microscopy [99], where electrical field vectors are detected in space and time, an additional energy resolution such as achievable with the presented approach could reveal, in addition, the longitudinal field components in a direct way.

## Acknowledgments

This work was supported by the European Research Council, the Munich Centre of Advanced Photonics, and the International Max-Planck Research School for Advanced Photon Science.

# Chapter 6

## Tilted electron pulses

Thus far in this thesis we have been mainly concerned with one-dimensional electron pulse control. In that sense we have pictured electron pulse manipulations for compression as mainly longitudinal and treated spatial inhomogeneities and time dependent deflection as unwanted effect. However, the defined interplay of time-dependent transverse *and* longitudinal momentum transfer offers new possibilities for multidimensional electron pulse control as demonstrated in this chapter by the deliberate generation of tilted electron pulses.

### 6.1 Preface

Tilted electron pulses are defined by having a non-zero angle between their propagation axis and current density normal, which is in analogy to their optical counterpart. However, in contrast to tilted laser pulses, which are ubiquitous in modern laser applications (see for example dielectric laser acceleration [202], X-ray lasing [203, 204], terahertz pulse generation [159], parametric amplification [205], quantum optics [206] or non-isotropic material processing [207]), tilted electron pulses are largely absent from research literature. This is even though they are expected to boost the performance of free-electron lasers [208] and allow for highest temporal resolution using them as probe in ultrafast electron diffraction and microscopy experiments (see Fig. 6.5).<sup>1</sup>

The central element of the following experiments, which allows us to introduce a novel tool for terahertz-based electron pulse shaping, is an ultrathin, electron-

---

<sup>1</sup>Temporal mismatch between excitation and probe pulses in a non-collinear configuration can also be avoided by tilting the optical excitation pulse [209, 8, 42]. However, for investigation of laser-induced sub-cycle dynamics with electrons [48, 28], the probe pulse must be tilted, because the phase front of an optically tilted pulse overall remains perpendicular to the propagation axis.

transmitting and optically reflecting mirror (Fig. 6.1 a). Due to an electron's abrupt passage through the mirror irradiated by an electromagnetic wave, the particle interacts with a field that is truncated in time. Thus, the Lorentz force this electron experiences does not average to zero in general and a net momentum transfer remains which leads to its deflection, acceleration or deceleration.

Experiments on electron beam manipulation in such a configuration featuring electromagnetic waves at a planar interaction element, have been pioneered by Pletner et al., who used it in combination with visible radiation to accelerate relativistic electrons [81]. Almost a decade later a similar scheme has been used to generate sidebands in energy spectra of nonrelativistic electron pulses for their temporal characterization [82]. Using an optical double-pulse excitation in this configuration, the control over the electron spectrum has recently been refined [83]. Furthermore, it has been shown that attosecond electron pulse trains can be generated using near-infrared radiation at a dielectric planar membrane [44]. Even though the latter work involves no reflective element, the momentum transfer scheme is conceptually similar as all of these experiments rely on the asymmetry in electric field imposed by the planar element, which the particle experiences when it crosses the boundary.

This chapter deals with the extension of the *semi-infinite* interaction scheme [81] to the terahertz regime, using single cycle terahertz transients (see Chapter 3) as control fields. Those, in contrast to the other reported experiments, allow us to manipulate a whole electron pulse of few-hundred-femtosecond duration in an all-optical fashion on a sub-cycle time scale. Other than in Chapter 4, where a similar element was used solely to deflect the electron beam (see Fig. 4.5), here, we investigate and apply the more complex angular dependency of the interaction between optical field and particle beam.

For this purpose, closed-form expressions of the time-dependent electron momentum change are given, including its explicit dependencies on incidence angles, optical field strength and optical frequency (see Eqs. 6.1–6.3). These relations, as derived by coauthor Andrey Ryabov [173], predict a vanishing transverse momentum transfer component, i.e. no electron beam deflection, if the interaction is velocity matched (see also [100]).<sup>2</sup> This coincidence of absent deflection and velocity-matching is particularly surprising because the two concepts are based on independent premises. Time-dependent deflection is a consequence of the integrated Lorentz force acting on the particle as it crosses the mirror [173], but velocity-matching is a purely geometrical consequence of the electron pulse group velocity, the terahertz phase velocity and the respective incidence angles (see Fig. 6.2 b). As it turns out, there is a non-

---

<sup>2</sup>The velocity matching condition (Eq. 6.4) is fulfilled if the mirror element is oriented such with respect to both electron and optical beams, that all electrons in a plane perpendicular to their propagation axis experience the same phase of the electromagnetic wave.

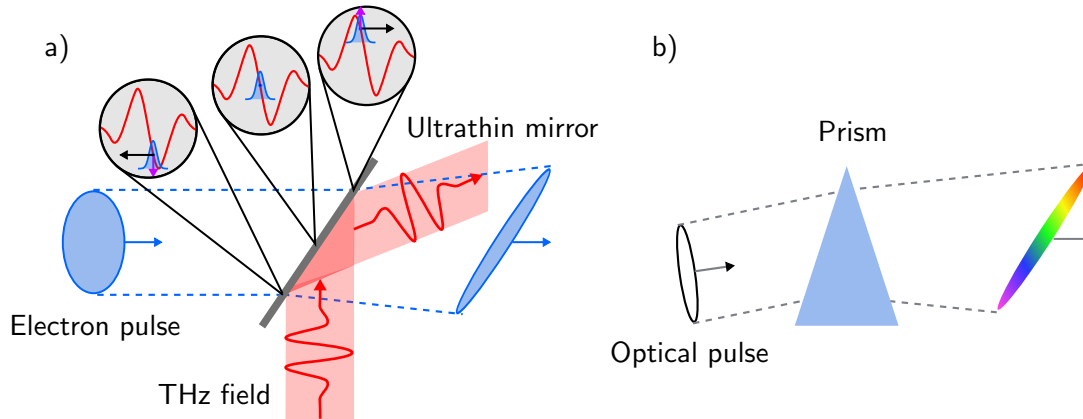


**Figure 6.1:** Generation of tilted pulses. a) Velocity mismatch between a terahertz transient and an electron pulse at a mirror element in a compression configuration leads to the formation of a tilted electron pulse. Insets show the amount of momentum transfer for different parts of the beam. The time dependency of the momentum kick is shifted by  $\pi/2$  with respect to the incident terahertz wave (see text on p. 95). b) Generation of titled optical pulses at a prism, which introduces angular dispersion. Different colors are deflected and delyed by different amounts. This figure is inspired by the viewpoint article [210].

trivial underlying principle connecting these two concepts, which was revealed and substantiated by measurement in the course of this thesis.

In order to understand the governing principle, we need to consider the consequences of a velocity-mismatched interaction between an electron beam and a terahertz wave. This situation is depicted in Fig. 6.1 a. If there is velocity mismatch, the electron pulse experiences different phases of the terahertz wave across its lateral beam profile (see insets). These different lateral parts of the electron beam obtain a velocity offset (black arrows), which delays their arrival time across the transverse beam profile. Upon further propagation, the pulse develops a tilt with respect to its propagation axis, while in addition it is being compressed in time. Hence, velocity mismatch is expected to cause tilted electron pulses.<sup>3</sup>

The electron pulse tilt as a result of transverse delay can be measured by a modification of the all-optical streaking concept introduced in Chapter 4. This modification adds spatial resolution along the unstreaked axis of the beam and has been developed in the course of this thesis. With this metrology, arrival times of electrons having passed through different parts of the mirror can be traced back experimentally (see lower part of Fig. 6.2 a and Appendix C). Measuring the electrons' transverse arrival

<sup>3</sup>The concept of tilted electron pulse formation caused by velocity mismatch is also mentioned in Ref. [100] in the context of attosecond electron pulse train generation at a dielectric membrane. There, however, not the pulse envelope, but rather the substructure appears tilted, due to the electron pulse covering multiple cycles in time.

time delay as a function of the angular configuration (see blue points in Fig. 6.3 c) shows that isolated and compressed electron pulses can be controlled to have a defined tilt angle at a target. As expected from theory, the tilt angle in the temporal focus is set by the angular configuration of the interaction element only (Eqs. 6.5 and 6.6) and equals zero for velocity matching.

Still, these findings do not explain the apparent connection between velocity-mismatch and the strength of time-dependent deflection at the mirror membrane (see Fig. 6.3 c), which was measured in a second, independent measurement. To understand this, we borrow from an optical concept, which relates pulse front tilt to angular dispersion [211]. In optics, angular dispersion can be understood as the rate with which deflection changes per wavelength. It is intrinsic to the optical element that is used to generate tilted pulses, as for example gratings or prisms (see Fig. 6.1 b).

It has been found in the course of this thesis, that the connection between angular dispersion and tilt angle seems also to hold for electron pulses, where the optical wavelength is substituted for the electronic de Broglie wavelength (Eq. 6.7). As it is shown here, the angular dispersion of our terahertz-irradiated mirror membrane is proportional to the ratio of transverse to longitudinal momentum modulation strength (black and magenta arrows in Fig. 6.1), which is given by Eqs. 6.2 and 6.3. Coincidentally, the tangent of the tilt angle is also given by this ratio (see Appendix C). Hence, pulse front tilt of electron pulses is intrinsic to the physics of momentum transfer at the mirror even without the geometrical notion of velocity mismatch. These theoretical considerations are backed by measurement data (Fig. 6.4 a) of the experiments conceived and performed in the course of this thesis, as well as quantum mechanical simulations by Peter Baum (Fig. 6.4 b).

Conclusively, the fundamental principle connecting angular dispersion and tilt angle, which is expressed in Eq. 6.7, forbids tilted electron pulses to form without (time-dependent) deflection in our scheme. And because here, tilted electron pulses require velocity mismatch at the mirror, there is no deflection in a velocity-matched configuration (see above).

In summary, this chapter demonstrates the controlled, all-optical generation and characterization of isolated, tilted electron pulses using experimental tools developed in the course of this thesis. This work furthermore provides the theoretical background required to understand the intrinsic connection between electron pulse tilt and angular dispersion of matter waves, that also governs the formation of tilted optical pulses. The capability to tilt compressed electron pulses will facilitate and improve time resolved electron diffraction and imaging experiments (see Fig. 6.5) and shows the versatility of the terahertz-based pulse compression schemes demonstrated in this thesis.

---

The experimental results, the methodology and the theory behind it are given in the following as a reprint of the original article published in Physical Review Letters (Vol. 121, p. 094801) in 2018 [104].<sup>4</sup> Details on the theoretical background and the measurements are given in [Appendix C](#) as a shortened version of the original article's supplemental material.

---

<sup>4</sup>Author contributions: Concept for tilted electron pulse generation and characterization by DE and PB. Theoretical treatment of momentum transfer at a perfect mirror by AR. Experimental realization and data evaluation of electron pulse front tilt measurements by DE. Quantum mechanical simulations and supervision of the experiments by PB. Theory behind electron pulse front tilt and angular dispersion by DE in close discussion with AR and PB. All authors interpreted the results and contributed to the writing of the manuscript based on a first draft by DE.



# Tilted electron pulses

Dominik Ehberger, Andrey Ryabov, Peter Baum

## Abstract

We report the all-optical generation and characterization of tilted electron pulses by means of single-cycle terahertz radiation at an electron-transmitting mirror at slanted orientation. Femtosecond electron pulses with a chosen tilt angle are produced at an almost arbitrary target location. The experiments along with theory further reveal that the pulse front tilt in electron optics is directly connected to angular dispersion. Quantum mechanical considerations suggest that this relation is general for particle beams at any degree of coherence. These results indicate that ultrashort electron pulses can be shaped in space and time as versatilely as femtosecond laser pulses, but at  $10^5$  times finer wavelength and subnanometer imaging resolution.

© 2018 American Physical Society  
doi:[10.1103/PhysRevLett.121.094801](https://doi.org/10.1103/PhysRevLett.121.094801)

Ultrashort electron pulses allow the direct visualization of atomic and electronic motion during matter transformations in space and time. For generating the necessary few-femtosecond and attosecond electron pulses, technology is currently progressing from microwave electronics to an all-optical control regime, where the optical cycles of laser-generated radiation are used to steer the electrons in a direct and jitter-free way, obviating the need for active synchronization electronics. So far, ultrashort electron pulses have been accelerated [90], compressed [89, 96], energy-modulated [77], and streaked [89, 44] by all-optical approaches, but many applications require more complex phase-space correlations involving multiple dimensions.

Here, we report a multidimensional, dynamical control of electron pulses by all-optical means, exemplified by the generation and characterization of tilted electron pulses. Such pulses, propagating non-normally to their pulse front, promise to improve free-electron laser performance [208] and enable pump-probe experiments in which optical cycles are used for sample excitation [48, 28].

Our concept (Fig. 6.2 a) is based on the controlled phase-space modulation of a beam of electrons (blue) by the cycles of electromagnetic radiation (red). The interaction is mediated by an ultrathin metal mirror (dark gray) in an off-angle geometry. Electrons can pass through, but radiation is reflected. The electrons therefore obtain

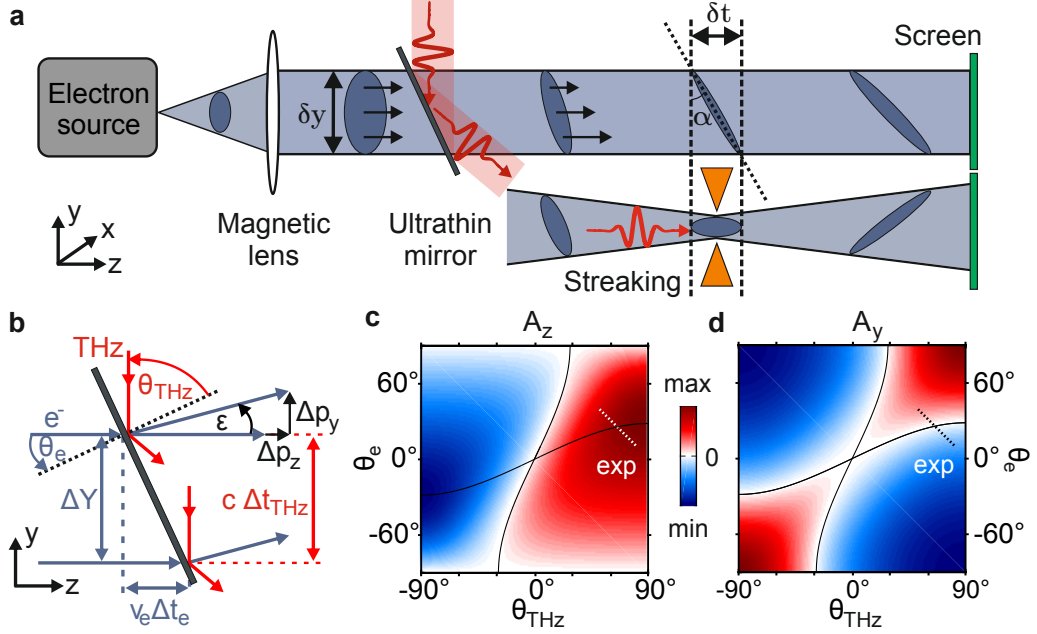


**Figure 6.2:** All-optical generation of tilted electron pulses. (a) Concept and experiment. Electron pulses (blue) pass through a mirror (dark gray) that is irradiated by single-cycle terahertz radiation (red). A traveling interference pattern along the mirror surface converts the electrons into compressed and tilted pulses. (Lower) If the electron beam is focused with the magnetic lens, the tilt angle increases with decreasing beam size, with the opposite sign after its waist. A terahertz-driven resonator (orange) and a phosphor screen (green) provide the necessary metrology to reveal this tilting dynamics by experiment. (b) Definition of angles for the analytical derivations. (c) Amplitude of the longitudinal momentum change as a function of the geometry. (d) Amplitude of the transverse momentum change. (Dotted lines) Angle combinations applied in the experiments; (solid lines) zero-deflection conditions.

a net momentum change from the optical cycles due to their passage through the mirror material within subcycle time [82]. For generating tilted electron pulses with multidimensional correlations in space and time, we place the mirror in such a way in the optical beam that different lateral slices of the electron beam are accelerated or decelerated with a constant gradient across the beam. Simultaneously, we ensure that the entire beam is uniformly compressed in time [89]. Therefore, we expect ultrashort and tilted pulses on a target after free-space propagation.

In order to find the appropriate geometry, we treat the electron beam classically and assume a point charge  $e$  of initial velocity  $v_e = \beta c$  along the  $z$  axis (initial momentum  $p_z$  and  $p_y = 0$ ) that is passing through a perfect mirror ( $y = z = 0$ ) irradiated with a p-polarized plane wave (angular frequency  $\omega$ , peak field strength  $E_0$  at  $y = z = t = 0$ ) as an approximation for the fields in the waist of a Gaussian beam (full width at half maximum  $w_0$ , Rayleigh length  $z_R$ ;  $z_R \gg w_0$ ). The mirror reflec-

tion causes a moving interference pattern with magnetic and electric contributions. An analytic derivation (see Supplemental Material [212, Appendix C]) provides the transverse and longitudinal momentum transfer components  $\Delta p_y$  and  $\Delta p_z$  after the interaction

$$\Delta p_{y,z} = eE_0 A_{y,z}(\theta_e, \theta_{\text{THz}}, \beta) \frac{\sin(\omega t)}{\omega}. \quad (6.1)$$

Here,  $t$  is the arrival time of the electron at the mirror. The amplitude of this sinusoidal momentum modulation depends on the angles  $\theta_e$  and  $\theta_{\text{THz}}$  (see Fig. 6.2 b) via the geometry factors

$$A_y = \pm \left( \frac{\cos(\theta_e + \theta_{\text{THz}}) + \beta}{1 + \beta \cos(\theta_e + \theta_{\text{THz}})} - \frac{\cos(\theta_e - \theta_{\text{THz}}) - \beta}{1 - \beta \cos(\theta_e - \theta_{\text{THz}})} \right), \quad (6.2)$$

$$A_z = \pm \left( \frac{\sin(\theta_e - \theta_{\text{THz}})}{1 - \beta \cos(\theta_e - \theta_{\text{THz}})} - \frac{\sin(\theta_e + \theta_{\text{THz}})}{1 + \beta \cos(\theta_e + \theta_{\text{THz}})} \right), \quad (6.3)$$

where the positive (negative) sign is for the same (opposite) incidence of the electrons and the plane wave with respect to the mirror. The momentum gain is assumed to be small compared to the initial momentum ( $\Delta p_{y,z} \ll p_z$ ) and ponderomotive effects are neglected. Under these assumptions, Eqs. 6.1–6.3 hold for relativistic particles, too.

We find that acceleration and deflection are in phase with each other, regardless of the angles. Furthermore, both momentum changes are phase shifted by  $\pi/2$  with respect to the incident electromagnetic wave. Therefore, cosinelike optical pulses (carrier-envelope phase of zero) lead to sinelike electron momentum modulation (carrier-envelope phase of  $\pi/2$ ) and vice versa. Terahertz pulses from optical rectification typically have a carrier-envelope phase of zero in a focus [102, 153] and therefore provide a sinusoidal momentum modulation. This time dependency of  $\Delta p_z$  causes pulse compression by deceleration of the incoming pulse's earlier parts and acceleration of the later parts. Thus, only half an optical cycle is responsible for compression, and in case of pulses, the relevant part of the momentum kick can be approximated by a modulation with a single frequency  $\omega$  (see Supplemental Material [212, Appendix C]). If an incoming electron pulse is shorter than the optical half-cycle, we obtain isolated electron pulses [89], otherwise pulse trains [44, 43, 45]. The minimum pulse duration is achieved at the temporal focus  $f_{\text{temp}} = (\beta^2 \gamma^3 / A_z E_0)(m_e c^2 / e)$  (see Supplemental Material [212, Appendix C]);  $m_e$  is the electron mass and  $\gamma$  is the Lorentz factor. Analogously, there is a time-dependent sideways deflection via  $\Delta p_y \propto A_y$ , which allows us to realize a cathode ray oscilloscope at optical frequencies [89, 44].

The geometry factors  $A_z$  and  $A_y$  are plotted in Figs. 6.2 c and 6.2 d for electrons with a kinetic energy of 70 keV. We find that there are certain combinations of angles for which  $\Delta p_y = 0$ , that is, no net deflection after interaction. This effect is due to

cancellation of electric and magnetic contributions and occurs for  $\sin \theta_{\text{THz}} = \beta \sin \theta_e$  and  $\sin \theta_{\text{THz}} = \beta^{-1} \sin \theta_e$  (Figs. 6.2 c and 6.2 d, solid lines). For most other angular configurations, we find that deflection and acceleration occur simultaneously, providing opportunity for multidimensional control. The dotted lines mark a convenient region for pulse front tilting experiments, because the deflection is weak there and the compression strength is roughly constant when varying the slant angle of the mirror. The position of the temporal focus is therefore approximately independent of angular adjustments.

For electron beams with a finite diameter, certain angular configurations provide velocity matching [82], that is, all electrons have the same relative delay to the optical cycles regardless of their position within the beam (Fig. 6.2 b). Velocity matching is achieved if

$$\frac{c}{\sin \theta_{\text{THz}}} = \frac{v_e}{\sin \theta_e}, \quad (6.4)$$

that is, if the superluminal phase velocity of the optical interference pattern along the mirror surface equals the surface velocity of the electron pulse's point of incidence. In order to generate tilted electron pulses, we rotate the mirror away from this velocity-matching condition. This simple adjustment produces a lateral timing mismatch  $\Delta T = \Delta t_{\text{THz}} - \Delta t_e$  between the optical cycles and electrons of different beam positions  $\Delta Y$  (Fig. 6.2 b). Considering the geometry depicted in Fig. 6.2 b, we obtain

$$\frac{\Delta T}{\Delta Y} = \frac{\sin \theta_{\text{THz}}/c - \sin \theta_e/v_e}{\cos \theta_e}. \quad (6.5)$$

If the position-dependent delay is smaller than a half-period of the optical radiation, the momentum modulation is nearly linear in space and time. Therefore, incoming electron pulses obtain a position-dependent overall acceleration or deceleration in addition to the time-dependent longitudinal momentum modulation that causes compression. Consequently, there is a constant velocity-gain gradient along the transverse beam profile (Fig. 6.2 a) and different slices of the beam profile arrive earlier or later at the target, that is, as tilted pulses. The lateral arrival time difference of  $\delta t/\delta y$  results in a tilt angle  $\alpha = \tan^{-1}(v_e \delta t/\delta y)$  for a collimated beam (Fig. 6.2 a). At the temporal focus, we find  $\delta t/\delta y = \Delta T/\Delta Y$  (see Supplemental Material [212, Appendix C]) and thus

$$\tan \alpha = v_e \frac{\Delta T}{\Delta Y}. \quad (6.6)$$

We see that the tilt angle in the temporal focus is solely determined by the combined sweeping dynamics of the electrons and the terahertz cycles across the mirror and is not dependent on the applied optical field strength or its wavelength. According to Eq. 6.6, compressed electron pulses can be produced at almost arbitrary tilt angle  $\alpha$  and position  $f_{\text{temp}}$ , simply by rotating the mirror for the tilt and adjusting the optical field strength for the temporal focus position.

In the experiment, we use single-cycle terahertz pulses (central frequency 0.3 THz [102]) as control fields. The mirror element is a 10-nm Al layer on a 10-nm SiN membrane (size  $1.5 \times 1.5 \text{ mm}^2$ ) with a reflectivity of  $> 90\%$  [213]. The transmission of our 70-keV electron pulses [111] is  $\sim 70\%$ . Space charge effects are avoided by using  $< 5$  electrons per pulse [116] at a repetition rate of 50 kHz. We let the terahertz beam cross the electron beam approximately at  $90^\circ$  (see Fig. 6.2 a). Finite transverse beam size effects of the electromagnetic wave can be neglected, because the electron beam diameter ( $< 1 \text{ mm}$ ) is much smaller than  $w_0$  ( $\sim 3 \text{ mm}$ ) or  $z_R$  ( $\sim 2 \text{ cm}$ ) of the terahertz pulses. The incident peak electric field strength is  $\sim 2 \times 10^5 \text{ V/m}$ , which produces a temporal focus at  $f_{\text{temp}} \approx 0.5 \text{ m}$  and compresses the electron pulses from 1 ps to  $\sim 100 \text{ fs}$ . For pulse tilt characterization, we use a magnetic solenoid lens that creates an intermediate waist (Fig. 6.2 a, lower panel) and therefore a shadow image of the mirror on the screen (green). The half-angle divergence of the electron beam at the mirror is  $\sim 1 \text{ mrad}$ . A butterfly shaped metal resonator (orange) is placed at the waist position, which coincides with the temporal focus. It is illuminated with a second terahertz pulse [153] at  $\sim 9 \times 10^5 \text{ V/m}$  peak field strength and serves as a streaking element, that is, it deflects the electrons along the  $x$  axis (out of the plane in Fig. 6.2 a) as a function of arrival time [89]. This streaking metrology in combination with the shadow imaging allows us to determine the arrival time differences  $\delta t$  between different parts of the beam profile along  $y$ , in order to measure the pulse front tilt of a collimated beam (Fig. 6.2 a, upper panel).

Figure 6.3 a shows raw screen images (each at a zero crossing of the streaking field) for different slant angles of the mirror. The apparent shear in the data directly demonstrates the predicted arrival time differences between electrons originating from different points of the foil (dashed lines) and thus shows that tilted electron pulses are produced.

A quantitative analysis is obtained by recording a series of screen images while scanning the streaking delay (for details see Supplemental Material [212, Appendix C]). This metrology reveals a time-dependent streaking trace for each position  $y$  in the electron beam (Fig. 6.3 b). We see that each slice of the beam deflects with a sinusoidal dependency in time, following the half-cycle of the terahertz streaking field with a position-dependent delay (see inset). The slope of this measured delay is  $\delta t/\delta y$  for the chosen mirror angle ( $\theta_e = 11.3^\circ$  in the figure). Repetition of this procedure for all angles provides the blue dots in Fig. 6.3 c, showing the measured lateral arrival time differences  $\delta t/\delta y$  as a function of  $\theta_e$  and  $\theta_{\text{THz}}$ .

In a second, independent experiment, we determine the relative strength of the transverse momentum kick  $\Delta p_y$  as a function of the mirror angle. To this end, the streaking element is removed and beam position changes are recorded as a function of the terahertz delay at the mirror. An aperture close to the foil (diameter  $50 \mu\text{m}$ )

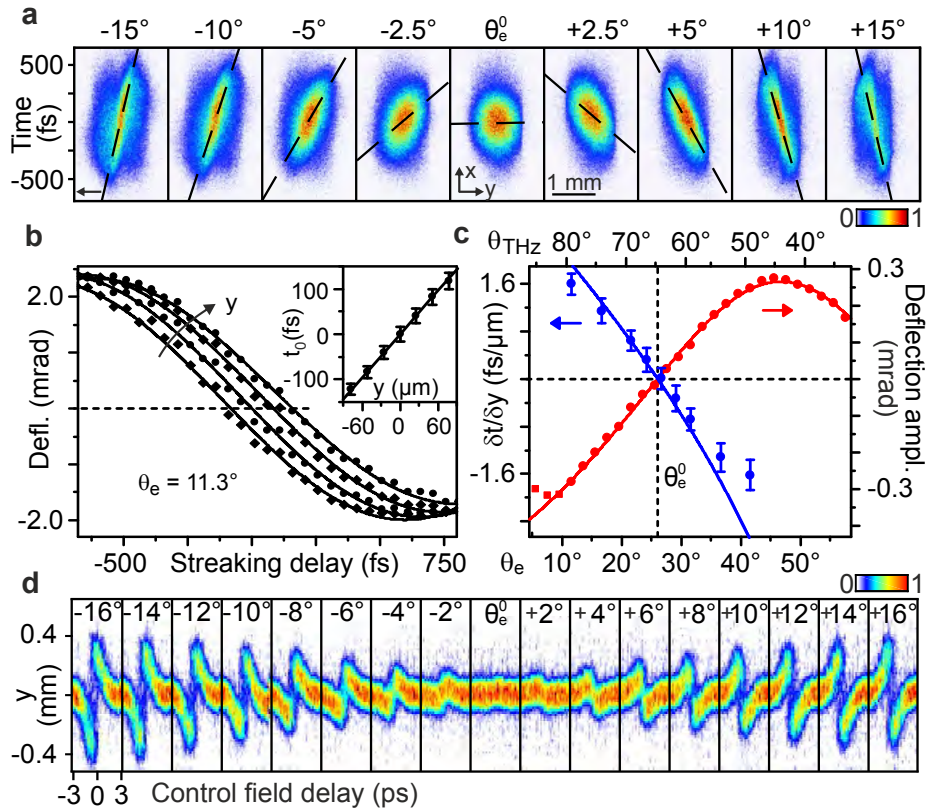


**Figure 6.3:** Experimental results on tilted electron pulses. (a) Screen images for different mirror slant angles at the zero crossing of the streaking field. Scale bar, 1 mm. The pulse front tilt is evident from the measured lateral arrival time differences (dashed line, time axis). (b) Streaking traces (dots and diamonds) for different  $y$  positions within the beam profile and sinusoidal fitting curves (solid). (Inset) Time zero of the streaking traces. (c) Measured arrival time difference (blue dots) and deflection amplitude (red dots). Red line, fit by Eq. 6.2; squares are excluded. Blue line, prediction by Eq. 6.5. Error bars indicate one standard deviation. (d) Time-dependent deflection measurements (deflectograms) for different mirror slant angles.

decreases the beam diameter and a peak field strength of  $\sim 4 \times 10^5$  V/m further enhances the resolution. Figure 6.3 d shows a subset of the measured deflectograms [89] as a function of the mirror angle. The observed time-dependent deflections are proportional to  $\delta p_y(t)$ . We see that all traces are single cycle and sinelike, as expected from our cosinelike terahertz pulses [102] via the considerations above. The peak-to-peak amplitude is proportional to the geometry factor  $A_y$  for sideways momentum transfer and shows a strong dependency on the mirror slant angle (red dots in Fig. 6.3 c). A least-squares fit to the data with Eq. 6.2 reveals the precise angle  $\Delta\theta = \theta_{\text{THz}} + \theta_e$  between the electrons and the terahertz beam in the experiment, as well as a proportionality constant  $C$  that includes the screen distance and electric peak field strength. We obtain  $\Delta\theta = (93.4 \pm 0.8)^\circ$ . The result is plotted as a red solid line in Fig. 6.3 c, which compares very well to the measured data and confirms the validity of the analytical expressions for sideways deflection (Eqs. 6.1 and 6.2). Using  $\Delta\theta$ , we compare the measured tilt parameters  $\delta t/\delta y$  (blue dots) to  $\Delta T/\Delta Y$  via Eq. 6.5 (blue solid line). We observe a good agreement; deviations at larger angles are attributed to residual shifts of the temporal focus by nonconstant  $\Delta p_z(\theta_e, \theta_{\text{THz}})$ , which is neglected here (see Fig. 6.2 c, dotted line). The agreement of the measured tilt data to the theory shows that tilted electron pulses are generated as predicted by Eq. 6.6.

The two separate experiments on tilt and deflection (blue and red data in Fig. 6.3 c, respectively) reveal a nontrivial coincidence between the velocity-matching condition and absent deflection. Both data traces cross zero at the same angle  $\theta_e^0$ , which happens to be the velocity-matching angle according to Eq. 6.4. It follows that planar elements, if oriented according to Eq. 6.4, allow compressing electron pulses of arbitrarily large beam diameter by means of all-optical control without any unwanted time-dependent deflections.

Furthermore, we see from Fig. 6.3 c that the measured pulse front tilt appears to be linked to the measured deflection strength: larger tilt angles imply stronger sideways effects. In optics, there is a direct relationship between pulse front tilt and angular dispersion via  $\tan \alpha = \bar{\lambda} d\varepsilon/d\lambda$  [211], where  $\alpha$  is the pulse front tilt,  $\bar{\lambda}$  is the spectral mean, and  $d\varepsilon/d\lambda$  is the angular dispersion (change of deflection angle  $\varepsilon$  per wavelength  $\lambda$ ). Our two experiments reveal a similar relation for electrons. We define the angular electron dispersion analogously to the optical case as  $d\varepsilon/d\lambda_{\text{db}}$ , where  $\varepsilon$  is the electron deflection angle (Fig. 6.3 b) and  $\lambda_{\text{db}} \approx h/p_z$  is the electron de Broglie wavelength. In order to evaluate  $d\varepsilon/d\lambda_{\text{db}}$  from the data, we assume  $p_y \ll p_z$  (paraxial approximation) and constant angular dispersion. Differentiating  $\varepsilon = p_y/p_z$  and  $\lambda_{\text{db}}$  yields  $d\varepsilon = (1/p_z)[dp_y - (p_y/p_z)dp_z]$ ,  $d\lambda_{\text{db}} = -(\lambda_{\text{db}}/p_z)dp_z$ , and  $d\varepsilon/d\lambda_{\text{db}} = -(1/\lambda_{\text{db}})[(dp_y/dp_z) - (p_y/p_z)]$ . For  $\lambda_{\text{db}} = \lambda_{\text{db}}^0$ , where  $\lambda_{\text{db}}^0$  is the initial de Broglie wavelength of the not-deflected electron ( $\varepsilon = 0$ ), we obtain  $-\lambda_{\text{db}}^0(d\varepsilon/d\lambda_{\text{db}}) =$

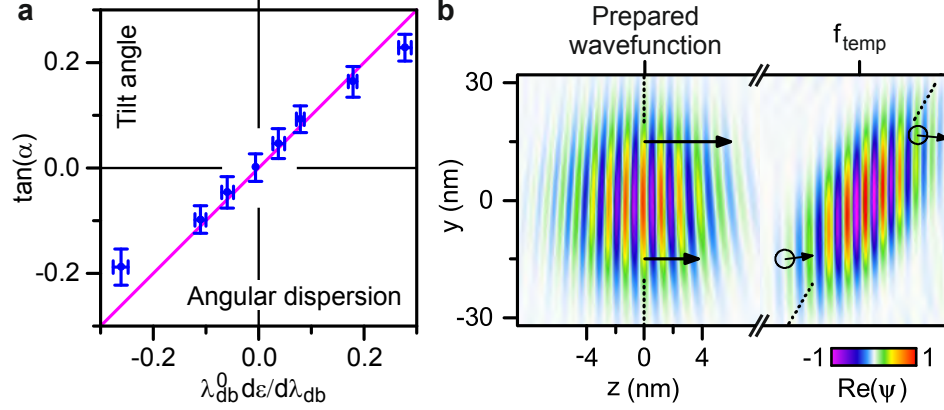


**Figure 6.4:** Pulse front tilt vs angular dispersion for electrons, and quantum simulations. (a) Measured angular dispersion in electron pulses as a function of tilt angle (blue) in comparison to this Letter’s conjecture (Eq. 6.7, magenta). Error bars indicate one standard deviation and are omitted when smaller than a data point. Unequal scanning ranges of the raw data (Fig. 6.3 c) are accounted for by linear interpolation. (b) Quantum simulation of an electron wave packet  $\psi(z, y, t)$  with initial position-momentum correlation (left) propagated to the temporal focus  $f_{\text{temp}}$  (right). We assume a coherence time of 8 fs, a beam waist of 20 nm, and a linear transverse change of forward momentum, as from the experiment (black arrows). The electron energy is 1 eV in order to make the de Broglie wavelength visible in the results. The phase fronts remain approximately perpendicular to the propagation direction, but the envelope becomes tilted. Angular dispersion is indicated by the black circles and constant throughout the simulation.

$\Delta p_y/\Delta p_z = [A_y(\theta_e, \theta_{\text{THz}})/A_z(\theta_e, \theta_{\text{THz}})]$ ,  $A_y$  is obtained from the measured deflection amplitude (red dots in Fig. 6.3 c), and  $A_z$  is calculated via Eq. 6.3 by using  $\Delta\theta$  and  $C$  from the calibration of the setup.

The result of this conversion is reported in Fig. 6.4 a, where we plot  $\lambda_{\text{db}}^0(d\varepsilon/d\lambda_{\text{db}})$  (evaluated angular dispersion) against  $\tan \alpha$  (measured tilt strength). We see that all data points are close to a straight line with a slope of unity (magenta). This experimental finding motivates the conjecture

$$\tan \alpha = \lambda_{\text{db}}^0 \frac{d\varepsilon}{d\lambda_{\text{db}}} \quad (6.7)$$

for electron pulses in a temporal focus, where all energy components overlap in space and time. Equation 6.7 is the matter wave analog to its optical counterpart [211].

In contrast to laser pulses, our electron pulses in the experiment have a  $10^5$  times shorter wavelength, a rest mass, and sublight speed. The beam is also rather incoherent and the electrons behave almost like point particles due to their low degree of coherence of  $\sim 10^{-4}$  in space and  $\sim 10^{-2}$  in time [116]. Furthermore, our way of generating tilted electron pulses is different from the optical approach, namely, by applying a position-dependent acceleration or deceleration instead of using a passive

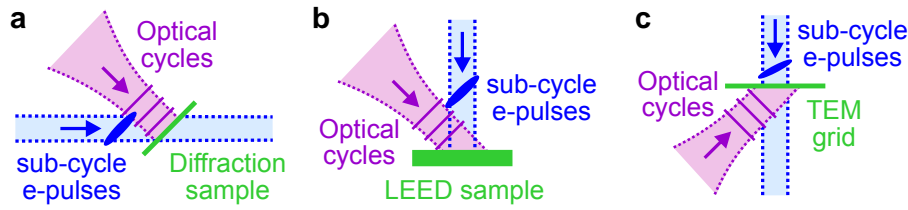


**Figure 6.5:** Potential applications of tilted electron pulses. (a) Subcycle/attosecond electron diffraction [44]. A crystalline sample (green) is oriented along a zone axis for generating multiple Bragg spots. The laser phase front (violet) has a polarization along the crystal surface. Tilted electron pulses (blue) propagate with sublight speed, but probe the sample in synchrony with the field cycles. (b) Subcycle low-energy electron diffraction (LEED). Laser cycles (violet) illuminate a sample material (green) at an angle due to practical space restrictions [214]. Tilted electron pulses (blue) can probe every part of the surface with the same delay with respect to the field cycles. (c) Subcycle electron microscopy. A transmission electron microscopy grid (TEM grid) can usually not be tilted a lot with respect to the twin lens in a high-resolution microscope. Nevertheless, a combination of tilted electron pulses (blue) and diagonal laser incidence (violet) can provide a uniform subcycle-level delay over the entire illuminated TEM grid area.

dispersive element like a prism or a grating. The fact that there is nevertheless an apparent connection between tilt and dispersion in the experiment (see Fig. 6.4 a) suggests that Eq. 6.7 might be general for any type of matter wave at arbitrary degree of coherence.

A simulation of a fully coherent electron wave packet with a transverse momentum modulation is depicted in Fig. 6.4 b, motivated by recent experimental advances in laser-triggered high-coherence electron sources [107]. We assume an initial electron wave function  $\psi(y, z) = \exp[-z^2/(2z_0^2) - y^2/(2y_0^2) + i(k_0 + c_y y)z + ic_z z^2]$ , where  $z_0$  is the pulse length,  $y_0$  is the wave packet width,  $k_0$  is the mean wave vector,  $c_z$  is the chirp coefficient, and  $c_y$  is a  $y$ -dependent longitudinal momentum change. Free-space propagation in a nonrelativistic approximation is calculated via Fourier transformation, multiplication with the propagator  $\exp[i\hbar k^2 t/(2m_e)]$ , and backtransformation;  $t$  is the propagation time and  $k$  is the electron wave vector. We see (Fig. 6.4 b) that the phase fronts are angled to the pulse shape, and different wavelengths travel at different angles (black circles). These simulations support Eq. 6.7 for the case of fully coherent electron wave packets.

In conclusion, our results show that tilted and compressed electron pulses can efficiently be generated by all-optical means and simple interaction elements. Tilted electron pulses allow for ultrafast pump-probe diffraction and microscopy in which the optical cycles are used for sample excitation or control (see Fig. 6.5). In experiments where the electron pulses are longer than an optical period [77, 44, 43, 45], the energy sidebands [77, 82] will be coupled to the deflection angles [89, 44], po-

tentially enabling novel imaging concepts in electron microscopy [77, 99]. Tailored optical control fields or more complex interaction elements [95] provide opportunity for complex phase-space manipulations to create exotic beams and pulse shapes at target. We predict that the controlled generation of such electron pulses will enable a wide range of future applications in probing and controlling materials, possibly along with electron vortices and Airy or Bessel beams [215–218].

### **Acknowledgments**

This work was supported by the European Research Council, the Munich-Centre for Advanced Photonics. We thank Ferenc Krausz for support and Kathrin Mohler for discussions.

# Terahertz compression of electron pulses at a planar mirror membrane

The present chapter concludes this thesis' series of terahertz-based electron pulse control and metrology experiments. Here, the knowledge gathered from the previous experiments is applied to achieve compressed electron pulses as short as 12 fs (rms), which are among the shortest and most stable electron pulses reported to date.

## 7.1 Preface

One of the main motivations of this thesis is to obtain shortest possible electron pulses, which can be used for the study of time-dependent processes in diffraction and microscopy samples on their intrinsic length and time scales (see Chapter 1). To this end, pulse compression with optically generated terahertz pulses provides a promising route, because of their intrinsic synchronization to the driving laser source and their comparably long cycle duration ( $\sim$  ps).

The here presented, record-short electron pulses are made possible by three essential elements: (i) the use of a thin metallic foil for electron pulse compression, which allows for velocity-matching and avoids time-dependent deflection (see Chapter 6) instead of bow-tie resonators, (ii) a state-of-the-art, flat-photocathode electron source with high acceleration fields [115] to keep the initial pulse duration low and (iii) a dedicated optical design avoiding timing variations caused by pointing fluctuations of the terahertz pump beam (see Chapter 3).

Furthermore, this chapter gives background information on how to achieve these and potentially even shorter electron pulses. Simulations of particle dynamics shown in this chapter (Fig. 7.4) open a path towards isolated attosecond electron pulses. Key parameters to this end are a higher kinetic electron energy ( $> 100$  keV), a reduced

electron energy spread ( $< 1$  eV), and a shorter temporal focal distance ( $< 10$  cm) by virtue of higher terahertz field strengths ( $> 10^6$  V/m). All of these parameters are realistically achievable and render electron pulses of few-femtosecond duration and below more than feasible.

In this chapter, we go step by step through the essential parts of the experiment. The reduced complexity of the experiments described in here should allow readers to get a comprehensive overview of the capabilities of terahertz-based electron pulse compression. We start with the electron source and the care that is taken to ensure a stable and arc-free operation. We then turn to the compression element, that is the electron-transmitting and terahertz-reflecting mirror which has already been used in the experiments in Chapter 6. In this context, the measured modulation strength as a function the thickness of the aluminum layer (Fig. 7.1 b) is of utter importance. It allows the reduction the inelastic scattering losses of the electron pulse passing through the foil by choosing the minimum possible thickness. Intriguingly, a only 10-nm thick layer is enough for this purpose and can possibly even be made thinner than that.<sup>1</sup>

The basic compression concept is laid out briefly here (see also Fig. 7.1 a and c), but is described in great detail in Chapter 2. The overall setup is still similar to the one described in Chapters 4–6. Also the streaking concept to determine the pulse duration and arrival time jitter, which is only touched here, is basically as first description in Chapter 4. Because the shortest pulses measured here exhibit a pulse duration close to the limit of the streaking resolution, a convolution fit procedure [65] was performed as described in this chapter (see Fig. 7.3).

One novel element added here to the basic setup of the previous chapters, is a pair of deflection plates, inserted behind the streaking resonator. They are used to deflect the electron beam perpendicular to the streaking axis. This previously unused dimension is exploited for determination of arrival time fluctuations on a timescale below the detector exposure time of  $\sim 1$  s (Fig. 7.3) and for the investigation of systematic effects resulting from the AC-frequency of the laboratory power lines of 50 Hz (Fig. 7.3 c).

In the course of this thesis, the here described pulse compression study has been conceived and realized. The electron beam line (Chapters 4–6) as well as the terahertz generation scheme (Chapter 3) has been improved for stability and robustness. Deflection plates for extended streaking methodology and temporal jitter characterization have been designed and added to the beamline. Simulations to capture the longitudinal phase space dynamics (see also Chapter 2) have been conducted and found to yield good agreement with reasonable experimental parameters. Those

---

<sup>1</sup>Metallic foils are in general expected to be superior to dielectric substrates for pulse modulation with low frequencies, i.e. in the terahertz range [100].

simulations are then used to predict the dependence of the compressed pulse duration on electron energy and temporal focusing distance and show a way to produce few-to-sub-femtosecond pulses in this scheme.

These results have been published in *Physical Review Applied* (vol. 11, p. 024034) in 2019.<sup>2</sup> The following text is a reprint of the original publication [105].

---

<sup>2</sup>Author contributions: Electron pulse compression and streaking experiments by DE and KJM under supervision of PB. Modulation strength measurements, data evaluation and simulations by DE. Optical setup and modifications to the electron beam line by DE, KJM and TV. Electron source design and implementation by LW, TV and RE in discussion with DE, KM and PB. All authors interpreted the results and contributed to the writing of the manuscript based on a first draft by DE.



# Terahertz compression of electron pulses at a planar mirror membrane

Dominik Ehberger, Kathrin J. Mohler, Thomas Vasileiadis, Ralph Ernstorfer, Lutz Waldecker, Peter Baum

## Abstract

Compression of electron pulses with terahertz radiation offers short pulse durations and intrinsic sub-cycle stability in time. Here we report the generation of 12-fs (rms), 28-fs (FWHM) electron pulses at a kinetic energy of 75 keV by using single-cycle terahertz radiation and a simple planar mirror. The mirror interface provides transverse velocity matching and spatially uniform compression in time with purely longitudinal field-electron interaction. The measured short-term and long-term temporal drifts are substantially below the pulse duration without any active synchronization. A simple phase-space model explains the measured temporal focusing dynamics for different compressor strengths and shows a path toward generating isolated attosecond electron pulses from beams of almost arbitrary transverse emittance.

© 2018 Author(s). Reprinted under the terms of the [Creative Commons Attribution 4.0 International](#) license.

[doi:10.1103/PhysRevApplied.11.024034](https://doi.org/10.1103/PhysRevApplied.11.024034)

## 7.2.1 Introduction

Robust and reliable methods for generating femtosecond and attosecond electron pulses are key to studying atomic and electronic processes in matter on their fundamental length and time scales. Ultrafast electron microscopy and diffraction [31, 33] allow for observing ultrafast processes on femtosecond and subnanometer levels. The techniques have already elucidated numerous ultrafast solid-state phenomena on subpicosecond time scales [34, 8, 40, 42], and subfemtosecond phenomena await investigation [48, 28]. Proof-of-principle diffraction and microscopy with electron-pulse trains [44] indicate the practicability of this attosecond-Angstrom regime.

For pump-probe geometries with isolated pulses, time resolution is limited by the duration of the electron pulses and their stability in time with respect to the optical excitation. Recent approaches for electron-pulse compression and metrology use terahertz single-cycle pulses [89, 95] instead of microwave radiation [57, 63, 61,

[64]. This concept largely circumvents temporal synchronization issues because an entire experiment can be operated in an all-optical way by a single laser source. In addition, terahertz radiation has been used for acceleration [90, 95], streaking and deflection [89, 95], focusing [95] and tilting [104] of electron pulses. There is also growing interest in applying terahertz techniques for the modulation of relativistic electron beams [96–98]. Waveguides or resonant structures are usually applied for mediating the terahertz-electron interaction. Although such structures can provide field enhancement and phase-matched propagation, their size limits the maximum acceptable electron-beam diameter. Therefore, it has been difficult to compress the rather large and high-emittance electron beams of table-top experiments or linear electron accelerators down to few-femtoseconds duration.

We demonstrate the use of a simple planar membrane mirror in combination with a high-acceleration electron source for terahertz-based electron-pulse compression. The mirror provides transverse phase matching over an almost arbitrarily large electron beam size and the laser-triggered high-field electron source minimizes the effects of nonlinearities in the time domain. In the experiment, we compress few-electron pulses from a simple planar photocathode to durations of 12 fs (rms) or 28 fs (FWHM). These values are on par with state-of-the-art microwave compression techniques [64, 65], but without the need for active synchronization [66, 67].

### 7.2.2 Concept and experimental setup

Figure 7.1 a depicts the experimental setup. Electron pulses are emitted from a gold-coated photocathode by the second harmonic of 270-fs-long laser pulses from a Yb:YAG laser (Pharos, Light Conversion Inc.) at a repetition rate of 50 kHz. The electron source is of compact design, featuring a high electrostatic acceleration field close to the breakdown limit [115]. Carefully polished gun parts and a gap-free contact between the sapphire cathode and the metal construction ensure stable gun operation without field emission or arcing. The electron pulses are accelerated to a kinetic energy of 75 keV over a distance of 11 mm. The laser spot size on the cathode is roughly 5  $\mu\text{m}$  (FWHM). To avoid space-charge effects, we reduce the average number of emitted electrons per pulse to approximately 3. The temporal shape of such a few-electrons pulse and its duration are understood as the probability distribution of the individual electron's arrival time at a certain position [116]. It is obtained from averaging over repetitive measurements. The electron-pulse duration at a distance of 0.9 m behind the gun is 490 fs (FWHM), measured by terahertz streaking [89]. A magnetic solenoid lens is placed 12 cm after the gun exit and aligned collinearly to the beam axis [200]. Terahertz single-cycle pulses for compression and subsequent streaking metrology are generated at a central frequency of 0.4 THz in two separate

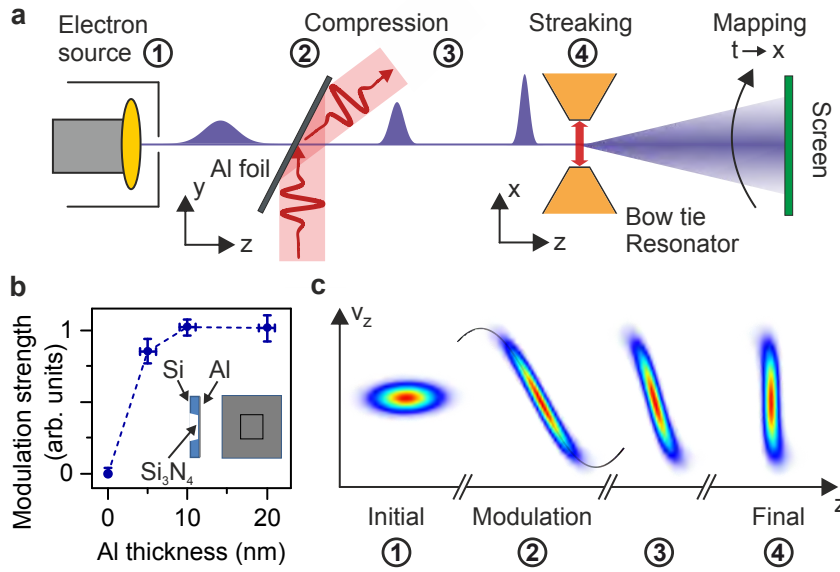


**Figure 7.1:** Concept and experimental setup. (a) Schematic of the electron compression scheme based on an electron-transparent planar terahertz mirror. An initial electron pulse (1) emitted from the electron source propagates to the mirror, where it interacts with the terahertz wave (2) and compresses in time upon propagation (3). Streaking (4) allows for retrieval of the electron pulse duration as it maps electron arrival times ( $t$ ) onto positions on the screen ( $x$ ). For the 50- $\mu\text{m}$  aperture (see text), the electron beam diameters at the compression mirror, bow-tie resonator and screen are approximately 1 mm,  $< 30\ \mu\text{m}$  and approximately  $150\ \mu\text{m}$ , respectively. (b) Measured modulation strength at the terahertz compressor for different aluminum layer thicknesses. Inset: Schematic of the mirror element. (c) Phase space representation of the stages of electron pulse compression (1-4) at terahertz frequencies. The black line indicates the terahertz-induced velocity gain along the electron pulse's longitudinal profile.

LiNbO<sub>3</sub> slabs with silicon prisms as output couplers [102]. Pump powers of approximately 3 W and 12 W are needed for compression and streaking, respectively.

Compression of the electron pulses is enabled by intersecting the electron beam with one of the two terahertz beams at approximately 90° on an ultrathin aluminum mirror membrane located 0.4 m behind the electron source (see Fig. 7.1 a). The mirror is thin enough to transmit the electron beam, but thick enough to efficiently reflect the terahertz radiation. To find the best mirror for our experiment, we measure the amplitude of the terahertz-induced, time-dependent electron-pulse deflection of four different mirror membranes. Figure 7.1 b depicts the relative strength of the interaction as a function of aluminum layer thickness. The strength of the deflection is proportional to the amount of longitudinal acceleration or deceleration [104]. We find that an aluminum layer as thin as 5–10 nm is sufficient, although it is  $> 10^4$  times thinner than a terahertz wavelength. This observation is in agreement with conductivity measurements of thin aluminum films at terahertz frequencies [213].

Simulations show that single atomic layers such as graphene might also be applicable [100]. In the experiment, the 10-nm thick aluminum layer is supported by a freestanding, 10-nm thick  $\text{Si}_3\text{N}_4$  membrane for mechanical stability (see inset of Fig. 7.1 b). The useful aperture is  $1.5 \times 1.5\text{mm}^2$  and the electron transmission for perpendicular incidence is approximately 0.7.

At a distance of 0.5 m after the compression stage, the electron pulses are characterized in time by terahertz streaking [89] at a collinearly excited bow-tie-shaped terahertz resonator with a clear aperture of 80  $\mu\text{m}$ . We use the magnetic lens to focus through the compression element and through the bow-tie resonator via an intermediate beam waist in front of the screen. There are no electro-optical elements between the compression and the streaking stage in order to avoid potential temporal distortions [199]. Different apertures of 25–50  $\mu\text{m}$  in diameter in front of the bow-tie resonator allow us to trade signal intensity for temporal-streaking resolution.

Figure 7.1 c depicts the compression dynamics in longitudinal phase space. The trailing part of an initial electron pulse is accelerated and its leading part is decelerated, while the mean velocity is left unaltered. The initially trailing parts catch up with the previously leading parts of the pulse at a location of the shortest pulse duration called the temporal focus. If the incoming electron pulse is shorter than half a modulation cycle, we obtain a single, isolated time-compressed pulse [89]. Our planar mirror provides the required, time-dependent electron momentum modulation by letting the electrons abruptly enter the electromagnetic field within a time much shorter than a cycle period [81, 82]. The final net momentum kick  $\Delta p$  is given by the time-integrated Lorentz force acting on the particle until the terahertz field has passed. For a p-polarized plane wave of peak electric field strength  $E_0$  and optical angular frequency  $\omega$ , an analytic derivation yields  $\Delta p \propto E_0 \sin(\omega t)/\omega$ , where  $t$  is the electron arrival time at the mirror relative to the crest of the wave; the proportionality constant depends on the electron and optical incidence angle [104]. A cosine-shaped terahertz pulse (carrier envelope phase equal to zero) is, therefore, required for efficient electron-pulse compression. It provides a sine-like momentum modulation that is approximately linear around its zero crossing [104]. To this end, we convert the sine-like terahertz pulses emerging from the  $\text{LiNbO}_3$  crystal (carrier envelope phase near  $\pm\pi/2$ ) into cosine-shaped pulses at the compression element by accurately adjusting the focusing conditions and in particular the Gouy phase. The size of the terahertz beam waist at the mirror is 2.8 mm (FWHM), which is considerably larger than the electron beam. The terahertz phase fronts are, therefore, approximately planar in the region overlapping with the electrons.

Realistic electron beams have a finite emittance and hence a finite beam diameter, for example, approximately 1 mm at the compressor stage in our experiment. It is, therefore, necessary to consider the compression dynamics as a function of

the transverse coordinate. For planar elements, there is a certain combination of electron incidence angle  $\theta_e$  and terahertz incidence angle  $\theta_{\text{THz}}$  for which momentum modulation and hence compression is independent of the spatial electron-beam profile. This configuration is called the (transverse) velocity-matching condition [82], namely,  $c/\sin\theta_{\text{THz}} = v_e/\sin\theta_e$ , where  $v_e$  is the electron velocity and  $c$  is the speed of light [104]. At these angles, the phase velocity of the terahertz pulses matches the velocity of the electron incidence along the mirror surface. This velocity-matching condition coincides with the absence of time-dependent transverse momentum transfer, and thus the net modulation is purely longitudinal and spatially homogeneous [104]. The entire electron beam is, therefore, compressed into isolated, short, and non-tilted electron pulses at the temporal focus. We note that a similar condition of spatially homogeneous interaction cannot be found for sideways deflection because net transverse momentum changes are absent in a velocity-matched mirror configuration [104]. The planar membrane is, therefore, ideal for electron-pulse compression while a microstructured resonator is ideal for their temporal analysis.

### 7.2.3 Results on pulse compression

In the experiment, we first adjust the timing of electron and terahertz pulses at the compression and streaking stages to zero crossings of the modulation [89]. We then vary the field strength at the compression mirror until the shortest electron pulses are observed at the streaking stage. Figure 7.2a depicts the measured streaking profiles as a function of compressor field strength. Temporal focusing is evident by the formation of a waist of the pulse duration for the optimum compression strength (peak field of approximately  $3 \times 10^5$  V/m). We observe that the temporal pulse profile is different when the electron pulses are under compressed (relative field strength  $< 1$ ) as compared to over compression (relative field strength  $> 1$ ), where a double-peak structure emerges. This effect has been observed before [89, 95] and is a direct consequence of the remaining temporal nonlinearities of the compression field [59]. At highest compression strength, these two peaks also have slightly different intensities because the curvature of the terahertz-modulation cycle is slightly different before and after the zero crossing. There is also a small background intensity for positive times in Fig. 7.2a, which is reproducible and a consequence of electron energy loss due to inelastic scattering at the membrane mirror [103].

Figure 7.2b shows the results of a Monte Carlo simulation in the longitudinal domain (compare Fig. 7.1c) with  $10^7$  point particles per simulated compression strength. Electron-electron interactions are neglected and terahertz-induced momentum transfer is much smaller than the central electron momentum. The initial electron pulse is assumed to be uncorrelated in energy and time which neglects the

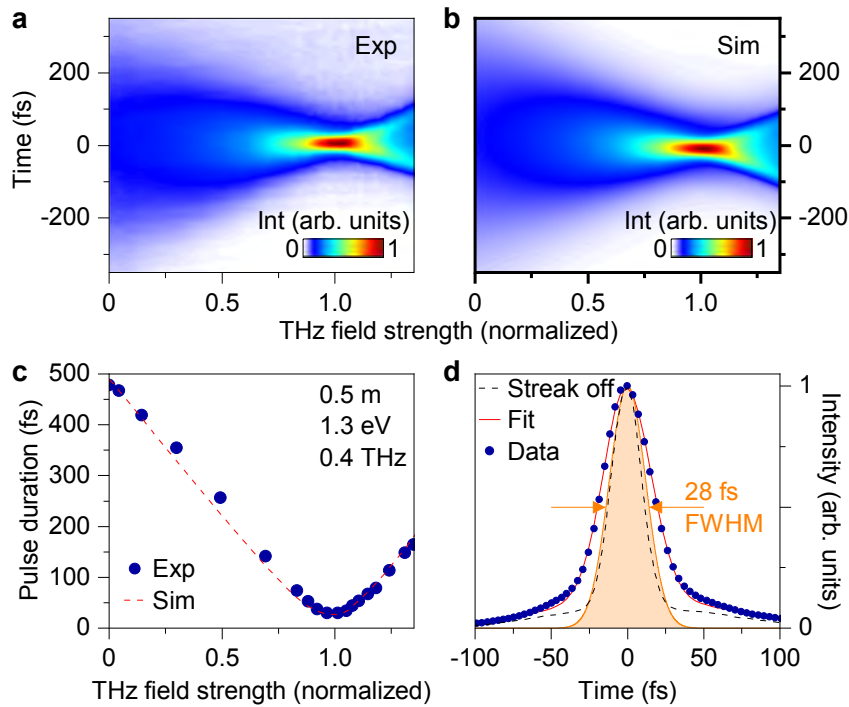


**Figure 7.2:** Experimental results and simulation. (a) Measured streaking profiles as a function of the normalized compressor field strength (unity approximately corresponds to  $3 \times 10^5$  V/m). The electron pulses first become shorter in time, reach a minimum pulse duration and then become again longer for highest field strengths. (b) Simulated streaking profiles assuming an energy spread of 1.3 eV, initial pulse duration of 490 fs, compression-streaking distance of 0.5 m, modulation with 0.4 THz and phase offset of 80 mrad. (c) Measured (blue dots) and simulated (dashed line) electron pulse durations (FWHM). For visibility, only every other data point is shown. (d) Shortest measured electron pulse. The averaged streaking profile (blue dots) is fitted by convoluting the unstreaked profile (dashed line) with a Gaussian pulse. The best fit (red line) is obtained for a pulse duration of 28.3 fs (FWHM) or 12.0 fs (rms).

dynamics of acceleration within the gun [123]. We find that an initial pulse duration of 490 fs (FWHM), a modulation frequency of 0.4 THz and an energy width of 1.3 eV (FWHM) yield the best overall agreement with our measured data (compare with Fig. 7.2 a). The energy spread of 1.3 eV may be caused by a work-function mismatch [110], inhomogeneous emission sites, inelastic scattering at the Al/SiN membrane, or fluctuations of the acceleration voltage.

In Fig. 7.2 c, we plot the measured pulse duration (blue dots) with increasing compressor field strength, compared to the simulation results (red dashed line). As expected, the pulses first compress and later overcompress as a function of the applied field strength, which agrees very well with the simulated pulse durations. The electron pulses are shortened in time by a factor of approximately 17. Figure 7.2 d reports the electron-pulse shape and duration at the best compression strength. The blue dots show the measured streaking profile. It is narrow, but shows a non-Gaussian shape and asymmetric wings. These wings are also present in the compressed but nonstreaked electron-beam profile (dashed line) and caused by elastic and inelastic electron scattering in the Al foil of the compressor; they can, in principle, be minimized by appropriate aperture and imaging settings. In general, the measured streaking profile is a convolution of the actual temporal profile of the electron pulses and the transverse beam profile. To retrieve the electron-pulse duration, we employ an evaluation that was also used by Maxson et al. [65]. We fit the data points (blue) with a convolution of an assumed Gaussian temporal shape for the electron pulses with the measured transverse electron-beam profile (black dashed line). The fitting curve (red line in Fig. 7.2 d) closely matches the experiment (blue dots). The retrieved electron-pulse profile plotted in orange has a duration of  $(28.3 \pm 0.5)$  fs (FWHM) or  $(12.0 \pm 0.2)$  fs (rms). Alternatively, deconvolution using a Wiener filter yields approximately 25 fs (FWHM). A second experiment with a 25- $\mu\text{m}$  instead of 50- $\mu\text{m}$  beam-limiting aperture in the streaking setup yields the exact same fit result of 12.0 fs (rms). This observation indicates that the electron pulses are compressed independently of the beam size, as expected from the velocity-matched mirror configuration.

#### 7.2.4 Timing stability

A central benefit of all-optical terahertz compression as compared to microwave approaches is the expected passive stability in time [89]. Here, we report a jitter and drift characterization over three typical time scales. Figure 7.3 a shows the long-term drifts  $\Delta T$  derived from repetitively acquired streaking traces and their center positions on the screen for the best pulse-compression settings. Each data point is averaged for 20 s. We measure a standard deviation of 3.7 fs without observing sys-

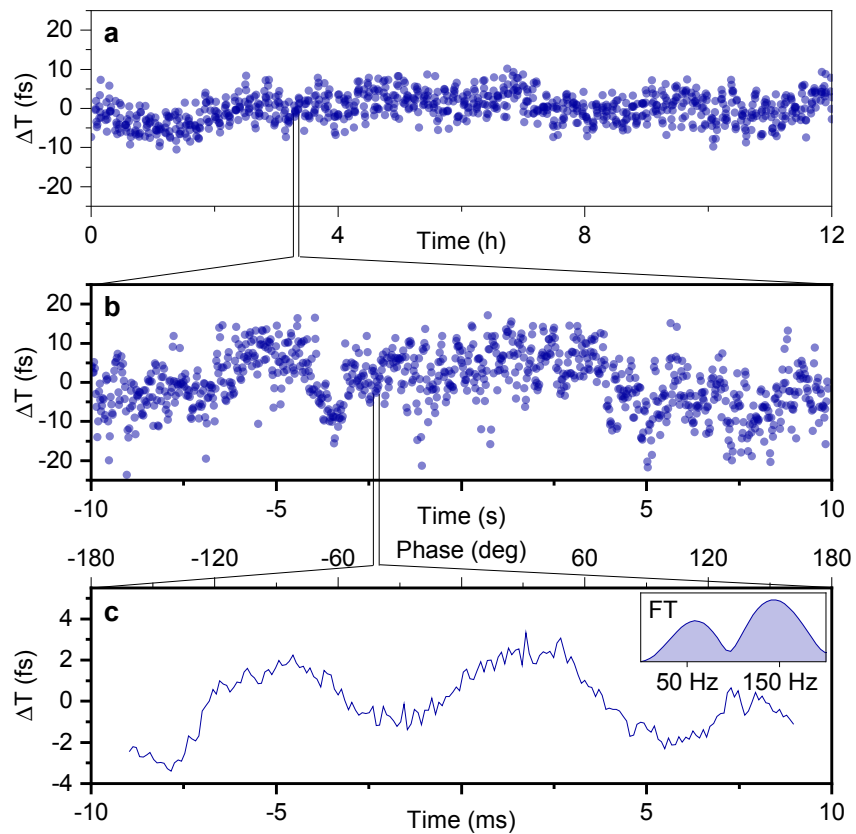


**Figure 7.3:** Timing stability. (a) Long-term fluctuations amount to 3.7 fs (rms). (b) Short-term jitter is 7.5 fs (rms) on average. (c) Systematical timing error locked to 50 Hz. Inset: Fourier analysis (FT).

tematic timing drifts over 12 h. This result is obtained without employing any kind of active timing stabilization. Faster fluctuations are measured with the help of electronically driven capacitor plates behind the streaking resonator that deflect the electron beam perpendicularly to the streaking axis, that is, along the  $y$  axis (see Fig. 7.1 a). This instrumentation allows us to measure timing fluctuations with millisecond resolution, limited mainly by the average electron current. Figure 7.3 b shows a typical 20-s trace with each data point averaged over 21 ms. The mean standard deviation of all 894 recorded 20-s traces is 7.5 fs. The accumulated stability over the course of 12 hours is 8.4 fs (rms). Locking the capacitor plates to the 50-Hz laboratory mains reveals systematic timing jitter on millisecond timescales. Figure 7.3 c shows the result, averaged over  $\sim 10^6$  50-Hz cycles. We see a periodic modulation with an amplitude of  $< 2$  fs and with Fourier components at 50 Hz and 150 Hz (Fig. 7.3 c, inset). We attribute the remaining timing fluctuations to pointing variations of the terahertz-pump beams and/or high-voltage instabilities of the electron acceleration. All of the measured timing fluctuations are clearly below the pulse duration. The reported mirror-based terahertz compression concept thus enables low-dose, few-electrons diffraction [112] and microscopy [31] at highest temporal resolution, even for measuring times of several hours.

### 7.2.5 Discussion

The compressed electron pulses are 2–3 times shorter than those achieved with terahertz compression at bow-tie resonators [89] or other more elaborate interaction elements [95]. The advancement by a factor of 2–3 over our previous results [89, 104] is a consequence of the dedicated mirror design with highest electron transmission and lowest electron energy losses combined with a substantially improved electron source [115].

The mirror compressor concept offers a clear perspective to enter the subfemtosecond regime with isolated electron pulses instead of pulse trains [43–45]. We first consider the potential influence of temporal nonlinearities of the compressing THz cycle. Figure 7.4 a shows a simulation of compressed electron-pulse profiles obtained by the phase-space model when changing the electron-pulse durations at the compressor. Longer pulses result in stronger deviations from a Gaussian shape, caused by temporal nonlinearities of the terahertz modulation. Nevertheless, the FWHM pulse duration is hardly affected and only the peak electron current decreases while the background comes up. The final pulse duration in the modeled experimental geometry is rather dominated by the initial energy spread. Therefore, we next consider the influence of kinetic energy and bandwidth of the photoemission process on the compressed electron-pulse duration.

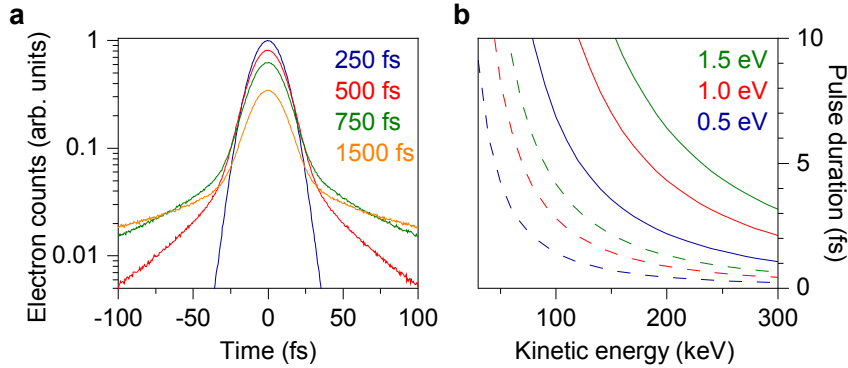


**Figure 7.4:** Simulated electron pulse shapes and durations. (a) Compressed electron pulse profiles for different incoming electron pulse durations (FWHM) at the compressor, assuming 0.4 THz central modulation frequency. For longer electron pulses incident on the compression element, shoulders emerge in the temporal profile due to temporal nonlinearities of the modulation. (b) Compressed electron pulse duration (FWHM) as a function of kinetic energy of the incoming electron pulses for different energy spreads. The initial electron pulse duration is 490 fs. Solid lines, compression-streaking distance of 0.5 m; dashed lines, compression-streaking distance of 0.1 m.

Figure 7.4 b shows compressed pulse durations for different uncorrelated electron-energy spreads as a function of kinetic energy. We simulate two different compressor-streaking distances while keeping the initial pulse duration fixed to 490 fs. For a photocathode bandwidth of 0.5 eV [110,107], the model predicts a final pulse duration of approximately 10 fs (FWHM) for the reported experimental configuration (blue solid line). Higher electron energies are also beneficial. Shortening the temporal focus distance from 50 cm to 10 cm at electron energies of 100–200 keV breaks the 1-fs barrier. The required terahertz field strength on the order of  $3 \times 10^6$  V/m [104] for this case is realistically achievable [95]. We note that phase-space correlations due to acceleration in the electron gun are neglected in our model, and the above results are, therefore, the upper limits. In a multistage compressor as outlined in Ref. [89], the terahertz-driven planar mirror could serve to inject subcycle electron pulses into a higher-frequency compression stage [43–45]. The final pulse duration in such a multistage compressor is expected to be largely independent of residual jitter in the terahertz stage [45].

In summary, terahertz compression of electron pulses with the help of a planar mirror membrane is insensitive to electron-beam-size effects and provides a uniform, passively stable, and purely longitudinal momentum modulation. A state-of-the-art electron source minimizes temporal nonlinearities and reduces background in the temporal pulse profile. The generated electron pulses with their sub-30-fs duration (FWHM) should be directly suitable for pump-probe investigations of fastest atomic

and electron motion, for example, fundamental phonon modes [49, 50] or metamaterial dynamics [99].

## Acknowledgments

This work was supported by the European Research Council (ERC) under the European Union's Horizon 2020 research and innovation program (Grant Agreements No. 647771 and No. ERC-2015-CoG-682843), the Munich Centre of Advanced Photonics (MAP), the International Max Planck Research School for Advanced Photon Science (IMPRS-APS) and the Max Planck Society. LW acknowledges support by the Alexander von Humboldt foundation. We would like to thank Ann-Kathrin Raab, Sonja Tauchert, Johannes Thurner, and Maxim Tsarev for assistance with electron beam-line components.



## Conclusions and outlook

In the course of this thesis, manifold ways to manipulate electron pulses in an all-optical fashion by virtue of single cycle terahertz fields have been explored. Now at the end of this work, let us recap the insights we gained.

In Chapter 1, we began with the statement that in order to obtain deeper insight into the properties of matter and materials, we need to understand those from a microscopic point of view. We identified ultrafast electron diffraction as a promising approach to resolve atomic and electronic dynamics on their intrinsic length and time scales, that is, from angstroms to picometers, from femtoseconds to attoseconds. Because of the short de Broglie wavelength of massive particles, diffraction with keV electron pulses offers high spatial resolution. However, it is also their mass which lets electrons in a pulse quickly disperse in time, as electrons of higher energy move faster through vacuum than those of lower energy and which therefore limits the temporal resolution of ultrafast electron diffraction to on the order of 100 fs. Preparing an electron pulse where the particles of lower energy are in the leading part of the pulse, ahead of the high energy electrons, will in turn lead to a compression of the pulse. Such a phase-space inversion can be achieved by using temporal lenses, which, by adding energy spread to the electron pulse, in principle allows for the formation of almost arbitrarily short pulses.

In Chapter 2 we investigated the dispersion dynamics of ultrashort electron pulses from theoretical standpoint and their manipulation by means of temporal lenses. These considerations led us to the derivation of an imaging equation for temporal lenses as the temporal analogue to the optical imaging equation for Gaussian beams. This previously unknown relation largely simplifies the analysis of temporal lens systems and provides an intuitive approach to understanding the properties of electron pulse compression from optical concepts. Its capabilities were highlighted by the theoretical investigation of two proposed, but yet-to-be realized applications, namely (i) a two-stage electron pulse compressor, which is able to produce isolated

attosecond electron pulses and conceptually minimizes timing jitter, and (ii) a dynamic monochromator, which reduces the energy bandwidth of electron pulses in trade-off for pulse duration.

Temporal lenses require time-varying electromagnetic fields. In search for an alternative to the conventional, but jitter-susceptible microwave approach, we found terahertz radiation as an ideal choice for femtosecond electron pulse manipulation. It combines the advantage of inherent laser synchronization and long cycle duration. Using a simple LiNbO<sub>3</sub> slab with a silicon prism as output coupler, we found a reliable and simple method to convert near-IR pump pulses to intense single-cycle terahertz pulses (Chapter 3), investigated its performance with respect to efficiency, spectrum and heat removal and gave formulas to calculate the optimum focusing parameters.

With those optimized terahertz pulses we moved on to demonstrate how to use them to manipulate electron pulses. We saw that we can compress and streak them with specially designed terahertz resonators and by doing so transferred well-established microwave control concepts to the optical domain (Chapter 4). From a proof-of-principle experiment we learned to use the compression-and-streaking scheme for measurement of electron energy spectra with a relative accuracy on the order of  $10^{-5}$  and possibly beyond (Chapter 5). We realized by experiment how to use terahertz pulses in a semi-infinite interaction scheme to tilt a compressed electron pulse in almost any desired way and moreover, it was found that matter-waves obey the same relation between pulse front tilt and angular dispersion which optical pulses do (Chapter 6). Lastly, all of the above findings—from the profound understanding of pulse compression dynamics with temporal lenses to the multidimensional handles a terahertz irradiated mirror membrane provides—flowed into the design of a final electron pulse compression experiment meeting the record value for isolated, sub-relativistic electron pulses of 12 fs (rms) with record temporal stability (Chapter 7).

So having seen all of this, the questions arises: where do we go from here? Triggered by this thesis' research, new scientific questions arose which await answering. First of all, in the light of future applications it will be interesting to see how the terahertz-based pulse compression schemes behave for space-charged dominated electron pulses—in theory as well as in practice. Second, the theoretical treatment of electron pulse compression of Chapter 2 calls for a full quantum description. Wigner quasiprobability distributions as quantum mechanical equivalent to a classical phase space description might be a promising approach. Third, a complete theoretical framework of tilted matterwave pulses to further support the discovered link between angular dispersion and tilt angle (Chapter 6) along with investigation of other experimental schemes to produce tilted electron pulses are highly desirable.

---

With all of the findings made in the course of this thesis, a route towards a new regime of ultrafast electron diffraction and microscopy emerges. Due to the demonstrated, highly stable and ultrashort electron pulses, the temporal-resolution gap of electron diffraction shrinks to the few-femtosecond regime. With the terahertz compression concept presented here, it is thus possible to resolve the fastest phononic excitations [49, 50] via electron diffraction or to recover collective electronic motion in the mid-IR of tens of THz via electron microscopy [99]. In particular, experimental pump-probe configurations with tight geometrical constraints will benefit from the additional flexibility that the controlled generation of tilted and compressed electron pulses offers.

Furthermore, breaking the femtosecond barrier with isolated electron pulses by the techniques developed in this thesis seems more feasible than ever. Key to this attosecond-angstrom regime will be optically driven temporal lenses with high electric field strength to keep the temporal focal distance and hence the electron pulses as short as possible (see Chapters 2 and 7). Double-stage compression approaches (see Chapter 2) might offer a possibility to meet both of these conditions. Higher terahertz field strengths beyond  $10^7$  V/m and mid-IR few cycle pulses for compression and streaking are readily available and are among the most promising candidates for the generation and characterization of sub-femtosecond electron pulses. Together with terahertz-based electron energy loss/gain spectroscopy (Chapter 5), which also would benefit from higher modulation field strengths, novel concepts for a complete characterization of structural dynamics in space and time are foreseeable involving elastic *and* inelastic processes.

It seems quite realistic, that the path of terahertz control of free electron pulses will be pursued by more and more researchers in the nearer future. This development is already indicated by the growing research interest in that topic. The range of other recently reported experiments spans from the eV-regime [181, 219], over the keV-regime [90, 95] and away from tabletop apparatuses to large facilities and relativistic MeV-scale beams [96–98]. These techniques combined with the concepts demonstrated in the course of this thesis bear great potential for further development. They give rise to high expectations for a new generation of all-optical electron pulse manipulation schemes to be used in electron microscopes, particle accelerators, free-electron lasers and many more. The broad range of possible future experiments enabled by the present work holds promise to bring us a more profound understanding of nature, matter and materials.



# Appendix A

This Appendix contains the derivation of the temporal lens imaging equation and the magnification relation (Eqs. 2.30 and 2.31 in Chapter 2). It is based on the transformation of the covariance matrix from object to image, given by Eq. 2.10:  $\Sigma' = \mathbf{M}_{\text{img}} \Sigma_0 \mathbf{M}_{\text{img}}^T$ , which explicitly reads

$$\begin{aligned} \begin{pmatrix} \sigma_z'^2 & 0 \\ 0 & \sigma_v'^2 \end{pmatrix} &= \begin{pmatrix} 1 - \frac{t'}{f_t} & t + t' - \frac{tt'}{f_t} \\ -\frac{1}{f_t} & 1 - \frac{t}{f_t} \end{pmatrix} \begin{pmatrix} \sigma_z^{02} & 0 \\ 0 & \sigma_v^{02} \end{pmatrix} \begin{pmatrix} 1 - \frac{t'}{f_t} & -\frac{1}{f_t} \\ t + t' - \frac{tt'}{f_t} & 1 - \frac{t}{f_t} \end{pmatrix} \\ &\equiv \frac{1}{f_t^2} \begin{pmatrix} A' & B' \\ C' & D' \end{pmatrix} \end{aligned} \quad (\text{A1})$$

with

$$A' = (f_t - t')^2 \sigma_z^{02} + (f_t t + f_t t' + tt')^2 \sigma_v^{02} \quad (\text{A2})$$

$$B' = C' = -(f_t - t') \sigma_z^{02} + (f_t - t)(f_t t + f_t t' - t't) \sigma_v^{02} \quad (\text{A3})$$

$$D' = \sigma_z^{02} + (f_t - t)^2 \sigma_v^{02}. \quad (\text{A4})$$

The off-diagonal terms (Eq. A3) must vanish in the temporal focus:  $B' = C' = 0$  (Eq. A1). This yields

$$(f_t - t') \underbrace{\begin{pmatrix} \sigma_z^0 \\ \sigma_v^0 \end{pmatrix}}_{=\tau_R}^2 = (f_t - t)(f_t t + f_t t' - t't), \quad (\text{A5})$$

which is equivalent to

$$\frac{1}{f_t} = \frac{1}{t'} + \frac{1}{t + \tau_R^2/(t - f_t)}, \quad (\text{A6})$$

i.e., Eq. 2.30.

The magnification  $m = \sigma'_z/\sigma_z^0$  can be found by using the diagonal terms of Eq. A1, given by Eqs. A2 and A4. We have

$$\sigma_v'^2 = \frac{D'}{f_t^2} \quad (\text{A7})$$

$$\Leftrightarrow \sigma_v'^2 = \frac{1}{f_t^2} \left[ \sigma_z^{02} + (f_t - t)^2 \sigma_v^{02} \right] \quad (\text{A8})$$

$$\Leftrightarrow \left( \frac{\sigma_v'}{\sigma_v^0} \right)^2 = \frac{1}{f_t^2} \left[ \tau_R^2 + (f_t - t)^2 \right]. \quad (\text{A9})$$

Because  $\det(\mathbf{M}_{\text{img}}) = 1$ , the longitudinal emittance is conserved (Eq. 2.12) and  $\sigma'_z/\sigma_z^0 = \sigma_v^0/\sigma_v'$ , which yields Eq. 2.31 as

$$m = \frac{\sigma_v^0}{\sigma_v'} = \frac{1}{\sqrt{[1 - (t/f_t)]^2 + [\tau_R/f_t]^2}}. \quad (\text{A10})$$

# Appendix B

This appendix contains the supplementary material published along with the article [89] of Chapter 4.<sup>1</sup> It gives details on the experimental setup, the terahertz-electron interaction and the data evaluation.

## Experimental setup

The laser system is a Yb:YAG regenerative amplifier [153] which generates 1 ps,  $\sim 350$   $\mu$ J pulses with a central wavelength of 1030 nm and at a repetition rate of 50 kHz. A small fraction of the laser output power is frequency doubled to obtain pulses at 515 nm for photocathode excitation. The cathode consists of a 20 nm gold film on a sapphire substrate, which is illuminated from behind. Electrons are emitted via two-photon photoemission.  $< 100$   $\mu$ W are used for photocathode excitation, the electron source size is  $\sim 5$   $\mu$ m rms (fitting the spot size on the camera as a function of magnetic lens parameters). The electron gun has a cathode-anode spacing of 25 mm, resulting in fields of 3.6 MV/m and 2.8 MV/m at 90 keV and 70 keV operating voltages, respectively. From the measured, uncompressed pulse durations of 780 fs at 90 keV and 930 fs at 70 keV and assuming an initial pulse duration of  $\sim 500$  fs (from the two consecutive two-photon processes), we infer a longitudinal energy spread of 0.6 eV on emission. This is consistent with the measured 4.26 eV work function of similar thin-film gold cathodes [110]. Terahertz fields were generated by optical rectification in lithium niobate; at 7 W pump power, both generation stages produce  $\sim 30$ – $40$  nJ single-cycle pulses at a frequency of  $\sim 0.3$  THz. The streaking terahertz was generated using tilted-pulse-front pumping [88] (for details of the experimental setup, see [153]). For streaking with the butterfly aperture, the THz was focused from inside the vacuum chamber and collinearly with the electron beam, using an off-axis parabolic mirror with a central hole of  $\sim 3$  mm diameter. The compression terahertz

---

<sup>1</sup>The original file can be found at [www.sciencemag.org/content/352/6284/429/suppl/DC1](http://www.sciencemag.org/content/352/6284/429/suppl/DC1).

was generated using a Cerenkov scheme [160]. This approach is more compact and less alignment sensitive than the tilted pulse-front method, which is advantageous here because a delay line in the pump beam was used to control the time-delay of this terahertz field. The compression terahertz was focused with an off-axis parabolic mirror onto the butterfly antenna from outside the vacuum chamber through a 6 mm thick silicon window, with an effective focal distance of about  $\sim 100$  mm. In addition to the delay stage in the compression THz generation path, there is a delay stage in the 515 nm beam, before electron generation. Data collection and the control of the delay stages are automated, and the delay stages can be moved together (for example, to change the time-delay of the compressed pulses with respect to the streaking THz). The distance between the compression interaction and the streaking interaction is  $\sim 0.49$  m. The detector (TemCam-F416, TVIPS GmbH) is located  $\sim 0.55$  m further after the streaking. A first solenoid lens focuses the beam to a spot size of  $3\ \mu\text{m}$  (rms) in the compression aperture, and a second lens focuses the beam between the streaking aperture and the camera. The lenses are mounted kinematically to allow precise alignment and avoid temporal distortions [200], and deflection coils are used to fine-tune the electron alignment at the streaking aperture. A  $50\text{-}\mu\text{m}$ -diameter aperture placed  $\sim 100$  mm before the butterfly resonator is used to improve the transverse beam emittance. The focus of the beam is placed between the butterfly resonator and the camera, resulting in spot sizes of  $11\ \mu\text{m}$  (rms) at the resonator and  $23\ \mu\text{m}$  (rms) at the camera. Beam sizes in the compression and streaking apertures were determined using knife-edge scans. The same electron optical configuration was used regardless of whether compression was applied. The butterfly resonators are laser-machined in  $30\text{-}\mu\text{m}$ -thick aluminum foil. They were designed for a resonance frequency of  $0.3$  THz, and simulations predict field enhancement by a factor of  $\sim 5$  in the center of the resonator. Simulations of the mode profile show that even for the  $11\ \mu\text{m}$  spot size at the streaking resonator, the amplitude of the deflection varies by less than 1% over the electron beam profile. This is confirmed by the excellent agreement between the fit in Figure 4.2 C, which assumes no amplitude variation, and the data of Figure 4.2 B.

## Resonator-free implementation

The mirror is a 70-nm thick aluminum layer and provides a good compromise between electron transmission ( $\sim 30\%$ ) and THz reflectivity ( $> 90\%$ ). The p-polarized THz beam is incident at  $60^\circ$  at the foil; the electron beam intersects at  $27^\circ$ . This angle combination ensures velocity matching over extended THz and electron beam [82]. A single solenoid lens gently focuses the electron beam through the foil to a  $55\ \mu\text{m}$  (rms) spot on the camera, located at a distance of  $\sim 0.68$  m behind the foil.

## Designing the electron-terahertz interaction

An interaction between the electrons and terahertz which scales linearly with field is not possible in free space, because such an interaction (between one photon and one electron) cannot conserve momentum and energy simultaneously. Therefore, a third body must be used to engineer the interaction. The resonators used here localize the THz field to subwavelength dimensions so that the electron effectively passes through the region of strong fields faster than a THz period. Equivalently, the confinement of the electromagnetic field by the resonator leads to evanescent components which are phase-matched to the electron [120]. In the resonator-free implementation, the role of the third body is to abruptly truncate the electromagnetic fields so that the field seen by the electron changes abruptly in time [81, 82]. The momentum change of the electron is given (to first order) by the integral of the Lorentz force on the electron's trajectory. The geometry of the interaction must be chosen to produce a momentum change in the desired control direction. Finally, the forces should be sufficiently uniform over the transverse profile of the beam.

## Scaling of the compression strength with electron energy

Here we briefly estimate how THz compression would work for other electron central energies than the 70 keV in the experiment. For an electron moving along the  $z$ -axis with speed  $v$  in a localized electromagnetic field, we can write the electron's energy increase in the longitudinal direction (ignoring quiver motion) as

$$\delta W = q \int_{-\frac{l}{2}}^{\frac{l}{2}} E_0(z) e^{-i\omega(t(z)-t_0)} dz \quad (\text{B11})$$

where  $q$  is the charge of the electron,  $t_0$  is a reference time,  $t(z) = z/v$  is the time when the electron arrives at coordinate  $z$ , and  $E_0$  is an envelope function describing the resonator mode, which decreases to zero at  $\pm l/2$ . Here, it is assumed that the temporal envelope of the THz field changes slowly in comparison with the time that the electron interacts with the localized field. If the electron transit time through the fields is comparable to the THz period, then dependence on the electron velocity is non-trivial. In analogy with microwave acceleration, this expression can be formally rewritten as

$$\delta W = q\delta V T e^{-i\omega t_0} \quad (\text{B12})$$

where the static voltage change is

$$\delta V \equiv \int_{-\frac{l}{2}}^{\frac{l}{2}} E_0(z) dz \quad (\text{B13})$$

and the (dimensionless) transit-time factor is

$$T \equiv \frac{\int_{-\frac{l}{2}}^{\frac{l}{2}} E_0(z) e^{-\frac{i\omega z}{v}} dz}{\int_{-\frac{l}{2}}^{\frac{l}{2}} E_0(z) dz} \quad (\text{B14})$$

which accounts for the temporal variation of the electric field as the electron passes through the resonator.  $T$  depends on a combination of THz frequency, field localization, and electron velocity and is generally not a monotonic function of these quantities. The maximum of the derivative of the longitudinal energy gain is thus

$$g_E = \frac{d\delta W}{dt_0} = q\delta V\omega T \quad (\text{B15})$$

In a simplified model, we can take the electric field amplitude to be uniform along  $z$  and localized to the thickness of the resonator, which we now take as  $l$ . In this case (assuming that  $\pi l/\beta c$  is much less than the THz period)

$$g_E \approx qE_0l\omega. \quad (\text{B16})$$

In this approximation, the compression strength  $g_E$  is independent of the electron energy, and the focus position scales according to Eq. 4.1 in the main paper. Thus THz field strengths of similar order-of-magnitude as used in the experiment will be suitable for a wide range of experimental conditions in electron diffraction, microscopy or other beam applications.

## THz field strength calibration

The THz field strength for the compression stage was calibrated approximately by measuring the THz power directly behind the silicon prism, for pump power from 1–5 W. To convert to a field strength, we used the field profile measured via electro-optic sampling and the focal parameters of the system. Independently, we measured deflection of the electron beam by the compression stage as a function of pump power used to generate the THz, finding a linear relation between pump power and deflection in the range 3–7 W. The THz field strength for the streaking stage was estimated using electro-optic sampling measurements [153] with similar path lengths and focusing as in the experiment.

## Fitting the pulse duration of the uncompressed pulses

The pulse duration of the uncompressed pulses was determined from the deflectograms using a fitting routine which simultaneously determines pulse duration and the streaking field. The electron pulse profile is assumed to be Gaussian, and the streaking field is parameterized by a varying number of spline points. The deflection is assumed to be the same at all points in the transverse profile of the electron beam. For every set of parameters, a deflectogram can be calculated which includes the effect of streaking and convolution with the unstreaked beam profile at the camera. The error is then given by the rms difference between the measured and calculated deflectograms. The number of spline points is changed to verify that the fit is robust, and the quoted error values correspond to the interval where the error increases by 10% relative to the error of the optimal fit.

## Streaking characterization of the compressed pulses

When the pulse duration is much less than the half period of the streaking terahertz (i.e., with the temporally compressed pulses), it is possible to make a direct reconstruction of monotonic segments of the streaking field, and using the streaking field, the temporal profiles of the electron pulses can be found without making assumptions about their shape. If the pulses are sufficiently short, then the streaking field at the zero crossing is to a very good approximation linear over the range required to convert the streaking profile to a time-trace. This is illustrated in Figure B1, which shows the center of the streaked pulse vs. delay time. The linear calibration taken from this dataset was used to determine the time-axis in Figure 4.4D. This linear calibration fails for longer pulses because the curvature of the streaking field vs. time distorts the streaked pattern, even when the pulse is streaked at the zero crossing. In this case, the streaking field reconstruction becomes important. To reconstruct the streaking field from the deflectograms, we measure deflectograms with optimally compressed pulses, using a delay step which is much smaller than the electron pulse duration. We then average the deflectogram horizontally over a monotonic section of the deflectogram (Figure B1 A). This generates a “streaking profile” (Figure B1 B) that is equivalent to streaking a nearly rectangular pulse matched to this monotonic segment. The streaking profile corresponds to a number of electrons  $\rho_i$  detected per pixel  $i$ . The central arrival time corresponding to deflection into pixel  $i$  is  $t_i = \sum_{n=1}^i \rho_n / I + t_0$ , where  $t_0$  is an arbitrary temporal offset, and  $I$  is the effective number of electrons per unit time. The reconstructed deflection vs. time-delay (Figure B1 C) is used to nonlinearly rescale the streaked pulses and determine the temporal profile of the

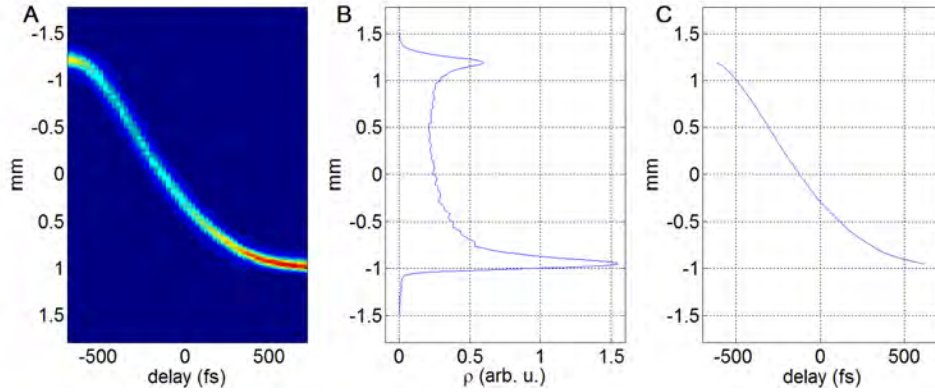


**Figure B1:** (A) Monotonic portion of a deflectogram used to infer streaking field. (B) Deflectograms as in (A) are integrated horizontally to obtain  $\rho$  (several deflectograms are averaged for better signal-to-noise). (C) Numerically integrating  $\rho$  results in the streaking field vs. time.

electron pulses in Figure 4.3 B. Due to the non-zero (unstreaked) beam profile on the camera, the streaking resolution is reduced at the turning points, which introduces distortion at the edges of the inferred temporal profiles of the longest pulses in Figure 4.3 B. Note that the reconstruction in Fig. B1 C is truncated well before the turning points.

## Particle tracing simulations

Simulations of pulse compression were carried out using General Particle Tracer [185]. The distances between optical elements match the experimental distances within uncertainties of  $\sim 5$  mm. The initial pulse duration at the cathode was 500 fs. The momentum distribution at the source was assumed to be hemispherical [110], and the energy spread was chosen to be 0.6 eV, to match the uncompressed pulse durations measured at the position of the streaking resonator. The rms source size of  $5.3 \mu\text{m}$  was chosen to reproduce the measured spot size at the compression point. The compression element was modeled as a thin scattering plane placed at  $45^\circ$  to the beam and which imparts a momentum to the electrons based on their arrival time. The momentum change was oriented along the direction of maximum electric field in the resonator. It was assumed to be sinusoidal in time, uniform and synchronous across the plane of the resonator. The traces in Fig. 4.3 B are histograms of the arrival time of 104 particles at the streaking point. Aperturing of the beam was not taken into account, but in the experiment, the aperture is located at a point where the transverse spatial coordinate should not be correlated with arrival time. To simulate

3 fs (FWHM) pulses, the electron energy was increased to 150 keV, the initial energy spread was reduced to 0.2 eV, and the source size was reduced to 0.1  $\mu\text{m}$  [106].



# Appendix C

This appendix contains a shortened version of the supplementary material published along with Ref. [104] of Chapter 6.<sup>2</sup> It gives details on the analytic expressions in the article and the data evaluation.

The first section of the original version containing the derivation of closed-form expressions for the momentum transfer at a perfect reflector can be found in coauthor Andrey Ryabov's Ph.D. thesis [173]. Here, only the final expressions and substitutions required to obtain Eqs. 6.1–6.3 of Chapter 6 are given.

The analytic derivation [173] yields

$$p_{x'}(\tau) = e E_0 \operatorname{sign}(\cos \alpha_e) \operatorname{sign}(\cos \alpha) \frac{\cos(\omega\tau + \phi)}{\omega} \times \left( \frac{\sin(\alpha - \alpha_e)}{(1 - \beta \cos(\alpha - \alpha_e))} + \frac{\sin(\alpha + \alpha_e)}{(1 + \beta \cos(\alpha + \alpha_e))} \right), \quad (\text{C1})$$

$$p_{y'}(\tau) = e E_0 \operatorname{sign}(\cos \alpha_e) \operatorname{sign}(\cos \alpha) \frac{\cos(\omega\tau + \phi)}{\omega} \times \left( \frac{\cos(\alpha + \alpha_e) + \beta}{(1 + \beta \cos(\alpha + \alpha_e))} - \frac{\cos(\alpha - \alpha_e) - \beta}{(1 - \beta \cos(\alpha - \alpha_e))} \right), \quad (\text{C2})$$

where  $p_{x'}$  and  $p_{y'}$  are the respective momentum changes perpendicular and parallel to the electron trajectory as a function of its arrival time  $\tau$ ;  $e$  is the electron charge;  $E_0$  is the electric field strength;  $\alpha_e$  and  $\alpha$  are the electron incidence and terahertz plane wave incidence angles relative to the mirror's surface normal, respectively;  $\omega$  is the optical angular frequency;  $\phi$  is an arbitrary phase offset and  $\beta$  is the electron velocity relative to the speed of light.

---

<sup>2</sup>The original version can be found at <http://link.aps.org/supplemental/10.1103/PhysRevLett.121.094801>.

Making the substitutions

$$\begin{aligned}\alpha_e &\rightarrow -\theta_e, \\ \alpha &\rightarrow \theta_{THz} + \pi, \\ \tau &\rightarrow t, \\ \{x', y', z\} &\rightarrow \{z, y, x\}, \\ \phi &= -\frac{\pi}{2},\end{aligned}$$

according to the definitions of Chapter 6, we obtain Eqs. 6.1–6.3.

## Momentum change in case of pulses with arbitrary bandwidth

For the derivation of Eq. C1 and C2 we assumed a monochromatic plane wave. However, the extension to electromagnetic pulses of arbitrary bandwidth can be done by summation over the plane wave contributions for different frequencies and phases, which constitute an optical pulse:

$$A(t) = \sum_k a_k \sin(\omega_k t + \phi_k), \quad (\text{C3})$$

where  $a_k$ ,  $\omega_k$  and  $\phi_k$  are  $k$ -th component amplitude, angular frequency and phase, respectively,  $A(t)$  is a time-dependent field, which interacts with an electron [...]. After this substitution, we can rewrite the equations (C1) and (C2) as

$$\begin{aligned}p_{x'}(\tau) = e &\left( \frac{\sin(\alpha - \alpha_e)}{(1 - \beta \cos(\alpha - \alpha_e))} + \frac{\sin(\alpha + \alpha_e)}{(1 + \beta \cos(\alpha + \alpha_e))} \right) \\ &\sum_k a_k \frac{\cos(\omega_k \tau + \phi_k)}{\omega_k};\end{aligned} \quad (\text{C4})$$

$$\begin{aligned}p_{y'}(\tau) = e &\left( \frac{\cos(\alpha + \alpha_e) + \beta}{(1 + \beta \cos(\alpha + \alpha_e))} - \frac{\cos(\alpha - \alpha_e) - \beta}{(1 - \beta \cos(\alpha - \alpha_e))} \right) \\ &\sum_k a_k \frac{\cos(\omega_k \tau + \phi_k)}{\omega_k}.\end{aligned} \quad (\text{C5})$$

Here all sign-functions are omitted. Sums can be substituted for integrals in case of a continuous spectrum.

## Dynamics of electron pulse compression and formation of tilted pulses

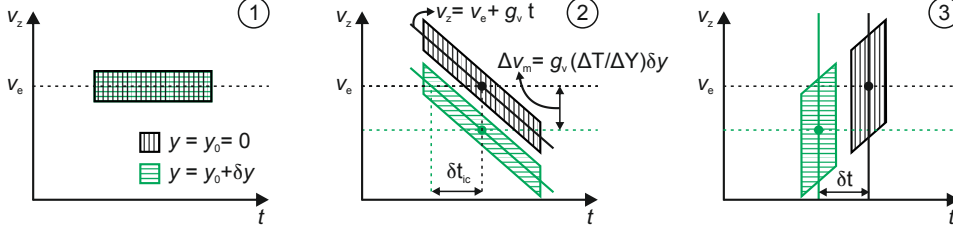


**Figure C1:** Longitudinal phase space representation illustrating the formation of a tilted pulse caused by velocity mismatch at a thin foil. Rectangles illustrate the phase space volume containing the electrons crossing the mirror element at two different  $y$ -positions (central and offset). Initially, they overlap perfectly (1). Interaction with the THz wave at the mirror, when there is velocity mismatch, causes a velocity change  $\Delta v_m$  of the offset part, while simultaneously creating a linear correlation (2). At the temporal focus (3) the parts are separated in time by  $\delta t$ , which is equal to the temporal spacing of parts of equal energy (velocity)  $\delta t_{ic}$ .

The location of the temporal focus  $f_{temp}$  can be calculated by approximating  $\Delta p_z \approx eE_0 A_z t$  around  $t=0$ .<sup>3</sup> The resulting longitudinal velocity changes are given by  $\Delta v_z \approx g_v t$ , where  $g_v = eE_0 A_z / (\gamma^3 m_e)$  is the compression strength,  $\gamma$  the Lorentz factor and  $m_e$  the electron rest mass. Here we made use of the linear approximation  $v_z(p_z) \approx v_e + (p_z - p_z(v_e)) / (\gamma(v_e)^3 m_e)$ , which is justified for small momentum changes relative to the initial. The time it takes for the trailing part of the pulse to catch up with the leading ones is given by  $\tau_{temp} = v_e / g_v$  (assuming negligible energy spread). Thus, a minimum pulse duration is obtained at a distance

$$f_{temp} = v_e \tau_{temp} = \frac{\beta^2 \gamma^3 m_e c^2}{E_0 A_z e} \quad (C6)$$

behind the foil.

If the mirror is rotated away from the velocity condition, electrons that are passing through at different  $y$ -positions obtain a longitudinal velocity change given by

$$\Delta v_z \approx g_v \left( t + \frac{\Delta T}{\Delta Y} y \right). \quad (C7)$$

The first term here is responsible for the formation of a temporal focus, i.e., compression, while the second is an additional,  $y$ -dependent velocity term leading to the formation of a tilted pulse. This process is illustrated in Fig. C1 at the example

<sup>3</sup>Here and in the following we use the variable definitions of the main text.

of two parts of the pulse, which cross the mirror at the center ( $y = 0$ , black) and at  $\delta y$  (green). After the interaction with the electromagnetic wave both parts are sheared in phase space with a slope corresponding to the compression strength  $g_v$ , but the offset part is shifted in velocity by  $\Delta v_m = g_v(\Delta T/\Delta Y)\delta y$ . Consequently, parts of different  $y$  positions  $\delta y$  arrive at different times  $\delta t$  at the temporal focus. From the geometry of the phase space we see that points of equal kinetic energy (isochromatic points) are separated in time by

$$\delta t_{ic} = \frac{\Delta v_m}{g_v} = \frac{\Delta T}{\Delta Y} \delta y. \quad (\text{C8})$$

The distance between isochromatic points does not change when the pulse propagates. Propagation to the temporal focus, i.e., for a time  $\tau_{\text{temp}}$  and where  $\delta t_{ic} = \delta t$ , thus, results in arrival time differences of

$$\frac{\delta t}{\delta y} = \frac{\Delta T}{\Delta Y}. \quad (\text{C9})$$

We note, that Eq. C9 holds under the assumption of small momentum changes also in the relativistic case.

## Relation between momentum transfer, tilt angle and angular dispersion for the reported experiment

For the special case of generating tilted electron pulses as described in the main text, Eq. 6.7 can also be derived analytically. By dividing Eq. 6.2 and 6.3 we obtain

$$\frac{\Delta p_y}{\Delta p_z} = -\frac{\sin \theta_{\text{THz}} - \beta^{-1} \sin \theta_e}{c \sin \theta_e} = -v_e \frac{\Delta T}{\Delta Y}. \quad (\text{C10})$$

The left hand side relates to the angular dispersion via

$$\frac{\Delta p_y}{\Delta p_z} = -\lambda_{\text{db}}^0 \frac{d\epsilon}{d\lambda_{\text{db}}} \quad (\text{C11})$$

(see main text). The right hand side of Eq. C10 equals  $-\tan \alpha$  (Eq. 6.6), which in combination with Eq. C11 yields

$$\tan \alpha = \lambda_{\text{db}}^0 \frac{d\epsilon}{d\lambda_{\text{db}}}. \quad (\text{C12})$$

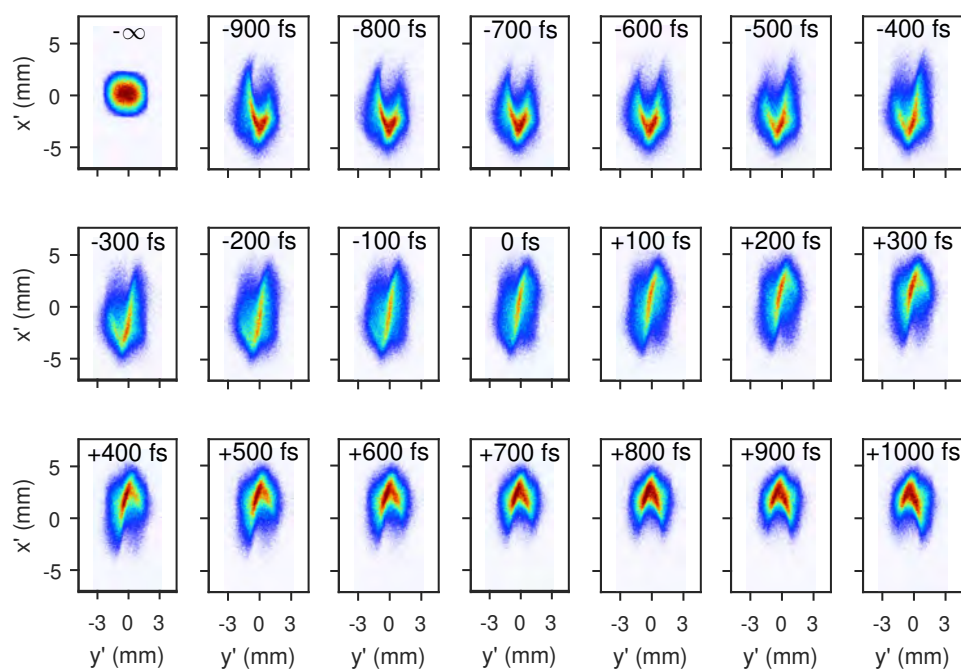


**Figure C2:** Raw screen images used to obtain the data points as shown in Fig. 6.3 b for various streaking delays. For clarity only every other images is displayed. Primed variables refer to the (magnified) screen dimensions.

## Evaluation of pulse front tilt from the measured streaking images

In order to obtain the data points as shown in Fig. 6.3 b in the main text, we analyze the raw streaking images for different THz delays, which are shown in Fig. C2. These images are binned along  $y$  (binsize 78 micron) and integrated, yielding streaked pulse profiles. The center of these profiles as a function of streaking delay are then fitted with a sinusoidal function in order to obtain the zero crossing  $t_0$  and consequently the arrival time differences for different segments in  $y$  (Fig. 6.3 b). The slope, extracted from a linear fit of  $t_0$  as shown in the inset of Fig. 6.3 b, yields the arrival time difference  $\delta t/\delta y$  for the given electron incidence angle, which are plotted as blue dots in Fig. 6.3 c. These values are furthermore used to obtain the time axis in Fig. 6.3 a for the plotted dashed lines. Uncertainties are inferred from the confidence intervals of the respective fit parameters and propagated assuming no correlation. We obtain the conversion factor between on screen units  $\{y', x'\}$  and foil/mirror units  $\{y, x\}$ , that is, the magnification, by using the 1.5 mm aperture of the foil as scale. Its borders can be faintly seen in Fig. C2 in the upper left panel (streaking delay  $-\infty$ ).

# Data Archiving

The experimental raw data, evaluation files, and original figures of this thesis are stored on the Data Archive Server of the Laboratory for Attosecond Physics at the Max Planck Institute of Quantum Optics:

`/afs/ipp-garching.mpg.de/mpq/lap/publication_archive`

The source data of all figures in Chapters 1 and 2, as well as in the prefaces to Chapters 3 and 6 is stored relative to the root folder at

`/Theses/2019/Ehberger, Dominik (PhD)`

The subfolders contained therein are organized by chapter using the same figure numbers as in this thesis.

Raw data and information about the data processing performed in order to obtain the final figures of the previously published articles contained in Chapters 3–7 are stored in the following folders relative to the root directory.

## **Chapter 3**

`/Papers/2016/Tsarev_ApplPhysB THz generation`

## **Chapter 4**

`/Papers/2016/Kealhofer_Science THz control`

## **Chapter 5**

`/Papers/2018/Ehberger_StrucDyn THz ToF`

## **Chapter 6**

`/Papers/2018/Ehberger_PhyRevLett tilted pulses`

## **Chapter 7**

`/Papers/2019/Ehberger_PhysRev_Appl mirror compression`



# Bibliography

- [1] F. Perakis, K. Amann-Winkel, F. Lehmkuhler, M. Sprung, D. Mariedahl, J. A. Sellberg, H. Pathak, A. Späh, F. Cavalca, D. Schlesinger, A. Ricci, A. Jain, B. Massani, F. Aubree, C. J. Benmore, T. Loerting, G. Grübel, L. G. M. Pettersson, and A. Nilsson, [Diffusive dynamics during the high-to-low density transition in amorphous ice](#), *Proceedings of the National Academy of Sciences of the United States of America* **114**, 8193 (2017).
- [2] K. H. Kim, A. Späh, H. Pathak, F. Perakis, D. Mariedahl, K. Amann-Winkel, J. A. Sellberg, J. H. Lee, S. Kim, J. Park, K. H. Nam, T. Katayama, and A. Nilsson, [Maxima in the thermodynamic response and correlation functions of deeply supercooled water](#), *Science* **358**, 1589 (2017).
- [3] R. P. Feynman, [Simulating physics with computers](#), *International Journal of Theoretical Physics* **21**, 467 (1982).
- [4] K. Burke, [Perspective on density functional theory](#), *Journal of Chemical Physics* **136**, 150901 (2012).
- [5] I. Bloch, J. Dalibard, and S. Nascimbène, [Quantum simulations with ultracold quantum gases](#), *Nature Physics* **8**, 267 (2012).
- [6] P. W. Shor, [Algorithms for quantum computation: discrete logarithms and factoring](#), in *Proceedings 35th Annual Symposium on Foundations of Computer Science* (1994), pp. 124–134.
- [7] M. Imada, A. Fujimori, and Y. Tokura, [Metal-insulator transitions](#), *Reviews of Modern Physics* **70**, 1039 (1998).
- [8] P. Baum, D. S. Yang, and A. H. Zewail, [4D Visualization of Transitional Structures in Phase Transformations by Electron Diffraction](#), *Science* **318**, 788 (2007).

- [9] V. R. Morrison, R. P. Chatelain, K. L. Tiwari, A. Hendaoui, A. Bruhács, M. Chaker, and B. J. Siwick, [A photoinduced metal-like phase of monoclinic VO<sub>2</sub> revealed by ultrafast electron diffraction](#), *Science* **346**, 445 (2014).
- [10] B. T. O’Callahan, A. C. Jones, J. Hyung Park, D. H. Cobden, J. M. Atkin, and M. B. Raschke, [Inhomogeneity of the ultrafast insulator-to-metal transition dynamics of VO<sub>2</sub>](#), *Nature Communications* **6**, 6849 (2015).
- [11] M. R. Otto, L. P. René de Cotret, D. A. Valverde-Chavez, K. L. Tiwari, N. Émond, M. Chaker, D. G. Cooke, and B. J. Siwick, [How optical excitation controls the structure and properties of vanadium dioxide](#), *Proceedings of the National Academy of Sciences of the United States of America* **116**, 450 (2019).
- [12] E. Beaurepaire, J.-C. Merle, A. Daunois, and J.-Y. Bigot, [Ultrafast Spin Dynamics in Ferromagnetic Nickel](#), *Physical Review Letters* **76**, 4250 (1996).
- [13] P. Tengdin, W. You, C. Chen, X. Shi, D. Zusin, Y. Zhang, C. Gentry, A. Blonsky, M. Keller, P. M. Oppeneer, H. C. Kapteyn, Z. Tao, and M. M. Murnane, [Critical behavior within 20 fs drives the out-of-equilibrium laser-induced magnetic phase transition in nickel](#), *Science Advances* **4**, eaap9744 (2018).
- [14] C. Dornes, Y. Acremann, M. Savoini, M. Kubli, M. J. Neugebauer, E. Abreu, L. Huber, G. Lantz, C. A. F. Vaz, H. Lemke, E. M. Bothschafter, M. Porer, V. Esposito, L. Rettig, M. Buzzi, A. Alberca, Y. W. Windsor, P. Beaud, U. Staub, D. Zhu, S. Song, J. M. Glowonia, and S. L. Johnson, [The ultrafast Einstein-de Haas effect](#), *Nature* **565**, 209 (2019).
- [15] D. Fausti, R. I. Tobey, N. Dean, S. Kaiser, A. Dienst, M. C. Hoffmann, S. Pyon, T. Takayama, H. Takagi, and A. Cavalleri, [Light-Induced Superconductivity in a Stripe-Ordered Cuprate](#), *Science* **331**, 189 (2011).
- [16] R. Mankowsky, A. Subedi, M. Först, S. O. Mariager, M. Chollet, H. T. Lemke, J. S. Robinson, J. M. Glowonia, M. P. Minitti, A. Frano, M. Fechner, N. A. Spaldin, T. Loew, B. Keimer, A. Georges, and A. Cavalleri, [Nonlinear lattice dynamics as a basis for enhanced superconductivity in YBa<sub>2</sub>Cu<sub>3</sub>O<sub>6.5</sub>](#), *Nature* **516**, 71 (2014).
- [17] W. Friedrich, P. Knipping, and M. Laue, [Interferenzerscheinungen bei Röntgenstrahlen](#), *Annalen der Physik* **346**, 971 (1913).
- [18] W. L. Bragg, [The Specular Reflection of X-rays.](#), *Nature* **90**, 410 (1912).

- [19] W. H. Bragg and W. L. Bragg, [Die Reflexion von Röntgen-Strahlen durch Kristalle](#), *Zeitschrift für anorganische Chemie* **90**, 169 (1914).
- [20] J. D. Watson and F. H. C. Crick, [Molecular Structure of Nucleic Acids: A Structure for Deoxyribose Nucleic Acid](#), *Nature* **171**, 737 (1953).
- [21] G. P. Thomson and A. Reid, [Diffraction of Cathode Rays by a Thin Film](#), *Nature* **119**, 890 (1927).
- [22] C. J. Davisson and L. H. Germer, [Reflection of Electrons by a Crystal of Nickel](#), *Proceedings of the National Academy of Sciences of the United States of America* **14**, 317 (1928).
- [23] E. W. Müller, [Das Feldionenmikroskop](#), *Zeitschrift für Physik* **131**, 136 (1951).
- [24] E. W. Müller and K. Bahadur, [Field Ionization of Gases at a Metal Surface and the Resolution of the Field Ion Microscope](#), *Physical Review* **102**, 624 (1956).
- [25] S. Marchesini, H. He, H. N. Chapman, S. P. Hau-Riege, A. Noy, M. R. Howells, U. Weierstall, and J. C. H. Spence, [X-ray image reconstruction from a diffraction pattern alone](#), *Physical Review B* **68**, 140101 (2003).
- [26] H. N. Chapman, A. Barty, S. Marchesini, A. Noy, S. P. Hau-Riege, C. Cui, M. R. Howells, R. Rosen, H. He, J. C. H. Spence, U. Weierstall, T. Beetz, C. Jacobsen, and D. Shapiro, [High-resolution ab initio three-dimensional x-ray diffraction microscopy](#), *Journal of the Optical Society of America* **23**, 1179 (2006).
- [27] D. M. Hoffman, V. I. Karasev, and M. S. Banks, [Temporal presentation protocols in stereoscopic displays: Flicker visibility, perceived motion, and perceived depth](#), *Journal of the Society for Information Display* **19**, 271 (2011).
- [28] V. S. Yakovlev, M. I. Stockman, F. Krausz, and P. Baum, [Atomic-scale diffractive imaging of sub-cycle electron dynamics in condensed matter](#), *Scientific Reports* **5**, 14581 (2015).
- [29] G. Mourou and S. Williamson, [Picosecond electron diffraction](#), *Applied Physics Letters* **41**, 44 (1982).
- [30] S. Williamson, G. Mourou, and J. C. M. Li, [Time-Resolved Laser-Induced Phase Transformation in Aluminum](#), *Physical Review Letters* **52**, 2364 (1984).
- [31] A. H. Zewail, [Four-Dimensional Electron Microscopy](#), *Science* **328**, 187 (2010).

- [32] G. Sciaini and R. J. D. Miller, [Femtosecond electron diffraction: heralding the era of atomically resolved dynamics](#), Reports On Progress In Physics **74**, 096101 (2011).
- [33] R. J. D. Miller, [Femtosecond Crystallography with Ultrabright Electrons and X-rays: Capturing Chemistry in Action](#), Science **343**, 1108 (2014).
- [34] B. J. Siwick, J. R. Dwyer, R. E. Jordan, and R. J. D. Miller, [An Atomic-Level View of Melting Using Femtosecond Electron Diffraction](#), Science **302**, 1382 (2003).
- [35] F. Carbone, P. Baum, P. Rudolf, and A. H. Zewail, [Structural Preablation Dynamics of Graphite Observed by Ultrafast Electron Crystallography](#), Physical Review Letters **100**, 035501 (2008).
- [36] G. Sciaini, M. Harb, S. G. Kruglik, T. Payer, C. T. Hebeisen, F.-J. Meyer Zu Heringdorf, M. Yamaguchi, M. Horn-von Hoegen, R. Ernstorfer, and R. J. D. Miller, [Electronic acceleration of atomic motions and disordering in bismuth](#), Nature **458**, 56 (2009).
- [37] M. Eichberger, H. Schafer, M. Krumova, M. Beyer, J. Demsar, H. Berger, G. Moriena, G. Sciaini, and R. J. D. Miller, [Snapshots of cooperative atomic motions in the optical suppression of charge density waves](#), Nature **468**, 799 (2010).
- [38] C. I. Bлага, J. L. Xu, A. D. DiChiara, E. Sistrunk, K. K. Zhang, P. Agostini, T. A. Miller, L. F. DiMauro, and C. D. Lin, [Imaging ultrafast molecular dynamics with laser-induced electron diffraction](#), Nature **483**, 194 (2012).
- [39] T. Ishikawa, S. A. Hayes, S. Keskin, G. Corthey, M. Hada, K. Pichugin, A. Marx, J. Hirscht, K. Shionuma, K. Onda, Y. Okimoto, S. Koshihara, T. Yamamoto, H. B. Cui, M. Nomura, Y. Oshima, M. Abdel-Jawad, R. Kato, and R. J. D. Miller, [Direct observation of collective modes coupled to molecular orbital-driven charge transfer](#), Science **350**, 1501 (2015).
- [40] L. Waldecker, T. A. Miller, M. Rudé, R. Bertoni, J. Osmond, V. Pruneri, R. E. Simpson, R. Ernstorfer, and S. Wall, [Time-domain separation of optical properties from structural transitions in resonantly bonded materials](#), Nature Materials **14**, 991 (2015).
- [41] X. Fu, B. Chen, J. Tang, M. T. Hassan, and A. H. Zewail, [Imaging rotational dynamics of nanoparticles in liquid by 4D electron microscopy](#), Science **355**, 494 (2017).

- [42] T. Frigge, B. Hafke, T. Witte, B. Krenzer, C. Streubühr, A. Samad Syed, V. Mikšić Trontl, I. Avigo, P. Zhou, M. Ligges, D. von der Linde, U. Boven-siepen, M. Horn-von Hoegen, S. Wippermann, A. Lücke, S. Sanna, U. Gerst-mann, and W. G. Schmidt, [Optically excited structural transition in atomic wires on surfaces at the quantum limit](#), *Nature* **544**, 207 (2017).
- [43] K. E. Priebe, C. Rathje, S. V. Yalunin, T. Hohage, A. Feist, S. Schäfer, and C. Ropers, [Attosecond electron pulse trains and quantum state reconstruction in ultrafast transmission electron microscopy](#), *Nature Photonics* **11**, 793 (2017).
- [44] Y. Morimoto and P. Baum, [Diffraction and microscopy with attosecond elec-tron pulse trains](#), *Nature Physics* **14**, 252 (2018).
- [45] M. Kozák, N. Schönenberger, and P. Hommelhoff, [Ponderomotive Generation and Detection of Attosecond Free-Electron Pulse Trains](#), *Physical Review Let-ters* **120**, 103203 (2018).
- [46] W. Ackermann, G. Asova, V. Ayvazyan, A. Azima, N. Baboi, J. Baehr, V. Balandin, B. Beutner, A. Brandt, A. Bolzmann, R. Brinkmann, O. I. Brovko, M. Castellano, P. Castro, L. Catani, E. Chiadroni, S. Choroba, A. Cianchi, J. T. Costello, D. Cubaynes, J. Dardis, W. Decking, H. Delsim-Hashemi, A. Delserieys, G. Di Pirro, M. Dohlus, S. Duesterer, A. Eckhardt, H. T. Edwards, B. Faatz, J. Feldhaus, K. Flöttmann, J. Frisch, L. Fröhlich, T. Garvey, U. Gensch, C. Gerth, M. Görler, N. Golubeva, H.-J. Grabosch, M. Grecki, O. Grimm, K. Hacker, U. Hahn, J. H. Han, K. Honkavaara, T. Hott, M. Hüning, Y. Ivanisenko, E. Jaeschke, W. Jalmuzna, T. Jezynski, R. Kam-mering, V. Katalev, K. Kavanagh, E. T. Kennedy, S. Khodyachykh, K. Klose, V. Kocharyan, M. Körfer, M. Kollwe, W. Koprek, S. Korepanov, D. Kostin, M. Krassilnikov, G. Kube, M. Kuhlmann, C. L. S. Lewis, L. Lilje, T. Limberg, D. Lipka, F. Löhler, H. Luna, M. Luong, M. Martins, M. Meyer, P. Michelato, V. Miltchev, W. D. Möller, L. Monaco, W. F. O. Müller, A. Napieralski, O. Napoly, P. Nicolosi, D. Nölle, T. Nuñez, A. Oppelt, C. Pagani, R. Paparella, N. Pchalek, J. Pedregosa-Gutierrez, B. Petersen, B. Petrosyan, G. Petrosyan, L. Petrosyan, J. Pflüger, E. Plönjes, L. Poletto, K. Pozniak, E. Prat, D. Proch, P. Pucyk, P. Radcliffe, H. Redlin, K. Rehlich, M. Richter, M. Roehrs, J. Roen-sch, R. Romaniuk, M. Ross, J. Rossbach, V. Rybnikov, M. Sachwitz, E. L. Saldin, W. Sandner, H. Schlarb, B. Schmidt, M. Schmitz, P. Schmüser, J. R. Schneider, E. A. Schneidmiller, S. Schnepf, S. Schreiber, M. Seidel, D. Ser-tore, A. V. Shabunov, C. Simon, S. Simrock, E. Sombrowski, A. A. Sorokin, P. Spanknebel, R. Spesyvtsev, L. Staykov, B. Steffen, F. Stephan, F. Stulle, H. Thom, K. Tiedtke, M. Tischer, S. Toleikis, R. Treusch, D. Trines, I. Tsakov,

- E. Vogel, T. Weiland, H. Weise, M. Wellhöffer, M. Wendt, I. Will, A. Winter, K. Wittenburg, W. Wurth, P. Yeates, M. V. Yurkov, I. Zagorodnov, and K. Zapfe, [Operation of a free-electron laser from the extreme ultraviolet to the water window](#), *Nature Photonics* **1**, 336 (2007).
- [47] M. Chollet, R. Alonso-Mori, M. Cammarata, D. Damiani, J. Defever, J. T. Delor, Y. Feng, J. M. Glowina, J. B. Langton, S. Nelson, K. Ramsey, A. Robert, M. Sikorski, S. Song, D. Stefanescu, V. Srinivasan, D. Zhu, H. T. Lemke, and D. M. Fritz, [The X-ray Pump-Probe instrument at the Linac Coherent Light Source](#), *Journal of Synchrotron Radiation* **22**, 503 (2015).
- [48] H. C. Shao and A. F. Starace, [Detecting Electron Motion in Atoms and Molecules](#), *Physical Review Letters* **105**, 263201 (2010).
- [49] K. Ishioka, M. Hase, M. Kitajima, L. Wirtz, A. Rubio, and H. Petek, [Ultrafast electron-phonon decoupling in graphite](#), *Physical Review B* **77**, 121402 (2008).
- [50] L. Waldecker, T. Vasileiadis, R. Bertoni, R. Ernstorfer, T. Zier, F. H. Valencia, M. E. Garcia, and E. S. Zijlstra, [Coherent and incoherent structural dynamics in laser-excited antimony](#), *Physical Review B* **95**, 054302 (2017).
- [51] T. Brabec and F. Krausz, [Intense few-cycle laser fields: Frontiers of nonlinear optics](#), *Reviews of Modern Physics* **72**, 545 (2000).
- [52] L. Xu, C. Spielmann, A. Poppe, T. Brabec, F. Krausz, and T. W. Hänsch, [Route to phase control of ultrashort light pulses](#), *Optics Letters* **21**, 2008 (1996).
- [53] H. R. Telle, G. Steinmeyer, A. E. Dunlop, J. Stenger, D. H. Sutter, and U. Keller, [Carrier-envelope offset phase control: A novel concept for absolute optical frequency measurement and ultrashort pulse generation](#), *Applied Physics B* **69**, 327 (1999).
- [54] M. Hentschel, R. Kienberger, C. Spielmann, G. A. Reider, N. Milosevic, T. Brabec, P. Corkum, U. Heinzmann, M. Drescher, and F. Krausz, [Attosecond metrology](#), *Nature* **414**, 509 (2001).
- [55] P. B. Corkum and F. Krausz, [Attosecond science](#), *Nature Physics* **3**, 381 (2007).
- [56] S. D. Vartak and N. M. Lawandy, [Breaking the femtosecond barrier - a method for generating attosecond pulses of electrons and photons](#), *Optics Communications* **120**, 184 (1995).

- 
- [57] E. Fill, L. Veisz, A. Apolonski, and F. Krausz, [Sub-fs electron pulses for ultrafast electron diffraction](#), *New Journal of Physics* **8**, 272 (2006).
- [58] C. Varin and M. Piché, [Relativistic attosecond electron pulses from a free-space laser-acceleration scheme](#), *Physical Review E* **74**, 045602 (2006).
- [59] P. Baum and A. H. Zewail, [Attosecond electron pulses for 4D diffraction and microscopy](#), *Proceedings of the National Academy of Sciences of the United States of America* **104**, 18409 (2007).
- [60] L. Veisz, G. Kurkin, K. Chernov, V. Tarnetsky, A. Apolonski, F. Krausz, and E. Fill, [Hybrid DC-AC electron gun for fs-electron pulse generation](#), *New Journal of Physics* **9**, 451 (2007).
- [61] R. P. Chatelain, V. R. Morrison, C. Godbout, and B. J. Siwick, [Ultrafast electron diffraction with radio-frequency compressed electron pulses](#), *Applied Physics Letters* **101**, 081901 (2012).
- [62] A. Gliserin, A. Apolonski, F. Krausz, and P. Baum, [Compression of single-electron pulses with a microwave cavity](#), *New Journal of Physics* **14**, 073055 (2012).
- [63] T. van Oudheusden, P. L. E. M. Pasmans, S. B. van der Geer, M. J. de Loos, M. J. van der Wiel, and O. J. Luiten, [Compression of Subrelativistic Space-Charge-Dominated Electron Bunches for Single-Shot Femtosecond Electron Diffraction](#), *Physical Review Letters* **105**, 264801 (2010).
- [64] A. Gliserin, M. Walbran, F. Krausz, and P. Baum, [Sub-phonon-period compression of electron pulses for atomic diffraction](#), *Nature Communications* **6**, 8723 (2015).
- [65] J. Maxson, D. Cesar, G. Calmasini, A. Ody, P. Musumeci, and D. Alesini, [Direct Measurement of Sub-10 fs Relativistic Electron Beams with Ultralow Emittance](#), *Physical Review Letters* **118** (2017).
- [66] M. Walbran, A. Gliserin, K. Jung, J. Kim, and P. Baum, [5-Femtosecond Laser-Electron Synchronization for Pump-Probe Crystallography and Diffraction](#), *Physical Review Applied* **4**, 044013 (2015).
- [67] M. R. Otto, L. P. René de Cotret, M. J. Stern, and B. J. Siwick, [Solving the jitter problem in microwave compressed ultrafast electron diffraction instruments: Robust sub-50 fs cavity-laser phase stabilization](#), *Structural Dynamics* **4**, 051101 (2017).

- [68] T. Heinzl and A. Ilderton, [A Lorentz and gauge invariant measure of laser intensity](#), *Optics Communications* **282**, 1879 (2009).
- [69] P. L. Kapitza and P. A. M. Dirac, [The reflection of electrons from standing light waves](#), *Mathematical Proceedings of the Cambridge Philosophical Society* **29**, 297 (1933).
- [70] D. L. Freimund, K. Aflatooni, and H. Batelaan, [Observation of the Kapitza-Dirac effect](#), *Nature* **413**, 142 (2001).
- [71] M. Kozák, T. Eckstein, N. Schönenberger, and P. Hommelhoff, [Inelastic ponderomotive scattering of electrons at a high-intensity optical travelling wave in vacuum](#), *Nature Physics* **14**, 121 (2018).
- [72] S. Carbajo, E. A. Nanni, L. J. Wong, G. Moriena, P. D. Keathley, G. Laurent, R. J. D. Miller, and F. X. Kärtner, [Direct longitudinal laser acceleration of electrons in free space](#), *Physical Review Accelerators and Beams* **19**, 021303 (2016).
- [73] J. Breuer and P. Hommelhoff, [Laser-Based Acceleration of Nonrelativistic Electrons at a Dielectric Structure](#), *Physical Review Letters* **111**, 134803 (2013).
- [74] E. A. Peralta, K. Soong, R. J. England, E. R. Colby, Z. Wu, B. Montazeri, C. McGuinness, J. McNeur, K. J. Leedle, D. Walz, E. B. Sozer, B. Cowan, B. Schwartz, G. Travish, and R. L. Byer, [Demonstration of electron acceleration in a laser-driven dielectric microstructure](#), *Nature* **503**, 91 (2013).
- [75] R. J. England, R. J. Noble, K. Bane, D. H. Dowell, C.-K. Ng, J. E. Spencer, S. Tantawi, Z. Wu, R. L. Byer, E. Peralta, K. Soong, C.-M. Chang, B. Montazeri, S. J. Wolf, B. Cowan, J. Dawson, W. Gai, P. Hommelhoff, Y.-C. Huang, C. Jing, C. McGuinness, R. B. Palmer, B. Naranjo, J. Rosenzweig, G. Travish, A. Mizrahi, L. Schachter, C. Sears, G. R. Werner, and R. B. Yoder, [Dielectric laser accelerators](#), *Reviews of Modern Physics* **86**, 1337 (2014).
- [76] M. Kozák, J. McNeur, K. J. Leedle, H. Deng, N. Schönenberger, A. Ruehl, I. Hartl, J. S. Harris, R. L. Byer, and P. Hommelhoff, [Optical gating and streaking of free electrons with sub-optical cycle precision](#), *Nature Communications* **8**, 14342 (2017).
- [77] B. Barwick, D. J. Flannigan, and A. H. Zewail, [Photon-induced near-field electron microscopy](#), *Nature* **462**, 902 (2009).

- [78] A. Feist, K. E. Echternkamp, J. Schauss, S. V. Yalunin, S. Schäfer, and C. Ropers, [Quantum coherent optical phase modulation in an ultrafast transmission electron microscope](#), *Nature* **521**, 200 (2015).
- [79] K. E. Echternkamp, A. Feist, S. Schäfer, and C. Ropers, [Ramsey-type phase control of free-electron beams](#), *Nature Physics* **12**, 1000 (2016).
- [80] M. T. Hassan, J. S. Baskin, B. Liao, and A. H. Zewail, [High-temporal-resolution electron microscopy for imaging ultrafast electron dynamics](#), *Nature Photonics* **11**, 425 (2017).
- [81] T. Plettner, R. L. Byer, E. Colby, B. Cowan, C. M. S. Sears, J. E. Spencer, and R. H. Siemann, [Visible-Laser Acceleration of Relativistic Electrons in a Semi-Infinite Vacuum](#), *Physical Review Letters* **95**, 134801 (2005).
- [82] F. O. Kirchner, A. Gliserin, F. Krausz, and P. Baum, [Laser streaking of free electrons at 25 keV](#), *Nature Photonics* **8**, 52 (2014).
- [83] G. M. Vanacore, I. Madan, G. Berruto, K. Wang, E. Pomarico, R. J. Lamb, D. McGrouther, I. Kammerer, B. Barwick, F. J. García de Abajo, and F. Carbone, [Attosecond coherent control of free-electron wave functions using semi-infinite light fields](#), *Nature Communications* **9**, 2694 (2018).
- [84] M. Krüger, M. Schenk, and P. Hommelhoff, [Attosecond control of electrons emitted from a nanoscale metal tip](#), *Nature* **475**, 78 (2011).
- [85] M. Moshinsky, [Diffraction in Time](#), *Physical Review* **88**, 625 (1952).
- [86] F. Lindner, M. G. Schätzel, H. Walther, A. Baltuška, E. Goulielmakis, F. Krausz, D. B. Milošević, D. Bauer, W. Becker, and G. G. Paulus, [Attosecond Double-Slit Experiment](#), *Physical Review Letters* **95**, 040401 (2005).
- [87] P. M. Paul, E. S. Toma, P. Breger, G. Mullot, F. Auge, P. Balcou, H. G. Muller, and P. Agostini, [Observation of a Train of Attosecond Pulses from High Harmonic Generation](#), *Science* **292**, 1689 (2001).
- [88] M. C. Hoffmann and J. A. Fülöp, [Intense ultrashort terahertz pulses: generation and applications](#), *Journal of Physics D: Applied Physics* **44**, 083001 (2011).
- [89] C. Kealhofer, W. Schneider, D. Ehberger, A. Ryabov, F. Krausz, and P. Baum, [All-optical control and metrology of electron pulses](#), *Science* **352**, 429 (2016).

- [90] E. A. Nanni, W. R. Huang, K.-H. Hong, K. Ravi, A. Fallahi, G. Moriena, R. J. D. Miller, and F. X. Kärtner, [Terahertz-driven linear electron acceleration](#), *Nature Communications* **6** (2015).
- [91] R. B. Yoder and J. B. Rosenzweig, [Side-coupled slab-symmetric structure for high-gradient acceleration using terahertz power](#), *Physical Review Special Topics – Accelerators and Beams* **8**, 111301 (2005).
- [92] L. J. Wong, A. Fallahi, and F. X. Kärtner, [Compact electron acceleration and bunch compression in THz waveguides](#), *Optics Express* **21**, 9792 (2013).
- [93] J. Fabianska, G. Kassier, and T. Feurer, [Split ring resonator based THz-driven electron streak camera featuring femtosecond resolution](#), *Scientific Reports* **4**, 5645 (2014).
- [94] S. R. Greig and A. Y. Elezzabi, [On the role of terahertz field acceleration and beaming of surface plasmon generated ultrashort electron pulses](#), *Applied Physics Letters* **105**, 241115 (2014).
- [95] D. Zhang, A. Fallahi, M. Hemmer, X. Wu, M. Fakhari, Y. Hua, H. Cankaya, A.-L. Calendron, L. E. Zapata, N. H. Matlis, and F. X. Kärtner, [Segmented terahertz electron accelerator and manipulator \(STEAM\)](#), *Nature Photonics* **12**, 336 (2018).
- [96] E. Curry, S. Fabbri, J. Maxson, P. Musumeci, and A. Gover, [Meter-Scale Terahertz-Driven Acceleration of a Relativistic Beam](#), *Physical Review Letters* **120**, 094801 (2018).
- [97] L. Zhao, Z. Wang, C. Lu, R. Wang, C. Hu, P. Wang, J. Qi, T. Jiang, S. Liu, Z. Ma, P. Qi, F. and Zhu, Y. Cheng, Z. Shi, Y. Shi, W. Song, X. Zhu, J. Shi, Y. Wang, L. Yan, L. Zhu, D. Xiang, and J. Zhang, [Terahertz Streaking of Few-Femtosecond Relativistic Electron Beams](#), *Physical Review X* **8**, 021061 (2018).
- [98] R. K. Li, M. C. Hoffmann, E. A. Nanni, S. H. Glenzer, M. E. Kozina, A. M. Lindenberg, B. K. Ofori-Okai, A. H. Reid, X. Shen, S. P. Weathersby, J. Yang, M. Zajac, and X. J. Wang, [Terahertz-based subfemtosecond metrology of relativistic electron beams](#), *Physical Review Accelerators and Beams* **22**, 012803 (2019).
- [99] A. Ryabov and P. Baum, [Electron microscopy of electromagnetic waveforms](#), *Science* **353**, 374 (2016).

- [100] Y. Morimoto and P. Baum, [Attosecond control of electron beams at dielectric and absorbing membranes](#), *Physical Review A* **97**, 033815 (2018).
- [101] F. X. Kärtner, F. Ahr, A.-L. Calendron, H. Çankaya, S. Carbajo, G. Chang, G. Cirmi, K. Dörner, U. Dorda, A. Fallahi, A. Hartin, M. Hemmer, R. Hobbs, Y. Hua, W. R. Huang, R. Letrun, N. Matlis, V. Mazalova, O. D. Mücke, E. Nanni, W. Putnam, K. Ravi, F. Reichert, I. Sarrou, X. Wu, A. Yahaghi, H. Ye, L. Zapata, D. Zhang, C. Zhou, R. J. D. Miller, K. K. Berggren, H. Graafsma, A. Meents, R. W. Assmann, H. N. Chapman, and P. Fromme, [AXSIS: Exploring the frontiers in attosecond x-ray science, imaging and spectroscopy](#), *Nuclear Instruments and Methods in Physics Research Section A: Accelerators, Spectrometers, Detectors and Associated Equipment* **829**, 24 (2016).
- [102] M. V. Tsarev, D. Ehberger, and P. Baum, [High-average-power, intense THz pulses from a LiNbO<sub>3</sub> slab with silicon output coupler](#), *Applied Physics B* **122**, 30 (2016).
- [103] D. Ehberger, C. Kealhofer, and P. Baum, [Electron energy analysis by phase-space shaping with THz field cycles](#), *Structural Dynamics* **5**, 044303 (2018).
- [104] D. Ehberger, A. Ryabov, and P. Baum, [Tilted Electron Pulses](#), *Physical Review Letters* **121**, 094801 (2018).
- [105] D. Ehberger, K. J. Mohler, T. Vasileiadis, R. Ernstorfer, L. Waldecker, and P. Baum, [Terahertz Compression of Electron Pulses at a Planar Mirror Membrane](#), *Physical Review Applied* **11**, 024034 (2019).
- [106] J. Hoffrogge, J. P. Stein, M. Krüger, M. Förster, J. Hammer, D. Ehberger, P. Baum, and P. Hommelhoff, [Tip-based source of femtosecond electron pulses at 30 keV](#), *Journal of Applied Physics* **115**, 094506 (2014).
- [107] D. Ehberger, J. Hammer, M. Eisele, M. Krüger, J. Noe, A. Högele, and P. Hommelhoff, [Highly Coherent Electron Beam from a Laser-Triggered Tungsten Needle Tip](#), *Physical Review Letters* **114**, 227601 (2015).
- [108] A. Feist, N. Bach, N. R. da Silva, T. Danz, M. Möller, K. E. Priebe, T. Domröse, J. G. Gatzmann, S. Rost, J. Schauss, S. Strauch, R. Bormann, M. Siviş, S. Schäfer, and C. Ropers, [Ultrafast transmission electron microscopy using a laser-driven field emitter: Femtosecond resolution with a high coherence electron beam](#), *Ultramicroscopy* **176**, 63 (2017).

- [109] M. Ossiander, J. Riemensberger, S. Neppl, M. Mittermair, M. Schäffer, A. Duensing, M. S. Wagner, R. Heider, M. Wurzer, M. Gerl, M. Schnitzenbaumer, J. V. Barth, F. Libisch, C. Lemell, J. Burgdörfer, P. Feulner, and R. Kienberger, [Absolute timing of the photoelectric effect](#), *Nature* **561**, 374 (2018).
- [110] M. Aidelsburger, F. O. Kirchner, F. Krausz, and P. Baum, [Single-electron pulses for ultrafast diffraction](#), *Proceedings of the National Academy of Sciences of the United States of America* **107**, 19714 (2010).
- [111] L. Kasmi, D. Kreier, M. Bradler, E. Riedle, and P. Baum, [Femtosecond single-electron pulses generated by two-photon photoemission close to the work function](#), *New Journal of Physics* **17**, 033008 (2015).
- [112] S. Lahme, C. Kealhofer, F. Krausz, and P. Baum, [Femtosecond single-electron diffraction](#), *Structural Dynamics* **1**, 034303 (2014).
- [113] C. Kealhofer, S. Lahme, T. Urban, and P. Baum, [Signal-to-noise in femtosecond electron diffraction](#), *Ultramicroscopy* **159**, 19 (2015).
- [114] F. O. Kirchner, S. Lahme, F. Krausz, and P. Baum, [Coherence of femtosecond single electrons exceeds biomolecular dimensions](#), *New Journal of Physics* **15**, 063021 (2013).
- [115] L. Waldecker, R. Bertoni, and R. Ernstorfer, [Compact femtosecond electron diffractometer with 100 keV electron bunches approaching the single-electron pulse duration limit](#), *Journal of Applied Physics* **117**, 044903 (2015).
- [116] P. Baum, [On the physics of ultrashort single-electron pulses for time-resolved microscopy and diffraction](#), *Chemical Physics* **423**, 55 (2013).
- [117] P. Baum, [Quantum dynamics of attosecond electron pulse compression](#), *Journal of Applied Physics* **122**, 223105 (2017).
- [118] R. Yang and J. O. Berger, [Estimation of a Covariance Matrix Using the Reference Prior](#), *The Annals of Statistics* **22**, 1195 (1994).
- [119] H. Kogelnik and T. Li, [Laser Beams and Resonators](#), *Applied Optics* **5**, 1550 (1966).
- [120] E. Hemsing, G. Stupakov, D. Xiang, and A. Zholents, [Beam by design: Laser manipulation of electrons in modern accelerators](#), *Reviews of Modern Physics* **86**, 897 (2014).

- 
- [121] V. Ziemann, [Charged Particle Transport, Gaussian Optics, Error Propagation: It's all the Same](#), Proceedings of International Particle Accelerator Conference (IPAC'16) pp. 3324–3327 (2016).
- [122] K. Floettmann, [Some basic features of the beam emittance](#), Physical Review Special Topics – Accelerators and Beams **6**, 034202 (2003).
- [123] B. J. Siwick, J. R. Dwyer, R. E. Jordan, and R. J. D. Miller, [Ultrafast electron optics: Propagation dynamics of femtosecond electron packets](#), Journal of Applied Physics **92**, 1643 (2002).
- [124] O. J. Luiten, S. B. van der Geer, M. J. de Loos, F. B. Kiewiet, and M. J. van der Wiel, [How to Realize Uniform Three-Dimensional Ellipsoidal Electron Bunches](#), Physical Review Letters **93**, 094802 (2004).
- [125] M. A. Monastyrskiy, S. V. Andreev, D. E. Greenfield, V. A. Bryukhnevich, G. I. Land Tarasov, and M. Y. Schelev, [Computer modeling of a subfemtosecond photoelectron gun with time-dependent electric field for TRED experiments](#), Proceedings of SPIE **5580**, 324 (2005).
- [126] S. A. Hilbert, C. Uiterwaal, B. Barwick, H. Batelaan, and A. H. Zewail, [Temporal lenses for attosecond and femtosecond electron pulses](#), Proceedings of the National Academy of Sciences of the United States of America **106**, 10558 (2009).
- [127] S. A. Self, [Focusing of spherical gaussian beams](#), Appl. Opt. **22**, 658 (1983).
- [128] A. Gliserin, [Towards attosecond 4D imaging of atomic-scale dynamics by single-electron diraction](#), Ph.D. thesis, Ludwig-Maximilians-Universität München (2014).
- [129] A. Gliserin, M. Walbran, and P. Baum, [Passive optical enhancement of laser-microwave synchronization](#), Applied Physics Letters **103**, 031113 (2013).
- [130] P. Baum and F. Krausz, [Capturing atomic-scale carrier dynamics with electrons](#), Chemical Physics Letters **683**, 57 (2017).
- [131] R. F. Egerton, [Electron energy-loss spectroscopy in the TEM](#), Reports on Progress in Physics **72**, 016502 (2009).
- [132] O. L. Krivanek, T. C. Lovejoy, N. Dellby, and R. W. Carpenter, [Monochromated STEM with a 30 meV-wide, atom-sized electron probe](#), Microscopy **62**, 3 (2013).

- [133] W. Verhoeven, J. F. M. van Rens, W. F. Toonen, E. R. Kieft, P. H. A. Mutsaers, and O. J. Luiten, [Time-of-flight electron energy loss spectroscopy by longitudinal phase space manipulation with microwave cavities](#), *Structural Dynamics* **5**, 051101 (2018).
- [134] J. B. Hastings, F. M. Rudakov, D. H. Dowell, J. F. Schmerge, J. D. Cardoza, J. M. Castro, S. M. Gierman, H. Loos, and P. M. Weber, [Ultrafast time-resolved electron diffraction with megavolt electron beams](#), *Applied Physics Letters* **89**, 184109 (2006).
- [135] G. H. Kassier, K. Haupt, N. Erasmus, E. G. Rohwer, H. M. von Bergmann, H. Schwoerer, S. M. M. Coelho, and F. D. Auret, [A compact streak camera for 150 fs time resolved measurement of bright pulses in ultrafast electron diffraction](#), *Review of Scientific Instruments* **81**, 105103 (2010).
- [136] C. M. Scoby, R. K. Li, E. Threlkeld, H. To, and P. Musumeci, [Single-shot 35 fs temporal resolution electron shadowgraphy](#), *Applied Physics Letters* **102**, 023506 (2013).
- [137] C. Kealhofer, B. B. Klopfer, G. E. Skulason, T. Juffmann, S. M. Foreman, and M. A. Kasevich, [Ultrafast oscilloscope based on laser-triggered field emitters](#), *Optics Letters* **40**, 260 (2015).
- [138] T. Hosokawa, H. Fujioka, and K. Ura, [Generation and measurement of subpicosecond electron beam pulses](#), *Review of Scientific Instruments* **49**, 624 (1978).
- [139] W. Verhoeven, J. F. M. van Rens, E. R. Kieft, P. H. A. Mutsaers, and O. J. Luiten, [High quality ultrafast transmission electron microscopy using resonant microwave cavities](#), *Ultramicroscopy* **188**, 85 (2018).
- [140] R. W. Boyd, *Nonlinear Optics (Third Edition)* (Academic Press, Burlington 2008).
- [141] M. Shalaby and C. P. Hauri, [Demonstration of a low-frequency three-dimensional terahertz bullet with extreme brightness](#), *Nature Communications* **6**, 5976 (2015).
- [142] S.-W. Huang, E. Granados, K. Ravi, K.-H. Hong, L. E. Zapata, and F. X. Kärtner, [Highly efficient terahertz pulse generation by optical rectification in stoichiometric and cryo-cooled congruent lithium niobate](#), *Journal of Modern Optics* **62**, 1486 (2015).

- [143] J. A. Fülöp, Z. Ollmann, C. Lombosi, C. Skrobol, S. Klingebiel, L. Pálfalvi, F. Krausz, S. Karsch, and J. Hebling, [Efficient generation of THz pulses with 0.4 mJ energy](#), *Optics Express* **22**, 20155 (2014).
- [144] A. Schneider, M. Neis, M. Stillhart, B. Ruiz, R. U. A. Khan, and P. Günter, [Generation of terahertz pulses through optical rectification in organic DAST crystals: theory and experiment](#), *Journal of the Optical Society of America B* **23**, 1822 (2006).
- [145] D. E. Thompson and P. D. Coleman, [Step-tunable Far Infrared Radiation By Phase Matched Mixing In Planar-dielectric Waveguides](#), *IEEE Transactions On Microwave Theory and Techniques* **MT22**, 995 (1974).
- [146] G. Chang, C. J. Divin, J. Yang, M. A. Musheinish, S. L. Williamson, A. Galvanauskas, and T. B. Norris, [GaP waveguide emitters for high power broadband THz generation pumped by Yb-doped fiber lasers](#), *Optics Express* **15**, 16308 (2007).
- [147] M. I. Bakunov, S. B. Bodrov, A. V. Maslov, and M. Hangyo, [Theory of terahertz generation in a slab of electro-optic material using an ultrashort laser pulse focused to a line](#), *Physical Review B* **76**, 085346 (2007).
- [148] M. I. Bakunov, E. A. Mashkovich, M. V. Tsarev, and S. D. Gorelov, [Efficient Cherenkov-type terahertz generation in Si-prism-LiNbO<sub>3</sub>-slab structure pumped by nanojoule-level ultrashort laser pulses](#), *Applied Physics Letters* **101**, 151102 (2012).
- [149] S. B. Bodrov, I. E. Ilyakov, B. V. Shishkin, and A. N. Stepanov, [Efficient terahertz generation by optical rectification in Si-LiNbO<sub>3</sub>-air-metal sandwich structure with variable air gap](#), *Applied Physics Letters* **100**, 201114 (2012).
- [150] J. A. Fülöp, L. Pálfalvi, S. Klingebiel, G. Almasi, F. Krausz, S. Karsch, and J. Hebling, [Generation of sub-mJ terahertz pulses by optical rectification](#), *Optics Letters* **37**, 557 (2012).
- [151] M. C. Hoffmann, K.-L. Yeh, J. Hebling, and K. A. Nelson, [Efficient terahertz generation by optical rectification at 1035 nm](#), *Optics Express* **15**, 11706 (2007).
- [152] X. Wu, S. Carbajo, K. Ravi, F. Ahr, G. Cirimi, Y. Zhou, O. D. Mücke, and F. X. Kärtner, [Terahertz generation in lithium niobate driven by Ti:sapphire laser pulses and its limitations](#), *Optics Letters* **39**, 5403 (2014).

- [153] W. Schneider, A. Ryabov, C. Lombosi, T. Metzger, Z. Major, J. A. Fülöp, and P. Baum, [800-fs, 330-uJ pulses from a 100-W regenerative Yb:YAG thin-disk amplifier at 300 kHz and THz generation in LiNbO<sub>3</sub>](#), *Optics Letters* **39**, 6604 (2014).
- [154] L. Pálfalvi, J. Hebling, J. Kuhl, A. Péter, and K. Polgár, [Temperature dependence of the absorption and refraction of Mg-doped congruent and stoichiometric LiNbO<sub>3</sub> in the THz range](#), *Journal of Applied Physics* **97**, 123505 (2005).
- [155] H. Fattahi, H. G. Barros, M. Gorjan, T. Nubbemeyer, B. Alsaif, C. Y. Teisset, M. Schultze, S. Prinz, M. Haefner, M. Ueffing, A. Alismail, L. Vámos, A. Schwarz, O. Pronin, J. Brons, X. T. Geng, G. Arisholm, M. Ciappina, V. S. Yakovlev, D.-E. Kim, A. M. Azzeer, N. Karpowicz, D. Sutter, Z. Major, T. Metzger, and F. Krausz, [Third-generation femtosecond technology](#), *Optica* **1**, 45 (2014).
- [156] C. J. Saraceno, F. Emaury, C. Schriber, M. Hoffmann, M. Golling, T. Südmeyer, and U. Keller, [Ultrafast thin-disk laser with 80  \$\mu\$ J pulse energy and 242 W of average power](#), *Optics Letters* **39**, 9 (2014).
- [157] A. Klenke, S. Breitkopf, M. Kienel, T. Gottschall, T. Eidam, S. Hädrich, J. Rothhardt, J. Limpert, and A. Tünnermann, [530 W, 1.3 mJ, four-channel coherently combined femtosecond fiber chirped-pulse amplification system](#), *Optics Letters* **38**, 2283 (2013).
- [158] D. Eimerl, [High average power harmonic-generation](#), *IEEE Journal of Quantum Electronics* **23**, 575 (1987).
- [159] A. G. Stepanov, J. Kuhl, I. Z. Kozma, E. Riedle, G. Almasi, and J. Hebling, [Scaling up the energy of THz pulses created by optical rectification](#), *Optics Express* **13**, 5762 (2005).
- [160] M. Theuer, G. Torosyan, C. Rau, R. Beigang, K. Maki, C. Otani, and K. Kawase, [Efficient generation of Cherenkov-type terahertz radiation from a lithium niobate crystal with a silicon prism output coupler](#), *Applied Physics Letters* **88**, 071122 (2006).
- [161] S. B. Bodrov, M. I. Bakunov, and M. Hangyo, [Efficient Cherenkov emission of broadband terahertz radiation from an ultrashort laser pulse in a sandwich structure with nonlinear core](#), *Journal of Applied Physics* **104**, 093105 (2008).

- [162] O. Gayer, Z. Sacks, E. Galun, and A. Arie, [Temperature and wavelength dependent refractive index equations for MgO-doped congruent and stoichiometric LiNbO<sub>3</sub>](#), *Applied Physics B* **91**, 343 (2008).
- [163] S. B. Bodrov, A. N. Stepanov, M. I. Bakunov, B. V. Shishkin, I. E. Ilyakov, and R. A. Akhmedzhanov, [Highly efficient optical-to-terahertz conversion in a sandwich structure with LiNbO<sub>3</sub> core](#), *Optics Express* **17**, 1871 (2009).
- [164] Q. Chen, M. Tani, Z. Jiang, and X.-C. Zhang, [Electro-optic transceivers for terahertz-wave applications](#), *Journal of the Optical Society of America B* **18**, 823 (2001).
- [165] G. Gallot and D. Grischkowsky, [Electro-optic detection of terahertz radiation](#), *Journal of the Optical Society of America B* **16**, 1204 (1999).
- [166] S. Kovalev and G. Kitaeva, [Two alternative approaches to electro-optical detection of terahertz pulses](#), *JETP Letters* **94**, 91 (2011).
- [167] Y. Qiu, K. B. Ucer, and R. T. Williams, [Formation time of a small electron polaron in LiNbO<sub>3</sub>: measurements and interpretation](#), *physica status solidi (c)* **2**, 232 (2005).
- [168] D. Maxein, S. Kratz, P. Reckenthaeler, J. Bückers, D. Haertle, T. Woike, and K. Buse, [Polarons in magnesium-doped lithium niobate crystals induced by femtosecond light pulses](#), *Applied Physics B* **92**, 543 (2008).
- [169] B. Riscob, I. Bhaumik, S. Ganesamoorthy, R. Bhatt, N. Vijayan, A. K. Karnal, M. A. Wahab, and G. Bhagavannarayana, [Effect of Mg doping on the growth aspects, crystalline perfection, and optical and thermal properties of congruent LiNbO<sub>3</sub> single crystals](#), *Journal of Applied Crystallography* **46**, 1854 (2013).
- [170] M. J. Prandolini, R. Riedel, M. Schulz, A. Hage, H. Höppner, and F. Tavella, [Design considerations for a high power, ultrabroadband optical parametric chirped-pulse amplifier](#), *Optics Express* **22**, 1594 (2014).
- [171] C. Rothhardt, J. Rothhardt, A. Klenke, T. Peschel, R. Eberhardt, J. Limpert, and A. Tünnermann, [BBO-sapphire sandwich structure for frequency conversion of high power lasers](#), *Optical Materials Express* **4**, 1092 (2014).
- [172] M. Bradler and E. Riedle, [Sub-20 fs μJ-energy pulses tunable down to the near-UV from a 1 MHz Yb-fiber laser system](#), *Optics Letters* **39**, 2588 (2014).
- [173] A. Ryabov, [Electron microscopy of electromagnetic waveforms](#), Ph.D. thesis, Ludwig-Maximilians-Universität (2017).

- [174] D. Kreier, [Ultrafast single-electron diffraction at 100 keV and investigation of carbon-nanotube dynamics](#), Ph.D. thesis, Ludwig–Maximilians–Universität (2015).
- [175] P. Emma, R. Akre, J. Arthur, R. Bionta, C. Bostedt, J. Bozek, A. Brachmann, P. Bucksbaum, R. Coffee, F.-J. Decker, Y. Ding, D. Dowell, S. Edstrom, A. Fisher, J. Frisch, S. Gilevich, J. Hastings, G. Hays, P. Hering, Z. Huang, R. Iverson, H. Loos, M. Messerschmidt, A. Miahnahri, S. Moeller, H.-D. Nuhn, G. Pile, D. Ratner, J. Rzepiela, D. Schultz, T. Smith, P. Stefan, H. Tompkins, J. Turner, J. Welch, W. White, J. Wu, G. Yocky, and J. Galayda, [First lasing and operation of an ångström-wavelength free-electron laser](#), *Nature Photonics* **4**, 641 (2010).
- [176] D. J. Flannigan and A. H. Zewail, [4D Electron Microscopy: Principles and Applications](#), *Accounts of Chemical Research* **45**, 1828 (2012).
- [177] J. Tenboer, S. Basu, N. Zatsepin, K. Pande, D. Milathianaki, M. Frank, M. Hunter, S. Boutet, G. J. Williams, J. E. Koglin, D. Oberthuer, M. Heymann, C. Kupitz, C. Conrad, J. Coe, S. Roy-Chowdhury, U. Weierstall, D. James, D. Wang, T. Grant, A. Barty, O. Yefanov, J. Scales, C. Gati, C. Seuring, V. Srajer, R. Henning, P. Schwander, R. Fromme, A. Ourmazd, K. Moffat, J. J. Van Thor, J. C. H. Spence, P. Fromme, H. N. Chapman, and M. Schmidt, [Time-resolved serial crystallography captures high-resolution intermediates of photoactive yellow protein](#), *Science* **346**, 1242 (2014).
- [178] S. Schulz, I. Grguras, C. Behrens, H. Bromberger, J. T. Costello, M. K. Czwalinn, M. Felber, M. C. Hoffmann, M. Ilchen, H. Y. Liu, T. Mazza, M. Meyer, S. Pfeiffer, P. Predki, S. Schefer, C. Schmidt, U. Wegner, H. Schlarb, and A. L. Cavalieri, [Femtosecond all-optical synchronization of an X-ray free-electron laser](#), *Nature Communications* **6**, 5938 (2015).
- [179] G. J. H. Brussaard, A. Lassise, P. L. E. M. Pasmans, P. H. A. Mutsaers, M. J. van der Wiel, and O. J. Luiten, [Direct measurement of synchronization between femtosecond laser pulses and a 3 GHz radio frequency electric field inside a resonant cavity](#), *Applied Physics Letters* **103**, 141105 (2013).
- [180] E. Esarey, C. B. Schroeder, and W. P. Leemans, [Physics of laser-driven plasma-based electron accelerators](#), *Reviews of Modern Physics* **81**, 1229 (2009).
- [181] L. Wimmer, G. Herink, D. R. Solli, S. V. Yalunin, K. E. Echternkamp, and C. Ropers, [Terahertz control of nanotip photoemission](#), *Nature Physics* **10**, 432 (2014).

- [182] Materials and methods are available as supplementary materials on Science Online. [www.sciencemag.org/content/352/6284/429/suppl/DC1](http://www.sciencemag.org/content/352/6284/429/suppl/DC1).
- [183] F. J. García de Abajo and M. Kociak, *Electron energy-gain spectroscopy*, *New Journal of Physics* **10**, 073035 (2008).
- [184] R. Kienberger, E. Goulielmakis, M. Uiberacker, A. Baltuska, V. Yakovlev, F. Bammer, A. Scrinzi, T. Westerwalbesloh, U. Kleineberg, U. Heinzmann, M. Drescher, and F. Krausz, *Atomic transient recorder*, *Nature* **427**, 817 (2004).
- [185] General particle tracer code ([www.pulsar.nl/gpt](http://www.pulsar.nl/gpt)).
- [186] U. Frühling, M. Wieland, M. Gensch, T. Gebert, B. Schütte, M. Krikunova, R. Kalms, F. Budzyn, O. Grimm, J. Rossbach, E. Plönjes, and M. Drescher, *Single-shot terahertz-field-driven X-ray streak camera*, *Nature Photonics* **3**, 523 (2009).
- [187] I. Grguraš, A. R. Maier, C. Behrens, T. Mazza, T. J. Kelly, P. Radcliffe, S. Duesterer, A. K. Kazansky, N. M. Kabachnik, T. Tschentscher, J. T. Costello, M. Meyer, M. C. Hoffmann, H. Schlarb, and A. L. Cavalieri, *Ultrafast X-ray pulse characterization at free-electron lasers*, *Nature Photonics* **6**, 851 (2012).
- [188] W. Verhoeven, J. F. M. van Rens, M. A. W. van Nindhuijs, W. F. Toonen, E. R. Kieft, P. H. A. Mutsaers, and O. J. Luiten, *Time-of-flight electron energy loss spectroscopy using  $TM_{110}$  deflection cavities*, *Structural Dynamics* **3**, 054303 (2016).
- [189] H. Ihee, V. A. Lobastov, U. M. Gomez, B. M. Goodson, R. Srinivasan, C. Y. Ruan, and A. H. Zewail, *Direct Imaging of Transient Molecular Structures with Ultrafast Diffraction*, *Science* **291**, 458 (2001).
- [190] J. Yang, M. Guehr, X. Z. Shen, R. K. Li, T. Vecchione, R. Coffee, J. Corbett, A. Fry, N. Hartmann, C. Hast, K. Hegazy, K. Jobe, I. Makasyuk, J. Robinson, M. S. Robinson, S. Vetter, S. Weathersby, C. Yoneda, X. J. Wang, and M. Centurion, *Diffraction Imaging of Coherent Nuclear Motion in Isolated Molecules*, *Physical Review Letters* **117**, 153002 (2016).
- [191] H. Lourenço-Martins, P. Das, L. H. G. Tizei, R. Weil, and M. Kociak, *Self-hybridization within non-Hermitian localized plasmonic systems*, *Nature Physics* **14**, 360 (2018).

- [192] O. L. Krivanek, T. C. Lovejoy, N. Dellby, T. Aoki, R. W. Carpenter, P. Rez, E. Soignard, J. Zhu, P. E. Batson, M. J. Lagos, R. F. Egerton, and P. A. Crozier, [Vibrational spectroscopy in the electron microscope](#), *Nature* **514**, 209 (2014).
- [193] F. Carbone, O.-H. Kwon, and A. H. Zewail, [Dynamics of Chemical Bonding Mapped by Energy-Resolved 4D Electron Microscopy](#), *Science* **325**, 181 (2009).
- [194] R. M. van der Veen, T. J. Penfold, and A. H. Zewail, [Ultrafast core-loss spectroscopy in four-dimensional electron microscopy](#), *Structural Dynamics* **2**, 024302 (2015).
- [195] M. J. Lagos, A. Trügler, U. Hohenester, and P. E. Batson, [Mapping vibrational surface and bulk modes in a single nanocube](#), *Nature* **543**, 529 (2017).
- [196] S. H. Chew, F. Süßmann, C. Späth, A. Wirth, J. Schmidt, S. Zherebtsov, A. Guggenmos, A. Oelsner, N. Weber, J. Kapaldo, A. Gliserin, M. I. Stockman, M. F. Kling, and U. Kleineberg, [Time-of-flight-photoelectron emission microscopy on plasmonic structures using attosecond extreme ultraviolet pulses](#), *Applied Physics Letters* **100**, 051904 (2012).
- [197] A. Gliserin, M. Walbran, and P. Baum, [A high-resolution time-of-flight energy analyzer for femtosecond electron pulses at 30 keV](#), *Review of Scientific Instruments* **87**, 033302 (2016).
- [198] W. Verhoeven, J. van Rens, W. Toonen, E. Kieft, P. Mutsaers, and O. Luiten, [Time-of-Flight Electron Energy Loss Spectroscopy by Longitudinal Phase Space Manipulation with Microwave Cavities](#), arXiv:1711.10798 (2018).
- [199] C. Weninger and P. Baum, [Temporal distortions in magnetic lenses](#), *Ultramicroscopy* **113**, 145 (2012).
- [200] D. Kreier, D. Sabonis, and P. Baum, [Alignment of magnetic solenoid lenses for minimizing temporal distortions](#), *Journal of Optics* **16**, 075201 (2014).
- [201] E. Pomarico, I. Madan, G. Berruto, G. M. Vanacore, K. P. Wang, I. Kaminer, F. J. García de Abajo, and F. Carbone, [meV resolution in laser-assisted energy-filtered transmission electron microscopy](#), *ACS Photonics* **5**, 759 (2018).
- [202] D. Cesar, J. Maxson, X. Shen, K. P. Wootton, S. Tan, R. J. England, and P. Musumeci, [Enhanced energy gain in a dielectric laser accelerator using a tilted pulse front laser](#), *Optics Express* **26**, 29216 (2018).

- [203] R. Tommasini and E. E. Fill, [Effective traveling-wave excitation below the speed of light](#), *Optics Letters* **26**, 689 (2001).
- [204] H. Daido, [Review of soft x-ray laser researches and developments](#), *Reports On Progress In Physics* **65**, PII S0034 (2002).
- [205] A. Shirakawa, I. Sakane, and T. Kobayashi, [Pulse-front-matched optical parametric amplification for sub-10-fs pulse generation tunable in the visible and near infrared](#), *Optics Letters* **23**, 1292 (1998).
- [206] J. P. Torres, M. Hendrych, and A. Valencia, [Angular dispersion: an enabling tool in nonlinear and quantum optics](#), *Advances In Optics and Photonics* **2**, 319 (2010).
- [207] A. Patel, Y. Svirko, C. Durfee, and P. G. Kazansky, [Direct Writing with Tilted-Front Femtosecond Pulses](#), *Scientific Reports* **7**, 12928 (2017).
- [208] E. Prat, F. Lohl, and S. Reiche, [Efficient generation of short and high-power x-ray free-electron-laser pulses based on superradiance with a transversely tilted beam](#), *Physical Review Special Topics – Accelerators and Beams* **18**, 100701 (2015).
- [209] P. Baum and A. H. Zewail, [Breaking resolution limits in ultrafast electron diffraction and microscopy](#), *Proceedings of the National Academy of Sciences of the United States of America* **103**, 16105 (2006).
- [210] J. Faure, [Viewpoint: Shaping electron bunches at the femtosecond level](#), *Physics* **11**, 87 (2018).
- [211] J. Hebling, [Derivation of the pulse front tilt caused by angular dispersion](#), *Optical and Quantum Electronics* **28**, 1759 (1996).
- [212] See Supplemental Material at <http://link.aps.org/supplemental/10.1103/PhysRevLett.121.094801> for analytic derivations and details on data analysis.
- [213] N. Laman and D. Grischkowsky, [Terahertz conductivity of thin metal films](#), *Applied Physics Letters* **93**, 051105 (2008).
- [214] M. Gulde, S. Schweda, G. Storeck, M. Maiti, H. K. Yu, A. M. Wodtke, S. Schafer, and C. Ropers, [Ultrafast low-energy electron diffraction in transmission resolves polymer/graphene superstructure dynamics](#), *Science* **345**, 200 (2014).

- [215] J. Verbeeck, H. Tian, and P. Schattschneider, [Production and application of electron vortex beams](#), *Nature* **467**, 301 (2010).
- [216] N. Voloch-Bloch, Y. Lereah, Y. Lilach, A. Gover, and A. Arie, [Generation of electron airy beams](#), *Nature* **494**, 331 (2013).
- [217] V. Grillo, E. Karimi, G. C. Gazzadi, S. Frabboni, M. R. Dennis, and R. W. Boyd, [Generation of Nondiffracting Electron Bessel Beams](#), *Physical Review X* **4**, 011013 (2014).
- [218] C. L. Zheng, T. C. Petersen, H. Kirmse, W. Neumann, M. J. Morgan, and J. Etheridge, [Axicon Lens for Electrons Using a Magnetic Vortex: The Efficient Generation of a Bessel Beam](#), *Physical Review Letters* **119**, 174801 (2017).
- [219] G. Herink, L. Wimmer, and C. Ropers, [Field emission at terahertz frequencies: AC-tunneling and ultrafast carrier dynamics](#), *New Journal of Physics* **16**, 123005 (2014).

# Acknowledgments

This work would not have been possible without the help, support and encouragement of many people, whom I would like to thank in the following.

First of all, I would like to thank Prof. Dr. Ferenc Krausz for taking me as PhD candidate and giving me the opportunity to work among inspiring and outstanding scientists in a world's leading research group. This work has benefited a lot from Ferenc's support and his insightful comments. Also, I would like to thank Prof. Dr. Alexander Högele for kindly offering to review this thesis and his sincere interest in its subject of research.

I would like to express my deep gratitude to my immediate adviser Prof. Dr. Peter Baum for his excellent scientific supervision. Peter's continued encouragement to pursue my own ideas, while making sure I would not lose my track, always fueled my motivation. His immense knowledge paired with his visionary mindset made our scientific discussions fruitful and truly inspiring. I highly appreciate his trust letting me supervise various Bachelor and Master students as well as his precious advice on scientific writing, time management and laboratory work.

Many thanks go to Prof. Dr. Catherine Kealhofer for the great time working on electron pulse compression. Together seeing terahertz compression work for the first time is certainly one of my most memorable lab experiences. In her patient way, she taught me many essential skills, which would later allow me to successfully do experiments on my own. I would also like to thank Catherine for proof reading most of this thesis and helping me to get rid of various "Germanisms".

I am grateful to Prof. Dr. Maxim Tsarev for bringing the Cherenkov style of terahertz generation to our lab and his practical help in this respect. I would like to thank Dr. Andrey Ryabov and Kathrin Mohler for endless discussion about the coincidence of velocity-matching and absence of deflection, as well as their precious help to make electrons meet terahertz pulses. I thank Andrey, Kathrin and Maxim also for proof reading parts of this thesis. Thanks go to Dr. Waldemar Schneider for

showing me how to operate his laser—the essential first step to do experiments in pre-Pharos times.

I thank all the other current and former members of AG Baum that I had the pleasure to work with: Benjamin Bauer, Bo-Han Chen, Dr. Alexander Gliserin, Sven Jandura, Dr. Daniel Kreier, Dr. Stefan Lahme, Dr. Yuya Morimoto, Sonja Tauchert, Johannes Thurner, Dr. Mikhail Volkov and Dr. Matt Walbran. In particular, I would like to thank all of the talented students under my supervision, who helped me with numerous projects: Tobias Boolakee, Jannik Esslinger, Artur Engelmann, Ann-Kathrin Raab and Eruthuparna Ramachandran. They all contributed to the great work atmosphere and offered a helping hand in countless occasions.

I would also like to thank our scientific collaborators from Berlin and Stanford, Dr. Ralph Ernstorfer, Dr. Lutz Waldecker and Thomas Vasileiadis for sharing their advanced electron source design and for the fruitful discussions.

I thank Rolf Oehm and his team from the mechanical workshop for valuable advice on mechanical design and most accurately manufactured parts, as well as Dr. Volodymyr Pervak and Dr. Elena Fedulova for their help coating cathodes on short notice.

I am grateful for having been given the opportunity to join the Interantional Max Planck Research School of Advanced Photon Science, which provided an ideal platform for exchange with other PhD students and faculty members.

Last but not least, I would like to thank my parents Melanie and Siegfried for their unconditional support, my brother Markus for lots of in-depth philosophy and physics discussions, my wife Johanna for her love, her patience and enduring encouragement throughout the past years, and my son August, who gave me a whole new and fresh perspective on basically everything.